ISBN 978-82-326-1368-7 (printed version)
ISBN 978-82-326-1369-4 (electronic version)
ISSN 1503-8181

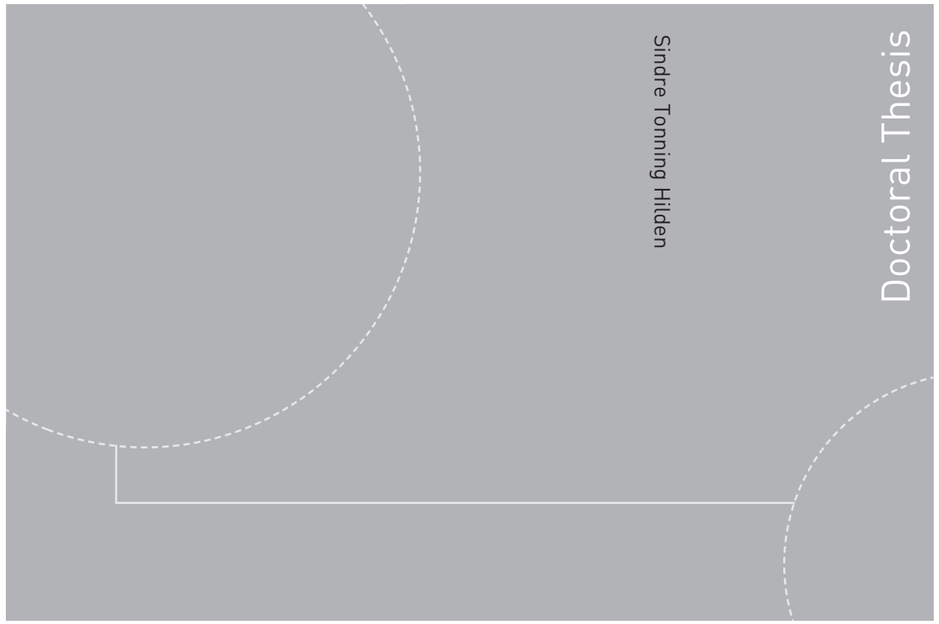

Doctoral theses at NTNU, 2016:12

Sindre Tonning Hilden

Upscaling of Water-Flooding Scenarios and Modeling of Polymer Flow

NTNU
Norwegian University of
Science and Technology

Doctoral theses at NTNU, 2016:12

NTNU

NTNU
Norwegian University of
Science and Technology
Faculty of Information Technology,
Mathematics and Electrical Engineering
Department of Mathematical Sciences

NTNU
Norwegian University of
Science and Technology

Sindre Tonning Hilden

Upscaling of Water-Flooding Scenarios and Modeling of Polymer Flow

Thesis for the degree of Philosophiae Doctor

Trondheim, March 2016

Norwegian University of Science and Technology
Faculty of Information Technology,
Mathematics and Electrical Engineering
Department of Mathematical Sciences

NTNU
Norwegian University of
Science and Technology

NTNU
Norwegian University of Science and Technology

Thesis for the degree of Philosophiae Doctor

Faculty of Information Technology,
Mathematics and Electrical Engineering
Department of Mathematical Sciences

ISBN 978-82-326-1368-7 (printed version)
ISBN 978-82-326-1369-4 (electronic version)
ISSN 1503-8181

Doctoral theses at NTNU, 2016:12

Printed by Skipnes Kommunikasjon as

Abstract

This thesis considers simulations of the fluid flow in petroleum reservoirs, and includes work on upscaling methods and on modeling of polymer flooding, which is a particular method of enhanced oil recovery.

The details of a small-scale model can have large impact on the flow on larger scales, and upscaling is therefore an essential part of reservoir modeling. We consider upscaling on the field-scale, investigate the balance of forces during the water-flooding of a reservoir, and use this to asses the applicability of different upscaling methods, and in particular steady-state methods. Two novel upscaling methods based on the steady-state assumption are suggested, and a comparison study is performed between different methods through realistic field-scale simulations. Established two-phase upscaling techniques are also extended to include polymer properties.

As an alternative to upscaling, we also consider the application of a multiscale method to run polymer flooding simulations more efficiently. Using the developed solver, we demonstrate that we are able to obtain fast and accurate solutions on complex grids, using realistic and highly non-linear flow physics.

Considering another aspect of polymer modeling, we address a known issue with the mathematical model of an import physical effect of polymer flooding, the velocity enhancement due to inaccessible pore volume. The conventional model may lead to ill-posed equations, and we propose alternative formulations to obtain numerically more stable simulations.

Contents

Preface

The following thesis is submitted for the degree of philosophiae doctor (PhD) at the Norwegian University of Science and Technology (NTNU), Trondheim, Norway.

The thesis is organized in two parts: Part I gives a short introduction to flow in porous media and to upscaling and multiscale methods. Part II contains the research papers.

Acknowledgments

First of all, I would like to thank my adviser Prof. Knut-Andreas Lie for his guidance and encouragement throughout the coarse of my PhD work. With his great knowledge and experience, he has been of invaluable assistance. I also want to thank my adviser Prof. Helge Holden for his support and helpfulness. To all my co-authors, I am appreciative for great collaboration and fruitful discussions. I would like to thank Vegard Kippe and Carl Fredrik Berg at Statoil for interesting conversations and for providing useful input from the industry point of view. For most of my PhD work, I have been working together with the Computational Geosciences group at Sintef ICT in Oslo, and I am grateful to everyone in the group for including me as part of the team and for all their enthusiastic help. At last, I would like to acknowledge my family. I would like to thank my parents for always supporting me, and I am ever so grateful to my wife, Ann-Kristin, for her encouragement, patience, and humor.

My research has been funded by VISTA, which is a basic research program funded by Statoil and conducted in close collaboration with The Norwegian Academy of Science and Letters. I am grateful to Statoil for funding the research of young scientists, and I have appreciated the occasional meetings with the other VISTA scholars.

Sindre Tonning Hilden
Oslo, March 2016

List of Papers

Paper I: **Rate Dependent Force Balance and Upscaling of Unsteady Flooding Processes**
Sindre Tonning Hilden and Carl Fredrik Berg
Submitted

Paper II: **Comparison of Two-Phase Upscaling Methods on Field Models**
Sindre Tonning Hilden and Carl Fredrik Berg
Submitted

Paper III: **Steady-State Upscaling of Polymer Flooding**
Sindre Tonning Hilden, Knut-Andreas Lie, and Xavier Raynaud
ECMOR XIV - 14th European Conference on the Mathematics of Oil Recovery, Catania, Sicily, Italy, 8-11 September 2014

Paper IV: **Multiscale Simulation of Polymer Flooding with Shear Effects**
Sindre Tonning Hilden, Olav Møyner, Knut-Andreas Lie, and Kai Bao
Submitted

Paper V: **A Well-Posed Model of Inaccessible Pore Volume for Polymer**
Sindre Tonning Hilden, Halvor Møll Nilsen, and Xavier Raynaud
Submitted

Part I

Background

Chapter 1

Introduction

An oil and gas reservoir is made up of sedimentary rock, created over a large time span by the accumulation of deposits which are gradually built up in layers. As the deposits get buried deeper and deeper, increasing pressure and temperature will eventually make the sediments into rock. The resulting reservoir formation is filled by tiny pores (voids) that are interconnected to make up a continuous pore network, where fluids are stored and able to flow. All materials containing such a pore structure is referred to as a porous medium, and other examples of porous media include sponges, cement and even human tissue. This thesis is concerned with reservoir simulation, which is the computer modeling and simulation of fluid flow in oil and gas reservoirs. While parts of this topic are reservoir specific, a lot of the theory is applicable to fluid flow in other forms of porous media as well.

Reservoir simulation is a useful tool for the oil and gas industry and is often an important part of various decision making processes. Simulations can be used for example during field development to help determine well-locations, as part of planning to asses possible methods for increasing recovery, as part of operations to optimize well controls, and in economics to estimate future income. Even though reservoir simulation has been in use since the middle of the last century, there are constantly new challenges that need to be overcome. Reservoir representations have become increasingly complex, and the industry is requesting better estimates and more detailed solutions. This places greater demands, not only on computer power, but at least as much on the mathematical modeling and numerical strategies.

To understand some of the difficulties in reservoir modeling and simulation, it is vital to get a grasp of the large span of spatial scales present in a reservoir. At the smallest scales, the flow of fluid takes place in tiny

pores (and pore throats) in between the mineral grains that make up the sedimentary rock. These pores are typically on the scale of micro meters. At the other end of the scales, the whole reservoir can stretch out over an area of several square kilometers, and the wells can be spaced by hundreds or even thousands of meters. From a modeling standpoint, this vast span of scales presents great challenges. It is not possible to include pore-scale details into a model of an entire field. First of all, the amount of information would simply be orders of magnitude too large for any computer to handle. Second, information at such a level of detail about the formation is simply not possible to obtain. In any case, for a reservoir simulation, it is the estimates of global flow patterns and of the hydrocarbon production that is most important. The details about the small-scale flow is really not of interest. At the same time, small-scale heterogeneities of the reservoir can have a large impact on the global flow, and so in order to create a representative model of the reservoir, it is important to understand and include the physical effects of the smaller scales. To this end, the fluid flow is considered separately on different scales by models of various physical sizes. Pore-scale models are used to simulate the flow in the pore network, where the entire model can have a length of less than a centimeter in each direction. From the wells, core samples of the rock, which are a few centimeters in diameter, are obtained and analyzed in the lab. On a larger scale, a geological model is created as a representation of the entire field, made by combining different sources of information, such as seismic data, well-logs and general knowledge of geological formations.

The details of each model scale have an impact on the flow on larger scales, and should therefore to be accounted for. As it is not possible to include all details from one model scale into the next, there is a need to average the properties in some way. This process is known as upscaling, and is an essential part of model construction. When a model is upscaled, it is replaced by an equivalent coarser model, containing less information, but which hopefully is representative of the original. This is in general a difficult task, as the problem is highly over-determined. Even though upscaling has been researched extensively for decades, there is still no predominant upscaling strategy, as there is no method which is always better than another. The best choice of upscaling method will depend on the specific model and the flow scenarios considered, and it is therefore important to have a thorough understanding of the underlying physical problem. Because upscaling is such an important part of reservoir modeling, and still has many challenges, we got motivated to consider different aspects of upscaling in this thesis. Upscaling is performed on all scales, but our primary interest is

upscaling from models with a resolution of about a meter, and up to geological models and models used for field-scale computer simulations. Our work includes investigation of the balance of forces during reservoir flooding scenarios, and how this is connected to the applicability of different upscaling methods. We also consider realistic field-scale models, and compare different upscaling methods in practice.

For oil and gas fields, and especially for offshore fields, the cost of creating the infrastructure to start producing is very large relative to the normal operational cost. Therefore, any method that increases the total recovery of a field, even by a small factor, can potentially generate large profits. This is one of the reasons why there is a great interest in enhanced oil recovery (EOR), which are methods designed to increase recovery by injection of heat, chemicals, or other substances not naturally present in the reservoir. Some more specific examples of EOR methods are injection of gas to maintain pressure, heating of the reservoir to reduce the viscosity of the oil, and injection of surfactants to lower the interfacial tension between oil and water. Another EOR method is polymer flooding, which is mainly used in reservoirs containing highly viscous oil. Polymer chains, consisting of relatively large molecules, are added to the injected water to reduce the mobility of the water solution and in this way create a more favorable displacement of oil. In onshore fields, the use of EOR methods in general, and in particular polymer flooding, has been successful and are extensively used. However, in offshore fields, there are many challenges that make the use of different EOR methods more difficult. For example, in the case of polymer flooding, the polymer chains are adsorbed by the rock and the effect of the polymer deteriorates as the solution travels through the formation. Because of the large distance between injection and production wells offshore, it is more difficult to apply polymer flooding effectively. But, if the challenges can be overcome, the use of polymer flooding may be the preferable EOR option on some offshore fields, and there is much interest in research on polymers. In particular, Statoil is currently investigating the potential of using polymers on the Norwegian Continental Shelf (NCS), as well as in other offshore locations. In this thesis, we consider modeling and simulation of polymer flooding, greatly motivated by the interest of the industry.

As discussed above, upscaling has been researched quite extensively, and several methods for performing single and two-phase flow upscaling are known and understood. However, there has been less research related to upscaling of enhanced oil recovery models. In this thesis, we investigate upscaling of models including polymer, where we extend ideas from well-established methods used for oil-water upscaling to also include polymer

properties.

Even though upscaling techniques are widespread, they do have their clear limitations and drawbacks. As already mentioned, the choice of upscaling method will always be case dependent, and there is no general method that always produces satisfactory reduced models. In addition, there are no a priori error estimates of the upscaling, and thus it is difficult to know in general how well a coarse model represents the fine-scale model. As an alternative to upscaling, different types of multiscale methods have been developed. These methods also consider the flow-problem on the coarse-scale, but in contrast to upscaling methods, a multiscale coarse model has sub-scale resolution, allowing the solution to be adapted to the fine-scale details. These methods can (sometimes greatly) reduce the computational run-time of a simulation, while maintaining the desired level of accuracy. Multiscale methods can also reduce the need for upscaling, as simulations can be run on more detailed models. Polymer flooding simulations can be particularly computationally intensive because of strong non-linearities and large mobility aspect ratios, and efficiency is therefore a challenge. In this thesis, we consider the application of a multiscale method to run complex polymer flooding scenarios in a highly effective manner.

The background part of this thesis is written to give a short overview of the mathematics and numerical methods which form the basis for the included papers. For more details and for a proper introduction to reservoir simulation in general, the novice reader is referred to one of the books written on this topic, e.g., [10, 56, 3, 16, 45]. For each of the specific subjects we discuss below, the reader is also referred to the included references for further details.

Chapter 2

Fluid Flow

To construct a mathematical description of the fluid flow in a reservoir, we need a model of the rock formation and a model for the fluid flow taking place. The representation of the rock formation is tightly coupled to the spatial discretization, as the particular grid chosen contains the geometry of the model. We will discuss this in the next chapter. For now, we just consider the reservoir rock as some arbitrary domain in 3D space.

The amount of fluids the rock is able to store is described by the *porosity*, which gives the fraction of the total volume that is made up of pore space. How well the rock is able to transport fluids is described by the *permeability*. Both these rock properties are macroscopic values, which can be thought of as averaged over each cell in the grid. The porosity reflects how much volume the pores make up in total, and the permeability reflects how well the pores are interconnected on average.

2.1 Single Phase Flow

A model for a reservoir can be considered on different scales. In this context, it is important to get an understanding of the concept of *representative elementary volumes* (REVs) [10, 1, 41]. This is a theoretical idea, where one assumes that there exist scales where the properties of the reservoir are relatively homogeneous. On such a scale, a region of the rock can be considered representative for a larger volume. The concept is illustrated for porosity in Figure 2.1. Possible REVs can be found on different scales depending on the particular reservoir, and any scale where REVs are assumed to exist is a good choice for a model scale.

Assuming there exist REVs on the particular scale considered, a mathematical model for a single phase flow is can be constructed based on the

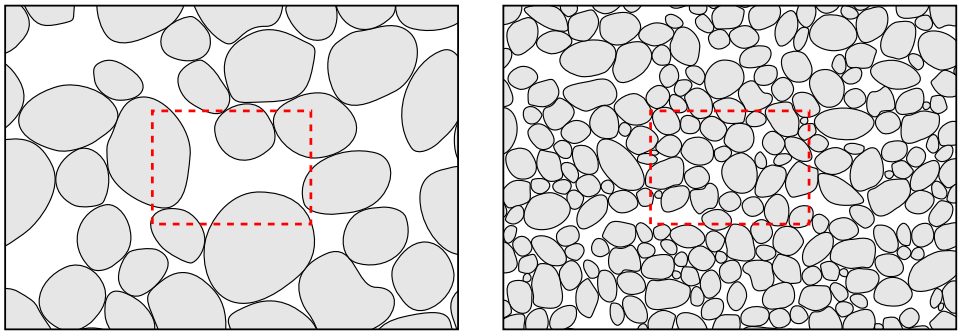

Figure 2.1: Conceptual illustration of the concept of representative elementary volumes (REVs) for porosity. Left: at the scale of the pore sizes, the rock is highly heterogeneous and the region in red square is not representative for the whole domain shown. Right: for a larger scale, the domain is more homogeneous, and the red square might be considered representative.

fundamental law of mass conservation and continuity of the flow. The accumulation of mass of the fluid inside any control volume must be balanced by the flow over its boundaries. If compressibility is included in the model, the compression of the fluid and the rock must also be accounted for in the mass balance. In addition, there might be sources or sinks present, which in a reservoir is typically a well or an aquifer. By considering the mass balance in a control volume, one can derive the continuity equation

$$\frac{\partial}{\partial t}(\phi\rho) + \nabla \cdot (\rho\vec{v}) = \rho q. \tag{2.1}$$

Here, $\phi(x)$ is the porosity, which is function of the position in space, ρ is the density of the fluid, $\vec{v}$ is the fluid velocity vector and q is a sink/source term. The fluid velocity is proportional to the pressure drop in the domain, which is a fundamental relationship first discovered by Henry Darcy though experiments of flow of water through sand. Today, this relationship is referred to as Darcy's law, and reads

$$\vec{v} = -\frac{\mathbf{K}}{\mu}\left(\nabla p - \rho g \nabla z\right), \tag{2.2}$$

where $\mathbf{K}(x)$ is the permeability, μ is the viscosity of the fluid, p is the pressure, g is the gravitational acceleration and z is the vertical coordinate. In general, the permeability $\mathbf{K}(x)$ is a tensor, which means that the permeability varies depending on the direction of flow (it is anisotropic), and also that a pressure drop in one direction may induce flow in another direction.

For some reservoir models, the directional dependency is considered small, and the permeability tensor is replaced by a scalar and the permeability is said to be isotropic. Both the density and viscosity depend in general on pressure and temperature, but we do not consider temperature dependence in this thesis.

2.2 Two-Phase Flow

In a reservoir, there are normally more than one phase present, and it is common to distinguish between the oil phase, the gas phase and the water phase. Each phase may also consist of several different components. E.g., the oil phase may contain several types of hydrocarbons with different properties. We consider now a system with two phases, where each phase only contains a single component, and for the sake of presentation, we let these phases be oil and water. For a two-phase system, the pore space is shared between the two fluids, as oppose to a single phase system, where the one fluid occupies the entire pore volume. We consider immiscible fluids, meaning that on the pore-scale, the phases stay separated and do not mix with one other. This separation is caused by interfacial tension between the two fluids. However, when considering some REV on a larger scale, the two fluids occupy the same space in an average sense. To account for the volume of each fluid present, the *phase saturations* are introduced, which give the amount of the pore volume occupied by each phase. The saturations of oil and water are denoted respectively by s_o and s_w. It is assumed that the two phases together occupy the entire pore volume, and thus the saturations must always sum to one.

As both phases are present in the pore space, each phase will experience a reduction in the ability to flow as the other phase restricts the pathway through the pore network. On the macro-scale, this is reflected in a reduction of the permeability. Each phase α experiences its own *phase permeability* $\mathbf{K}_\alpha$, which always will be less than or equal to the permeability $\mathbf{K}$ experienced by a single fluid in the same rock formation. How large this reduction is, will depend on the phase saturations, and to model this dependency, we introduce the *relative permeability* functions $k_{r\alpha}$, which are defined such that $\mathbf{K}_\alpha = k_{r\alpha}(s_\alpha)\mathbf{K}$. The permeability will be reduced if there is more of the other fluid present to restrict the flow, and thus the relative permeabilities are (usually monotone) increasing functions of the phase saturation. An example of a typical pair of relative permeability functions for oil and water is shown in Figure 2.2, where both curves are expressed as a function of the water saturation. Note that the curves to not span the

whole saturation domain from 0 to 1. This is because some of the fluids will be immobile (unable to flow) because of trapping in the pore network and interfacial tension between the fluids, and between the fluid and the rock.

Between a fluid and a solid, there are attractive forces causing the fluid to stick to the solid surface (an effect called adhesion). In the reservoir, oil and water have different interaction forces with the rock surface. This causes one of the phases to be more attracted to the rock than the other, and that phase is known as the wetting phase. Reservoirs are most often found to be water-wet, such that water is the wetting-phase, but this is not always the case. The wettability may also vary within a reservoir and may change depending on the substances present.

Due to the interfacial tension between the fluids on the pore-scale, the pressure inside each fluid will be different at equilibrium (when there is no flow taking place). This is expressed on the macro-scale by the *capillary pressure*, and is normally defined as $p_{\text{cow}} = p_o - p_w$, the difference between the oil pressure and the water pressure. The phase pressure is higher for the wetting phase, and thus p_{cow} is positive for a water-wet system. The capillary pressure is a function of the saturation, and an example of such a function for an intermediate-wet system is shown in Figure 2.2.

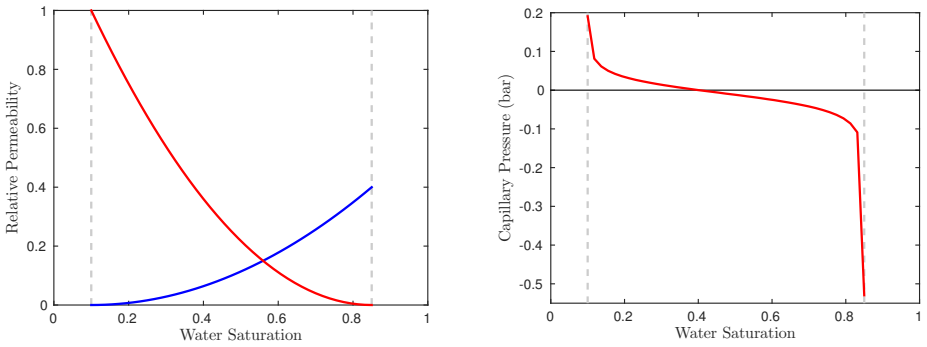

Figure 2.2: Examples of two-phase properties. Left: relative permeability curves, with k_{ro} in red and k_{rw} in blue. Right: a capillary pressure curve for an intermediate-wet system.

The fluid behavior in a reservoir depends on both pressure and temperature. In general, mass may be transferred between phases, and the amount of different chemical components in each phase may change. E.g., a hydrocarbon compound may be released from the oil phase into the gas phase if pressure decreases. Also, the density and viscosity of a fluid changes with pressure and temperature. How this fluid behavior is described mathematically is referred to as the pressure-volume-temperature (PVT) model.

A compositional model treats each chemical component separately and ensures mass conservation of each of these. An alternative and commonly used simplified PVT model, is the so-called *black-oil model* [66], where all hydrocarbons are assumed to be either oil or gas at surface conditions, and the composition of each of the phases is not considered. However, for a three-phase model at reservoir conditions, the oil phase can be dispersed in gas, and the gas phase can be dissolved in oil, depending on the pressure. The volume of each phase at reservoir conditions is also assumed to depend on pressure, and this dependence is included by the *formation volume factor* B_α, which is given by

$$B_\alpha = \frac{\text{volume of phase } \alpha \text{ at reservoir conditions}}{\text{volume of phase } \alpha \text{ at standard (surface) conditions}}.$$

We consider here the two-phase black-oil model for oil and water. This can be considered an extension of the single phase model discussed above, where now the mass of each phase has to be conserved. As we use the black-oil formulation, the density in each of the phase equations is expressed in terms of the formation volume factor as $\rho_\alpha = \rho_{\alpha,s}/B_\alpha$, where $\rho_{\alpha,s}$ is the phase density at surface conditions. Because $\rho_{\alpha,s}$ is assumed to be a constant, it is subsequently divided away. The two-phase continuity equations for oil and water are then given by

$$\frac{\partial}{\partial t}\left(\frac{\phi s_o}{B_o}\right) + \nabla \cdot \left(\frac{\vec{v}_o}{B_o}\right) = \frac{q_o}{B_o}, \tag{2.3a}$$

$$\frac{\partial}{\partial t}\left(\frac{\phi s_w}{B_w}\right) + \nabla \cdot \left(\frac{\vec{v}_w}{B_w}\right) = \frac{q_w}{B_w}, \tag{2.3b}$$

where for each phase α, $\vec{v}_\alpha$ is the phase velocity and q_α is a sink/source term. Darcy's law is extended to include two phases, and the phase velocities are given by

$$\vec{v}_o = -\frac{k_{ro}}{\mu_o}\mathbf{K}\left(\nabla p_o - \rho_o g \nabla z\right), \tag{2.4a}$$

$$\vec{v}_w = -\frac{k_{rw}}{\mu_w}\mathbf{K}\left(\nabla p_w - \rho_w g \nabla z\right). \tag{2.4b}$$

In addition to the previously introduced quantities, μ_α denotes the phase viscosity and ρ_α the phase density.

Disregarding any wells in the system, the unknowns of the equations are the saturation s_o and s_w, and the phase pressures p_o and p_w. Thus, we have two equations and four unknowns. In order to create a complete model, we

need additional closing relations. To this end, we use the assumption that the saturations always have to sum to one, given by $s_o + s_w = 1$, and the capillary pressure function, given by $p_{\text{cow}}(s_w) = p_o - p_w$.

2.3 Two-Phase Flow With Polymer

As discussed in the introduction, polymer flooding is an enhanced oil recovery method where water-soluble polymers are added to the water before it is injected into the reservoir. The mathematical model of polymer flooding we consider [27], is an extension of the black-oil two-phase equations for oil and water presented above, where the polymer is included in the water phase. The polymer concentration c_p is given in units of mass per volume of water. It is assumed that the presence of polymer changes the properties of the water, but does not influence the properties of the oil phase. The conservation equations for oil, water, and water with polymer are

$$\frac{\partial}{\partial t}\left(\frac{\phi s_o}{B_o}\right) + \nabla \cdot \left(\frac{\vec{v}_o}{B_o}\right) = \frac{q_o}{B_o}, \quad (2.5a)$$

$$\frac{\partial}{\partial t}\left(\frac{\phi s_w}{B_w}\right) + \nabla \cdot \left(\frac{\vec{v}_w}{B_w}\right) = \frac{q_w}{B_w}, \quad (2.5b)$$

$$\frac{\partial}{\partial t}\left(\frac{(1 - s_{\text{ipv}})\,\phi s_w c_p}{B_w}\right) + \frac{\partial}{\partial t}\Big((1 - \phi_{\text{ref}})\rho_r c_a\Big) + \nabla \cdot \left(\frac{c_p \vec{v}_p}{B_w}\right) = \frac{q_p}{B_w}, \quad (2.5c)$$

and the Darcy velocities are now given by

$$\vec{v}_o = -\frac{k_{ro}}{\mu_o}\mathbf{K}\left(\nabla p_o - \rho_o g \nabla z\right), \quad (2.6a)$$

$$\vec{v}_w = -\frac{k_{rw}}{\mu_{w,\text{eff}} R_k}\mathbf{K}\left(\nabla p_w - \rho_w g \nabla z\right), \quad (2.6b)$$

$$\vec{v}_p = -\frac{k_{rw}}{\mu_{p,\text{eff}} R_k}\mathbf{K}\left(\nabla p_w - \rho_w g \nabla z\right). \quad (2.6c)$$

Compared to the two-phase equations (2.3), we have now introduced one extra equation and one extra unknown with the polymer concentration c_p. Thus, as the two closing relations used for two phase flow still apply, $s_w + s_o = 1$ and $p_{\text{cow}}(s_w) = p_o - p_w$, we have a complete model. There are several new parameters introduced in these equations. Each of them are explained in the following, together with an discussion of the different physical effects they model.

Viscosity influence

When polymer is solved in the water, the viscosity of the solution is increased. In our equations, this effect is modeled by effective viscosity functions that depend on the polymer concentration. The effective viscosities of water and polymer are denoted by $\mu_{w,\text{eff}}$ and $\mu_{p,\text{eff}}$, respectively, and they are defined using the Todd–Longstaff mixing model [65]. The viscosity of a fully mixed solution of water and polymer is denoted by $\mu_m(c_p)$, and the effective polymer viscosity is given by

$$\mu_{p,\text{eff}} = \mu_m(c_p)^\omega \mu_p^{1-\omega}.$$

In this expression, $c_{p,\max}$ is the maximum possible polymer concentration, $\mu_p = \mu_m(c_{p,\max})$, and $\omega \in [0,1]$ is the Todd–Longstaff mixing parameter. For $\omega = 1$, the polymer solution and the water are fully mixed, whereas for $\omega = 0$ the polymer solution is completely segregated from the pure water. Values of ω in between 0 and 1 model partial mixing. The viscosity of partially mixed water is defined as

$$\mu_{w,e} = \mu_m(c_p)^\omega \mu_w^{1-\omega}.$$

The effective water viscosity $\mu_{w,\text{eff}}$ is then given by

$$\frac{1}{\mu_{w,\text{eff}}} = \frac{1 - c_p/c_{p,\max}}{\mu_{w,e}} + \frac{c_p/c_{p,\max}}{\mu_{p,\text{eff}}}.$$

Inaccessible pore volume

Polymer chains are large in size compared to the water and hydrocarbon molecules in the reservoir, and because of this, parts of the pore-volume may not be accessible to the polymer. Thus, polymer has an effective pore space that is smaller than the other fluids, which may result in an accelerated polymer flow. This effect is included in (2.5c) with the parameter s_{ipv}, which is the fraction of the pore volume not accessible to polymer, commonly referred to as the *inaccessible pore volume* or *dead pore space*.

The model used in (2.5c) for the inaccessible pore volume is the conventional model, used in several reservoir simulators. However, this method can lead to an ill-posed problem. In Paper V, this problem is discussed in detail and other models are suggested.

Adsorption

The polymer molecules may get attached to the rock surface inside the reservoir, and this effect is known as adsorption. As the polymer then is

removed from the flow, this reduces the polymer concentration in the solution, and consequently the viscosity effect becomes smaller. The adsorption function $c_a(c_p)$ gives the relationship between the polymer concentration and the amount of adsorbed polymer.

Permeability reduction

The increased viscosity causes a mobility-reduction of the water-polymer solution. However, some types of polymer also experience a reduction in the permeability [40], further reducing the mobility. This effect can be explained by the adsorption, as the large polymers attached to the rock reduce the effective pore size for the flowing polymer solution. The permeability reduction effect is modeled by the reduction factor R_k, defined by

$$R_k(c_p) = 1 + (R_{RF} - 1)\,\frac{c_a(c_p)}{c_{a,\max}}, \tag{2.7}$$

where $R_{RF} \geq 1$ is called the residual resistance factor and $c_{a,\max}$ is the maximum adsorption.

Non-Newtonian behavior

For a polymer solution at low shear rates, there is a linear relationship between the shear stress and the shear rate, and the solution is a Newtonian fluid. However, at higher shear rates, the solution shows non-Newtonian behavior. The viscosity typically decreases with higher shear rates, an effect known as *shear-thinning*, which is caused by the uncoiling and unsnagging of polymer chains when they are elongated in shear flow [40]. Throughout the reservoir, the flow-rates are usually low and so are the shear stresses. But near the injection well, the shear rates can be large and the effect of shear-thinning can be important. The shear-thinning is not seen in the equations (2.5), but this is discussed in detail in Paper IV, where also shear-thinning is included in a multiscale solver.

Chapter 3

Discretization and Simulation

3.1 Grid Structures

The reservoir rock formation is represented by a discrete grid, where each cell in the grid is assumed to have constant properties. There is a variety of different grid structures, spanning in complexity from simple Cartesian grids to fully unstructured grids. Two examples of grids are shown in Figure 3.1.

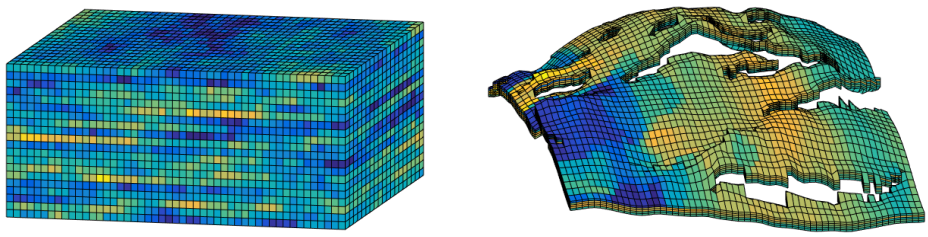

Figure 3.1: Two examples of reservoir model grids with their porosity fields plotted. Left: a Cartesian grid represented by a section of the SPE10 model [19]. Right: a more complex grid with faults represented by a section of the SAIGUP model [48] (this particular realization can be downloaded using MRST [64]).

If the grid structure is created from a real reservoir, it may contain faults and fractures, and grid cells can be degenerated or have large aspect ratios. In addition, grids are often refined to increase the resolution in certain areas, such as in the near-well regions. All this contribute to very complex model geometry, requiring numerical methods which can be applied

to unstructured grids. Reservoir models also continue to grow in size, and can today contain multimillion cells, putting further requirements on both solution algorithms and computational power.

3.2 Discretization of the Flow Equations

In order to apply the mathematical flow models presented above to a grid, we need some form of spatial discretization scheme. There is a wide variety of different schemes based on finite difference, finite-volume and finite-element methods. In this thesis, we consider finite-volume methods, and in particular the two-point flux approximation (TPFA) scheme.

To present the TPFA scheme in the following, we consider the discretization of the single phase flow equation (2.1) on a rectilinear grid, which is a grid where all cells are cuboids (or rectangles in 2D), and we assume that the grid is aligned with the principle coordinate directions. To simplify the presentation, we neglect gravity, assume the permeability is isotropic, the viscosity is constant and that the rock and the fluid are incompressible. The continuity equation for one-phase flow (2.1) then simplifies to

$$\nabla \cdot \vec{v} = q, \qquad \vec{v} = -\frac{K}{\mu}\nabla p, \tag{3.1}$$

where K now is a scalar. We also impose no-flow boundary conditions on the domain.

A finite volume method has a clear physical motivation. Each cell in the grid is considered a control volume, and then mass conservation is imposed on each cell volume. This approach is quite similar to the construction of the continuous differential equations, where mass conservation is imposed on all control volumes in the continuous sense.

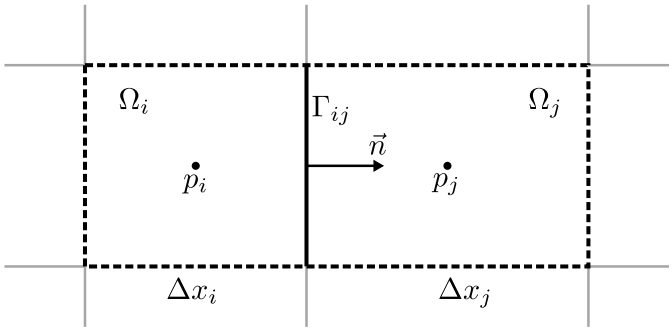

Figure 3.2: Illustration of finite volume discretization on a rectilinear grid.

Consider now a cell Ω_i in the grid, as illustrated in Figure 3.2. To impose mass balance over the cell volume of Ω_i, the equation (3.1) is integrated over the volume of the cell to obtain

$$\int_{\Omega_i} \nabla \cdot \vec{v} \, dV = \int_{\Omega_i} q \, dV.$$

Applying the divergence theorem to the volume integral on the left hand side, we obtain a surface integral over the boundary $\partial\Omega_i$ of the cell. The interface with each adjacent cell j is denoted Γ_{ij}, and we write the surface integral as a sum over all interfaces. We get

$$\int_{\partial\Omega_i} \vec{v} \cdot \vec{n} \, dA = \sum_j \int_{\Gamma_{ij}} \vec{v} \cdot \vec{n} \, dA = \int_{\Omega_i} q \, dV, \tag{3.2}$$

where the flux $\vec{v}$ is evaluated on the boundary of the cell and $\vec{n}$ is a unit normal vector out of the boundary. Considering the boundary Γ_{ij} in Figure 3.2 as an example, we have to evaluate on the boundary

$$\vec{v} \cdot \vec{n}\Big|_{\Gamma_{ij}} = -\left(\frac{K}{\mu}\nabla p \cdot \vec{n}\right)\Big|_{\Gamma_{ij}} = -\left(\frac{K}{\mu}\frac{\partial p}{\partial x}\right)\Big|_{\Gamma_{ij}}.$$

Both the pressure and the permeability is assumed constant on each cell, and are not well defined on the interface between two cells. Thus, both properties have to be approximated on the interface to obtain a value for the flux. In the TPFA method, the gradient of the pressure is approximated by the pressure drop between the two cell-centers (hence the name *two-point* flux approximation). That is,

$$\frac{\partial p}{\partial x}\Big|_{\Gamma_{ij}} \approx \frac{2(p_i - p_j)}{\Delta x_i + \Delta x_j}.$$

The permeability is approximated as the distance-weighted harmonic mean of the two cell permeabilities, such that

$$K\Big|_{\Gamma_{ij}} \approx K_{ij} = (\Delta x_i + \Delta x_j)\left(\frac{\Delta x_i}{K_i} + \frac{\Delta x_j}{K_j}\right)^{-1}.$$

The flux is considered constant over the whole face, and thus the total flux over Γ_{ij} is obtained by multiplying by face area $|\Gamma_{ij}| = A_{ij}$. The discrete equation (3.2) for cell Ω_i can now be written as

$$-\sum_j \frac{1}{\mu} T_{ij}(p_i - p_j) = \int_{\Omega_i} q \, dV, \tag{3.3}$$

where all the constant grid related factors have been collected into the *transmissibility* T_{ij}. For the particular interface considered above, the transmissibility is given by

$$T_{ij} = A_{ij} \frac{2}{\Delta x_i + \Delta x_j} (\Delta x_i + \Delta x_j) \left(\frac{\Delta x_i}{K_i} + \frac{\Delta x_j}{K_j} \right)^{-1}.$$

For any grid, the finite volume discretization may be written on the form (3.3), but the transmissibilities will be different depending on the particular grid and on the discretization method chosen. The TPFA method may be generalized to varying cell sizes, and also to unstructured grids, where the angle from the face center to the cell centers also changes. However, the method suffers from so called grid-orientation effects, where the solution will depend on the particular geometry of the grid. For a discussion of the TPFA method on general grids, including examples of its weaknesses, see [46].

An important reason for introducing the transmissibilities, is that they are independent of the fluid flow and constant for a given grid, also for multi-phase simulations. Thus, a simulator can pre-compute all the transmissibility values before the simulation starts. We also note that the same is true for the divergence and gradient, where discrete versions of the operators can be pre-computed [37, 45].

In the two-phase equations, the phase mobility $\lambda_\alpha = k_{r\alpha}/\mu_\alpha$, which is highly dependent on the saturation because of the relative permeability, also has to be evaluated on the interface between the adjacent cells. Though it may initially seem like a simple average between the two cells would suffice, this turns out that this will create highly unstable numerical schemes. A much better approach, which is the common solution, is to perform a so-called *upstream-weighting* of the mobilities. Then the saturation on the interface is set equal to the saturation of the cell upstream, i.e., where the flow is coming from.

3.3 Fully Implicit Solver

A commonly used solution strategy of the conservation equations is to solve them as a coupled system by using a fully implicit Newton-Raphson solver. For two-phase flow, this means solving (2.3) for both pressure and saturation simultaneously. By defining $x = [p_o, s_w]^T$, we first write (2.3) on residual

form as

$$F(x) = \begin{bmatrix} \frac{\partial}{\partial t}(\phi s_o b_o) + \nabla \cdot (\vec{v}_o b_o) - q_o b_o \\ \frac{\partial}{\partial t}(\phi s_w b_w) + \nabla \cdot (\vec{v}_w b_w) - q_w b_w \end{bmatrix} = 0,$$

where we have used the notation $b_\alpha = 1/B_\alpha$. By then discretizing this system in time and space, the discrete equations can be solved by the classic Newton-Raphson method through iterations of the form

$$x^{n+1} = x^n - J^{-1}(x^n)F(x^n),$$

where J is the Jacobian matrix of F. Newton's method is known to be robust and can often give quadratic convergence. However, the method requires an accurate calculation of the Jacobian matrix. For simple systems, this is straight forward differentiation which can be done analytically, but as the equations become more complex, such a calculation become both time-consuming and can easily contain errors. However, in an implementation, the value of the Jacobian can be computed automatically by the use of *automatic differentiation*, removing the need for a tedious analytical calculation. This technique is extremely powerful, but surprisingly simple to implement, at least in a language supporting object-orientation. We will not explain the concept of automatic differentiation herein, but an introduction can be found in e.g. [53], which also shows implementation using MATLAB.

The open source reservoir simulator MRST [64] uses automatic differentiation and operator overloading in Matlab to abstract away the construction of Jacobians [37]. By also using discrete operators, the equations can be written in the code on the same form as they would be written on paper. This greatly simplifies the implementation, and makes complex flow physics relatively easy to include.

3.4 Sequential Solver

In a multiphase system, we have to solve for both pressures and saturations, and these two properties have very different mathematical behavior. The pressures of the system show a behavior which is typical for an elliptic equation, while the transport of the saturations has a hyperbolic character. Because of this difference, another common solution strategy is to split the conservation equations into a pressure part and a transport part, and then solve these equations separately. Such a solution strategy is often referred to as a *sequential solver* [16, 43, 66], and it allows for the use of

different numerical methods, which can take advantage of the mathematical characteristics of each equation. One such sequential strategy which has been extensively used in reservoir simulation, is the IMPES method [22], applying an implicit solver for the pressure equation, and an explicit solver for the saturation transport.

In order to apply a sequential numerical scheme, the conservation equation must be divided into a pressure equation and a transport equation. Let us consider how this can be done for the two-phase black oil equations (2.3). To keep notation simpler, we assume in the following that the fluids and the rock are incompressible and we also disregard gravity and capillary pressure. The construction of the sequential formulation without these simplifications are given with similar notation in Paper IV.

Time Discretization

The first step in constructing the sequential formulation is to discretize the two-phase continuity equation (2.3) in time using implicit Euler to obtain the semi-discrete equations

$$\frac{\phi}{\Delta t}\left(s_o^{n+1} - s_o^n\right) - \nabla \cdot \left(v_o^{n+1}\right) = q_o^{n+1}, \tag{3.4a}$$

$$\frac{\phi}{\Delta t}\left(s_w^{n+1} - s_w^n\right) - \nabla \cdot \left(v_w^{n+1}\right) = q_w^{n+1}, \tag{3.4b}$$

where superscript denotes the discrete time and $\Delta t = t^{n+1} - t^n$.

Pressure Equation

To obtain an equation for the pressure alone, we need to eliminate the saturations at the next time-step. To this end, sum the oil and water equations to obtain

$$\frac{\phi}{\Delta t}\left(s_o^{n+1} + s_w^{n+1} - s_o^n - s_w^n\right) - \nabla \cdot \left(v_o^{n+1} + v_w^{n+1}\right) = q_o^{n+1} + q_w^{n+1}.$$

As the saturations always sum to one, the first term is zero, and we are left with

$$-\nabla \cdot \left(v_o^{n+1} + v_w^{n+1}\right) = q_o^{n+1} + q_w^{n+1}.$$

Now, the fluxes v_o^{n+1} and v_w^{n+1} both depend on the saturation at the next time-step. To remove this dependency, the relative permeabilities are in-

stead evaluated using s_w^n, and the phase fluxes are replaced by

$$v_o^{n+1/2} = -\frac{\mathbf{K}k_{ro}(s_o^n)}{\mu_o(p^{n+1})}\nabla p^{n+1},$$
$$v_w^{n+1/2} = -\frac{\mathbf{K}k_{rw}(s_w^n)}{\mu_w(p^{n+1})}\nabla p^{n+1}.$$

We denote the fluxes with discrete time $n + 1/2$ to emphasize that they are computed using the saturations at time n and pressure at time $n + 1$, and can in this way be thought of as intermediate fluxes. With these phase fluxes, the pressure equation that we solve, written in residual form, then becomes

$$r = -\nabla \cdot \left(v_o^{n+1/2} + v_w^{n+1/2}\right) - q_o^{n+1} + q_w^{n+1} = 0.$$

Using a standard two-point flux approximation (TPFA) as the spatial discretization, this residual equation is solved using Newton's method, where in each iterations, one has to solve the linearized system

$$-J\Delta p = r, \tag{3.6}$$

where J is the Jacobian of r. Once the pressure at the next time-step has been found to an acceptable tolerance, the total flux $v_T = v_o^{n+1/2} + v_w^{n+1/2}$ is computed, which will be used in the transport equation.

Transport Equation

To construct the transport equation, we express the phase fluxes in terms of the total flux, and we find that

$$v_T = v_o + v_o = -\lambda_o \mathbf{K}\nabla p - \lambda_w \mathbf{K}\nabla p \quad \Longrightarrow \quad \nabla p = -\frac{\mathbf{K}^{-1}v_T}{\lambda_o + \lambda_w},$$

where the mobilities are given as $\lambda_\alpha = k_{r\alpha}/\mu_\alpha$. Inserting this expression for ∇p into the phase fluxes, we obtain

$$v_o^{n+1} = f_o^{n+1}v_T, \qquad v_w^{n+1} = f_w^{n+1}v_T,$$

such that the phase fluxes now are expressed in terms of the total flux. Here,

$$f_\alpha = \frac{\lambda_\alpha}{\lambda_o + \lambda_w} = \frac{k_{r\alpha}/\mu_\alpha}{k_{rw}/\mu_w + k_{ro}/\mu_o} \tag{3.7}$$

is the fractional flow of phase $\alpha \in \{o, w\}$.

We then choose either the oil or the water equation in (3.4) to solve for. If we choose the oil equation, then we solve

$$\frac{\phi}{\Delta t}\left(s_o^{n+1} - s_o^n\right) - \nabla \cdot \left(f_o^{n+1} v_T\right) = q_o^{n+1},$$

to obtain the oil saturations at the next times step, s_o^{n+1}. Once this equation is solved, we let water fill up the remaining void and set $s_w^{n+1} = 1 - s_o^{n+1}$.

3.5 Reservoir Simulators

There are several reservoir simulators available for use. Some are for commercial use, such as e.g., ECLIPSE[1] and INTERSECT[2], which are both developed by Schlumberger, and the CMG suite[3] developed by Computer Modelling Group Ltd. But there are also free and open source simulators, which are especially useful for students and researchers. Of particular interest are the two projects OPM[4] (The Open Porous Media initiative) and MRST (Matlab Reservoir Simulation Toolbox) [64, 45, 37]. OPM is written in C++, and is a collaboration project mainly by Statoil, SINTEF, IRIS and Ceetron Solutions. MRST is a toolbox for Matlab, which is developed by SINTEF Applied Mathematics.

In this project, all implementation is based on MRST. This is a comprehensive collection of routines for grid handling, discretization, solver, and work-flow tools. The main advantage of using an open source framework as a foundation in the context of research, is that the basic grid handling and most common solvers are already implemented. Thus, there is no need to spend a considerable amount of time getting a basic code up and running, but instead, it is possible to dive right into complex and fascinating methods and examples. MRST also takes advantage of automatic differentiation, which we discussed in Section 3.3, to greatly simplify the implementation of implicit methods. The use of automatic differentiation in MRST is further discussed in [37].

The latest release of MRST is available for download at `www.sintef.no/MRST/` under the terms of the GNU General Public License (GPL). For a thorough introduction to MRST, and also for an extensive introduction to reservoir simulation in general, see [45], parts of which are also available for download on the MRST web page.

[1] `http://www.software.slb.com/products/eclipse`
[2] `http://www.software.slb.com/products/intersect`
[3] `http://www.cmgl.ca/`
[4] `http://opm-project.org/`

Chapter 4

Upscaling and Multiscale Methods

4.1 Upscaling

Upscaling of a reservoir model is the process of coarsening the grid, creating fewer and larger cells, at the same time as the physical dimensions and total pore volume are kept constant. The coarse model should in addition be a good representation of the fine-scale (original) model, by e.g., producing similar flow patterns as the fine-scale model during simulation. In the process of upscaling, each physical property of the model needs to be upscaled or averaged in some sense, to the coarser model. The original fine-grid is partitioned into a set of coarse grid blocks, each of which is upscaled to a single cell in the coarse model as illustrated in Figure 4.1.

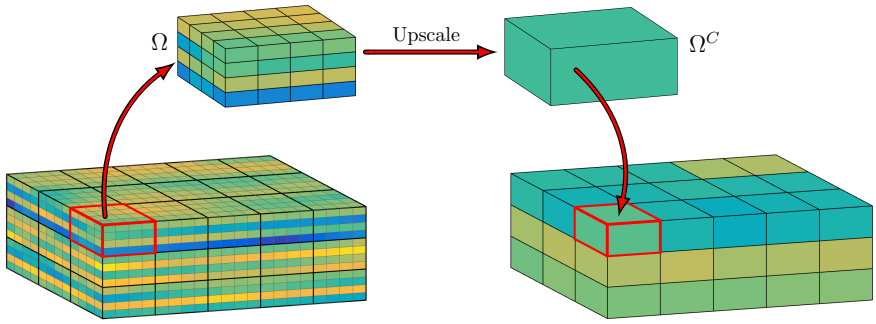

Figure 4.1: Conceptual illustration of upscaling a fine-scale grid to a coarse-scale grid. The fine-scale grid is partitioned into grid blocks, where each block is upscaled in turn to a single coarse cell.

4.2 One-Phase Upscaling

One-phase upscaling has been studied quite extensively, and papers giving an overview of different methods include [69, 60, 29, 25]. Maybe the simplest upscaling method is to use *sampling*, where a block is given the permeability value at its center. This method does not take into account the change of scales involved in the upscaling, and disregard any heterogeneities within the block, but it has still been commonly used in the industry [60]. Simple permeability averages have also been extensively used. It was shown in [13] that the upscaled permeability must lie in between the arithmetic and harmonic averages, and for simple layered models, these averages will give exact upscaling (examples of this are given below on page 24). It was later suggested in [35] to use general *power averages* as an improvement to compute upscaled permeabilities. One of the main weaknesses of the power averages, however, is that the value of the power is case-dependent, and there is no simple way of computing its value a priori [69].

The use of *renormalization* was suggested for 2D grids in [36] to calculate upscaled permeabilities. This is a recursive method which computes the equivalent permeability of only a few cells at a time to obtain a slightly coarser grid. The calculations are then repeated until the desired grid size is reached. The renormalization method has later been extended to 3D grids and also to produce full upscaled tensors [30]. The method is fast to compute, and have shown good results for lognormal permeability fields. However, for models with strong anisotropy, the upscaling can be poor [69].

Another large class of upscaling methods are the *flow-based methods*, which solve some flow problem on the fine-scale grid block, and use the resulting solution to compute effective permeabilities. The flow-based methods can further be sub-categorized as either a local or non-local, depending on the domain taken into account when upscaling a grid block.

Local methods consider each block that is to be upscaled individually, and solve a flow-problem on the fine-scale block by imposing some set of boundary conditions. One choice of boundary conditions is to apply a linear pressure drop in one direction, and impose no-flow on the other boundaries. Relatively early use of this method can be found in [12, 11]. By computing one flow solution in each direction, one obtains an upscaled diagonal permeability tensor. To account for cross-flow, it was suggested in [24] to use periodic boundary conditions, which will produce full upscaled permeability tensors. The use of uniform boundary conditions, which has linear pressure drop imposed along the boundaries parallel to flow, has also been suggested. This will also produce upscaled tensors, but these will not be symmetric, as

opposed to those obtained using periodic conditions [60].

As the local methods do not include any information from the surrounding fine-scale cells, they are unable to capture effects of larger heterogeneity correlations of the model, which are important for the global flow patterns. To account for more of the surrounding heterogeneities, a *non-local method* (also referred to as an *oversampling method*) considers a region of the fine-scale grid which is larger than the grid block that is to be upscaled. The extra region around the block included in the flow solution may be referred to as the *skin*, the *flow jacket* or the *oversampling region*.

If the oversampling region covers the entire domain, the method is referred to as a *global method*. The first non-local method suggested [70] was a global method, where the flow problem was solved on the entire domain multiple times using different boundary conditions. From the solutions, upscaled transmissibilities are computed. It was later suggested in [31] to use a larger domain than the coarse cell, but smaller than the whole grid, and we refer to such a method as *local-global*. As a global method can be computationally expensive, a local-global method may be seen as a trade-off between included information and computational cost. Some more recent work on non-local methods include both global methods [71, 15] and local-global methods [68, 4].

As there are many sources of uncertainty when creating a model of a reservoir, the fine-scale permeability field may be given as random variables with some probability distribution. To perform upscaling of such models, a number of *stochastic methods* have been applied. For more on such methods, see the discussion in [60] and the references therein. Upscaling is a large topic, and other methods which are not discussed above include percolation theory, effective media, streamline methods and elastic grids. We refer to the review articles [69, 60] for more information.

In the following, we will introduce the upscaling methods we mostly use in this thesis. We consider upscaling of a single grid block Ω containing a set of cells in the fine-scale grid. This grid block is to be upscaled to a single coarse cell Ω^c, as illustrated in Figure 4.1. For a one-phase system, the properties that need to be upscaled are porosity and permeability.

Porosity Upscaling

For porosity, the upscaling is usually performed by a simple volume averaging, where for each grid block Ω, the upscaled porosity is given by

$$\phi^* = \frac{\int_\Omega \phi(x)dx}{\int_\Omega dx},$$

where ϕ^* denotes the upscaled value of ϕ. Note that this method conserves the total pore volume of the model, which is an important property.

Permeability Upscaling

When upscaling the permeability of a grid block Ω, one would ideally want an upscaled (effective) permeability $\mathbf{K}^*$ which gives the same total flux in the grid block as the original permeability, given the same pressure field. That is, one would like to impose

$$\int_\Omega \mathbf{K}(x)\nabla p \, dV = \mathbf{K}^* \int_\Omega \nabla p \, dV. \tag{4.1}$$

In general however, it is not possible to find an upscaled tensor $\mathbf{K}^*$ such that this equation is fulfilled for any pressure field. The problem of finding a K^* that satisfies (4.1) for all pressure fields is highly over-determined and the equation does not have a solution. In particular, this means that when imposing (4.1) on the grid block Ω, the upscaling is highly dependent on the boundary conditions of the block. Also note that if a particular pressure field is given, the value of $\mathbf{K}^*$ is not unique, and so the problem is under-determined.

Averaging

One of the simplest methods for upscaling the permeability is to perform a power average [35]. We assume in this section that the original permeability is scalar. For a choice of the parameter p, the upscaled permeability K^* is given by

$$K^* = \left(\frac{\int_\Omega K(x)^p dx}{\int_\Omega dx}, \right)^{1/p}, \quad -1 \leq p \leq 1.$$

Special cases of the power average are the *arithmetic average* ($p = 1$), and the *harmonic average* ($p = -1$). For a one-dimensional model, the harmonic average gives the correct upscaling. Also, for a two-dimensional perfectly layered model, the harmonic average will give correct upscaling if the layers are normal to the flow direction, and the arithmetic average will be correct if the layers are parallel to the flow direction. This can easily be shown. First, consider a horizontally layered model as shown in Figure 4.2 where we impose a pressure drop Δp to induce flow from west to east. We upscale the whole model Ω to a single cell. The total flux of the fine-scale model,

$$v_f = \int_\Omega v(x,y) \, dA = -L \int_0^H K(y) \frac{\partial p}{\partial x} \, dy = -L \int_0^H K(y) \frac{\Delta p}{L} \, dy,$$

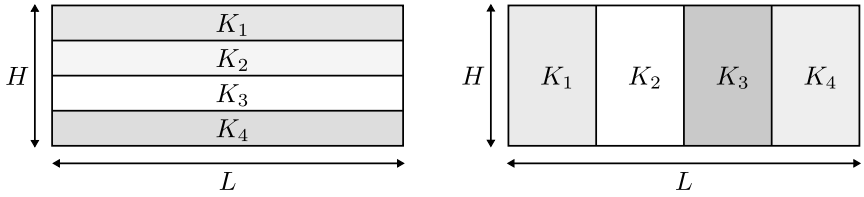

Figure 4.2: Illustration of perfectly layered models.

should match the total flux on the coarse scale,

$$v_c = -\int_\Omega K^* \frac{\Delta p}{L}\, dA = -K^* \frac{\Delta p}{L} HL.$$

Thus, the correct upscaled permeability equals the arithmetic average

$$K^* = \frac{1}{H}\int_0^H K(y)\, dy.$$

Consider then the vertically layered model as shown in Figure 4.2, where we again impose a pressure drop Δp to induce flow from west to east. As the pressure drop on the whole model is known, we have

$$\Delta p = \int_0^L \frac{\partial p}{\partial x}\, dx.$$

Darcy's law applied everywhere on the fine scale, and thus we also have

$$\int_0^L \frac{\partial p}{\partial x}\, dx = \int_0^L -\frac{v}{K(x)}\, dx.$$

From the conservation equation we have $\nabla \cdot v = 0$, and so the flux is constant. This means that v is also equal to the coarse scale flux, and we get

$$\Delta p = \int_0^L \frac{\partial p}{\partial x}\, dx = \int_0^L -\frac{v}{K(x)}\, dx = K^* \frac{\Delta p}{L} \int_0^L \frac{1}{K(x)}\, dx.$$

This implies that the upscaled permeability is given by the harmonic average

$$K^* = \left(\frac{1}{L}\int_0^L \frac{1}{K(x)}\, dx\right)^{-1}.$$

By combining the harmonic and the arithmetic means, one can obtain averaging methods which are often seen to give better results than each of them individually. If we denote the arithmetic mean in ξ-direction for

μ_a^ξ, and similarly the harmonic average for μ_h^ξ, then an upscaled diagonal permeability tensor can be formed by combining these averages as follows

$$K_{xx}^* = \mu_a^z(\mu_a^y(\mu_h^x)), \quad K_{yy}^* = \mu_a^z(\mu_a^x(\mu_h^y)), \quad K_{zz}^* = \mu_a^x(\mu_a^y(\mu_h^z)).$$

That is, we first apply the harmonic average in the first dimension, and then the arithmetic average along the two remaining dimensions. This method is known as the *harmonic-arithmetic average*. Similarly, it is also possible to reverse the order to create the *arithmetic-harmonic average*. These two averages are of special interest, because they create outer bounds for the upscaled permeability [60], where e.g., $\mu_h^x(\mu_a^y(\mu_a^z)) \leq K_{xx}^* \leq \mu_a^z(\mu_a^y(\mu_h^x))$.

Flow-Based Upscaling

In local flow-based upscaling the pressure equation

$$\nabla \cdot \left(\frac{\mathbf{K}}{\mu} \nabla p \right) = 0,$$

is solved on each coarse grid block. This is done by applying a pressure drop in each direction in turn, and is illustrated in Figure 4.3. For each direction, the total flux from the pressure solution is used in Darcy's law to find an upscaled value for the permeability. This method is highly dependent on the choice of boundary conditions [38].

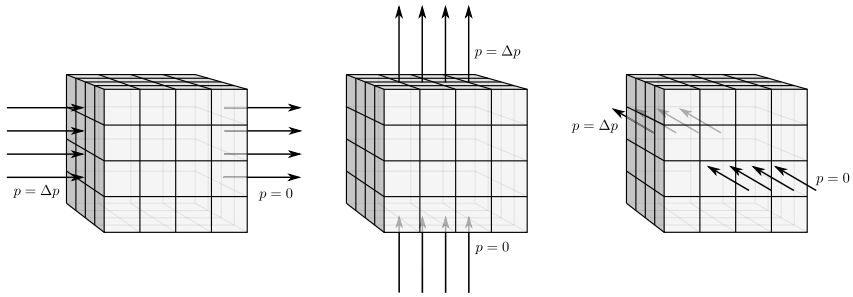

Figure 4.3: Local flow-based pressure upscaling is performed by applying a pressure drop in each direction and solving the pressure equation.

One choice is to apply Dirichlet boundary conditions in one of the directions, and no-flow conditions on the remaining boundaries [12, 11]. Applying a pressure drop Δx across the block in direction ξ, let the resulting total flux per area be v_ξ. Using Darcy's law on the grid block, we obtain

$$v_{\xi,\xi} = -\frac{K_{\xi\xi}^*}{\mu} \frac{\Delta p_\xi}{L_\xi},$$

where L_ξ is a representative length of the grid block in ξ-direction and $K^*_{\xi\xi}$ is the upscaled value of K. Solving for the upscaled permeability gives

$$K^*_{\xi\xi} = -\frac{\mu v_{\xi,\xi} L_\xi}{\Delta p_\xi}.$$

Combining all three dimensions, these upscaled values form a diagonal permeability tensor given by $\mathbf{K}^* = \mathrm{diag}(K^*_{xx}, K^*_{yy}, K^*_{zz})$.

Instead of assuming no-flow conditions on the boundaries perpendicular to flow, one can apply a linear pressure drop on these boundaries. The flow is still induced in one direction by setting constant pressure on two opposing boundaries, but flow is now allowed to cross the remaining boundaries of the block. This means that the resulting upscaled permeability in general becomes a full tensor.

Another possible choice is to apply periodic boundary conditions [24], which also allow for cross-flow. Let us define the two matrices V and P as

$$V = \begin{bmatrix} v_{x,x} & v_{x,y} & v_{x,z} \\ v_{y,x} & v_{y,y} & v_{y,z} \\ v_{z,x} & v_{z,y} & v_{z,z} \end{bmatrix}, \quad P = \begin{bmatrix} \Delta p_x/L_x & & \\ & \Delta p_y/L_y & \\ & & \Delta p_z/L_z \end{bmatrix},$$

where $v_{\xi,\eta}$ is the total flux per area in the ξ-direction caused by a pressure drop in the η-direction. A full upscaled permeability tensor $\mathbf{K}^*$ can then be computed by the matrix equation

$$\mathbf{K}^* = -\mu V P^{-1}.$$

Transmissibility Upscaling

The discretization of the flow equations using the two-point flux approximation (TPFA) was discussed in Section 3.2. In this discretization, the permeabilities are only used to compute the transmissibilities on the interfaces of the grid. Therefore, when upscaling a discrete model, it is quite common to consider upscaling of the transmissibilities instead of the permeabilities [70, 55].

A flow-based transmissibility upscaling has similarities with the flow-based permeability upscaling discussed above. The upscaled transmissibility is chosen such that the flow across an interface of the grid partition is matched between the fine-scale and the coarse-scale.

Consider the flow between two adjacent blocks in the fine-scale grid, which we denote Ω_i and Ω_j. Let the interface between them be denoted Γ_{ij}. The flux between the two blocks is then given by

$$v_{ij} = -\int_{\Gamma_{ij}} (\mathbf{K}\nabla p) \cdot \vec{n}\, dA.$$

On each of the two grid blocks, the upscaled pressures are computed by

$$p_i = \frac{\int_{\Omega_i} p \, dV}{\int_{\Omega_i} dV}, \qquad \text{and,} \qquad p_j = \frac{\int_{\Omega_j} p \, dV}{\int_{\Omega_j} dV}.$$

Now, instead of matching the permeability as in (4.1), we want an upscaled transmissibility T^*_{ij} that fulfills the equation

$$v_{ij} = T^*_{ij}(p_i - p_j). \tag{4.2}$$

Similar to the case of upscaling permeability, this is not possible to obtain in general for any pressure field. However, given a particular pressure field, the equation (4.2) now determines T^*_{ij} uniquely.

4.3 Two-Phase Upscaling

When creating a coarse scale model for two-phase flow, the relative permeability curves, and possibly also capillary pressure, needs to be upscaled in addition to the porosity and absolute permeability, which were discussed in the previous section. Upscaling of relative permeability has also been studied quite extensively, though maybe not to the extent of one-phase flow. Papers giving reviews and interesting discussions on two-phase upscaling include [7, 18, 23, 14, 26].

Dynamic methods (*pseudoization methods*) are two-phase upscaling techniques that compute a flow solution on the fine scale, and compute pseudorelative permeabilities based on this solution. Overviews of dynamic methods can be found in [7, 6], and a comparison study is performed in [23]. One type of dynamic methods are the *Kyte and Berry methods*, which were first introduced in [39], use the fine-scale solution to create an average pressure in each coarse grid block. These pressures are used to find upscaled relative permeability values which reproduce the flow from the fine-scale solution. These methods have some clear weaknesses, as they may produce negative or infinite values for the relative permeability [7]. To avoid some of the problems of the Kyte and Berry method associated with the average coarse pressures, *Stone's method* [63] instead computes upscaled relative permeabilities from the average fractional flow and the average total mobility. However, the method cannot be used with gravity or capillary pressure [7]. Different improvements to Stone's method have been suggested, which use better definitions of the average total mobility. One example is the method suggested in [21], but also this method may produce negative values [6].

Steady-state methods make up another group of two-phase upscaling methods, which we consider in several of the papers included in this thesis. The basic assumption of the steady-state methods is that the saturation change within each block is very small relative to the average flow rate of the fluids, such that the saturation can be said to be constant. A relatively early work on steady-state methods is that of [62], and further discussions of steady-state methods can be found in e.g., [38, 57]. Later work has mostly focused on the application of steady-state methods, and their validity for different models and flow rates [58, 59, 28], and this also includes some more recent publications [42, 47, 34, 54]. In the following section, we will discuss the details of steady-state methods and how the upscaled relative permeabilities are computed.

Steady-State Upscaling

At steady-state, there is no time-dependence in the saturations. If we discard compressibility and gravity, and assume we are away from any well, the phase equation (2.3) for phase α becomes

$$\nabla \cdot \left(-\frac{k_{r\alpha}\mathbf{K}}{\mu_\alpha} \nabla p_\alpha \right) = 0. \tag{4.3}$$

Because the saturations do not change, the relative permeability $k_{r\alpha}(s_w)$ is also constant. Thus, by assuming the saturation distribution s_w is known, then (4.3) is equal to the one-phase pressure equation, where the permeability now instead is given by the product $k_{r\alpha}\mathbf{K}$. This means we can apply a one-phase upscaling method to upscale the phase permeability $k_{r\alpha}\mathbf{K}$, and we denote the upscaled value for $(k_{r\alpha}\mathbf{K})^*$. The upscaled relative permeability is then found by dividing by the upscaled absolute permeability, and we get

$$k^*_{r\alpha}(s^*_\alpha) = (k_{r\alpha}\mathbf{K})^*(\mathbf{K}^*)^{-1}.$$

When applying the one-phase upscaling method, we can do this in each of the three dimensions, giving an upscaled relative permeability diagonal tensor

$$k^*_{r\alpha} = \mathrm{diag}(k^*_{r\alpha,xx}, k^*_{r\alpha,yy}, k^*_{r\alpha,zz}).$$

The upscaled value of the relative permeability will depend on the saturation distribution in the steady-state solution, and so $k^*_{r\alpha}$ will be a function of an upscaled water saturation s^*_α. This saturation is given as the pore-volume average over the grid block, such that

$$s^*_\alpha = \frac{\int_\Omega \phi s_\alpha \, dx}{\int_\Omega \phi \, dx}. \tag{4.4}$$

In order to create full upscaled relative permeability curves, we have to find a series of steady-state distributions, and for each state, compute upscaled values $k^*_{r\alpha}$ with corresponding upscaled saturations s^*_w. This method of looping over saturation values is described in [61].

Finding a Steady State

As we need the steady-state saturation distribution to compute the upscaling of the relative permeabilities, the main problem is then to find this distribution. One way to do this, is to perform a flow simulations on the grid block using some set of boundary conditions (often periodic boundaries are used). Given an initial saturation, a simulation is run until the saturation change in the block is below some threshold. However, the final saturation will depend on the initial condition and on the particular boundary conditions, so this method does not uniquely define upscaled curves. Also, this is obviously a computationally expensive method, as a flow simulation has to be run for each point on the upscaled curves. Using a good initial guess for the distribution and clever time-step control can reduce the cost somewhat.

By making further assumptions, there are faster ways to obtain a steady-state distribution. The two most common assumptions are the capillary-limit and the viscous-limit methods [38, 59]. In the capillary-limit method, it is assumed that the flow rate is slow enough, such that the capillary forces have time to redistribute the fluids and obtain a capillary equilibrium. Thus, the capillary pressure is assumed to be constant within the grid block. If this constant value is $\hat{p}_{\text{cow}}$, then the saturation distribution is found by inverting the capillary pressure, such that $s_w = p^{-1}_{\text{cow}}(\hat{p}_{\text{cow}})$.

In the viscous-limit method, the flow rate is assumed to be large enough such that the capillary forces are negligible. At steady-state, the fractional flow f_w, as defined in (3.7), then becomes constant along streamlines, and will only depend on the choice of inlet boundary conditions [28]. A common assumption is constant fractional flow over the inlet, resulting in constant fractional flow in the whole block. Denoting this constant value by $\hat{f}_w$, the saturation distribution that $s_w = f^{-1}_w(\hat{f}_w)$.

Capillary Pressure Upscaling

As discussed in Section 2.2, the capillary pressure is dependent on the saturation and on the particular rock type. In a two-phase oil-water reservoir model, the capillary pressure is therefore in general given by a function $p_{\text{cow}}(x, s_w)$, which depends on both the position x and the water saturation s_w. A common assumption when upscaling, it to assume that the capillary

pressure is always equal everywhere inside the grid block Ω. Based on this assumption, the upscaled capillary pressure function $p^*_{\text{cow}}(s^*_w)$ is computed as follows. Let the capillary pressure be constant within Ω, such that

$$p_{\text{cow}}(x, s_w) = \hat{p}_{\text{cow}},$$

for some value $\hat{p}_{\text{cow}}$. Then, find the saturation distribution s_w which fulfills this equation by inverting the capillary pressure function in the saturation variable. That is, compute

$$s_w(x) = p^{-1}_{\text{cow}}(x, \hat{p}_{\text{cow}}).$$

The upscaled value of the saturation s^*_w is taken as the pore-volume average over the grid block (4.4), and the upscaled capillary pressure is then given by $p^*_{\text{cow}}(s^*_w) = \hat{p}_{\text{cow}}$. Similar to the upscaling of relative permeability, this upscaling needs to be repeated for a series of different values $\hat{p}_{\text{cow}}$ in order to create a full upscaled capillary pressure function.

In this presentation, we have neglected any gravitational forces in the upscaling. However, if gravity plays an important role in the force balance of the particular scenario considered, then it should be accounted for in the upscaling of capillary pressure. This is further discussed in Paper I.

4.4 Compositional and EOR Upscaling

Multi-component and compositional models are needed to run enhanced oil recovery (EOR) scenarios, and such simulations can be very computationally demanding. If in addition a large number of flow simulations are needed, for example for optimization of the EOR strategy, then upscaling of the model may be required. Methods for upscaling flow where multiple components are present have not been studied to the same extent as one- and two-phase parameters, but there are several examples of publications on the topic.

A method for upscaling compositional flow was suggested in [8], where transport coefficients (α-factors) for the components were computed from fine-scale simulations. These coefficients relates the coarse scale compositional flow to the average compositions within the block in a similar fashion as upscaled relative permeability curves relate the phase fluxes to the average saturations. This method was also considered in [20] and other works, but only for single-phase flow.

Examples of more recent work include a method for upscaling of two-phase multicompontent flow suggested in [32], which includes thermodynamic equations, and accounts for compressibility in the upscaled flow functions. Another recent approach for two-phase compositional upscaling was

presented in [44], where near-well behavior is also accounted for in the upscaling.

Upscaling of EOR methods has also recently been studied in [5], which uses an upscaling-downscaling method to achieve higher accuracy, and in [2], where the adsorption function in polymer flooding is upscaled.

We do not further discuss any details of upscaling compositional flow or EOR in the background part of this thesis, but our work in Paper III considers an approach for upscaling of two-phase polymer flooding.

4.5 Multiscale Methods

The fine-scale details of a model can have a large impact on the global flow-patterns, and in an upscaled coarse model, a lot of this detailed information will necessarily be lost. This makes upscaling methods difficult to apply in general, and the errors introduced are hard to estimate and control.

Different types of *multiscale methods* [33, 17, 52, 49] offer an alternative to upscaling. These methods have similarities with upscaling as the pressure equation is solved on the coarse scale, but as opposed to upscaling methods, a multiscale model includes the original heterogeneities, and can adapt the coarse solution to the fine-scale grid. There are a number of different multiscale methods, but most of them build on the same ideas. From the original fine-scale problem, an equivalent flow-problem on the coarse-scale is created by using a set of basis functions. These basis functions are constructed by solving localized flow-problems defined over coarse blocks on the fine-scale grid, which is similar to the method of flow-based upscaling. The coarse problem is then solved to get a solution which accounts for the global effects of the model. An important feature of the multiscale methods is that once the coarse-scale pressures/fluxes are known, fine-scale velocity (and pressure) fields can be reconstructed. Depending on the method, this can be done either by the use of basis functions, or by solving local flow problems on the fine-scale grid.

Two types of multiscale methods that have been in focus over the past decade [49], are the multiscale finite-volume (MsFV) methods [33] and the multiscale mixed finite element (MsMFE) methods [17]. These two methods have different strengths and weaknesses. In short terms, the finite-volume methods have been extended to handle realistic flow physics, but have been difficult to apply to complex grid structures. In contrast, the mixed finite element methods are able to handle grids of large complexity, but are challenging to use with advanced flow models. More recently, the multiscale two-point flux approximation (MsTPFA) method [52] was proposed

to combine the best features of the two methods, showing both robustness and flexibility. Shortly after, the multiscale restricted smoothed basis (MsRSB) method [49, 50, 51] was also proposed, which is simpler than the MsTPFA, but more accurate, flexible and robust.

In this thesis, we consider the application the MsRSB method on polymer flooding simulations in Paper IV. As polymer simulations contain large mobility contrasts, and often require short time-steps to converge, efficiency of the simulator is essential. Our examples in Paper IV show promising results and further demonstrates the flexibility of the MsRSB method.

Chapter 5

Summary of Papers

The research papers are included in Part II of this theses. In this chapter, we summarize the papers and discuss how they are connected. We also give comments and ideas for further work. The papers are not included in chronological order based on when they are written, but are ordered based on content, which we find natural in our case. Papers I though III are all related to upscaling, and papers III through V are concerned with polymer flooding. Note that Paper III combine both these topics.

Papers I and II are both related to upscaling of two-phase flow of oil and water. Paper I considers in detail the balance of forces during the water flooding of a reservoir by considering simulation results and uses this to quantify when viscous-limit and capillary-limit upscaling methods may be applicable. Paper II compares different one- and two-phase upscaling methods on realistic field-scale models, and we also suggest two novel steady-state methods based on the results from Paper I. Paper III discusses upscaling when polymer is included into two-phase flow, and extends established upscaling methods from two-phase to also include polymer properties. Paper IV applies a multiscale method to solve the polymer flow problem efficiently, and demonstrates this on complex grids using highly non-linear fluid physics. Finally, Paper V considers the modeling of velocity enhancement due to inaccessible pore volume, which is an import physical effect of polymer flooding. The conventional method for modeling this effect can lead to ill-posed equations and we propose alternative models which are seen to produce well-behaving results, which can contribute to improved convergence and hence more efficient simulations.

Paper I

Rate Dependent Force Balance and Upscaling of Unsteady Flooding Processes

Sindre Tonning Hilden and Carl Fredrik Berg

Submitted

For a general steady-state upscaling, it is necessary to run a simulation in order to find the saturation distribution in the grid block, which is a computationally expensive task. However, by making further assumptions about the force balance, the distribution can be computed without any simulations, which greatly reduces the cost of the upscaling. The low-rate capillary-limit upscaling assumes that the capillary and/or gravity forces are dominant, while the high-rate viscous-limit upscaling assumes on the other hand that these forces can be neglected. To apply one of the steady-state limit methods, it is important to understand when the limiting assumptions are valid, and thus for what cases the upscaling can be used. This is the main motivation for this paper.

As discussed earlier in the background part, there exists a large amount of literature on the subject of two-phase steady-state upscaling [62, 59, 58, 18, 42, 34], and in particular on the steady-state limit upscaling methods [28, 47, 54, 67]. However, this is a complex topic, and there is no definite answer as to when an upscaling method is applicable. This paper takes a practical approach and investigates the balance of forces by numerical two-phase simulations on various fine-scale models for a wide range of flow rates. Then, we perform upscaling and run the same simulations on coarse-scale grids. In light of the fine-scale simulation results, we discuss the validity of the steady-state limit methods.

To run a simulation for very low flow-rates, where capillary and gravitational forces dominate, can be computationally demanding. We present a semi-analytical method which allows us to efficiently compute this low-rate solution for a flooding process. To our knowledge, this method is novel. The high-rate limit solution is easily obtained by neglecting capillary pressure and gravity in the numerical simulation. Thus, we can compute both outer limits, which is useful when considering solutions for intermediate flow rates.

We first consider fine-scale simulations of water-flooding for both simplified and more realistic field-scale models. As an example taken from the paper, the left plot in Figure 5.1 shows the total oil production for a homogeneous model for different flow velocities, where also the limit solutions are

shown. We observe how the rate-dependent simulation results move from the capillary-limit to the viscous-limit solution. To better visualize this rate-transition, we plot the solutions at the point where 0.8 pore-volumes of water has been injected into the model. These solutions are shown as curves in the right plot of Figure 5.1 for three different model lengths. The solutions can clearly be seen to converge to both limits and the transition between them is smooth. This is seen for all models we consider. However, depending of the model properties, the solutions are not necessarily bounded by the low- and high-rate limits and the transitions can be non-monotone.

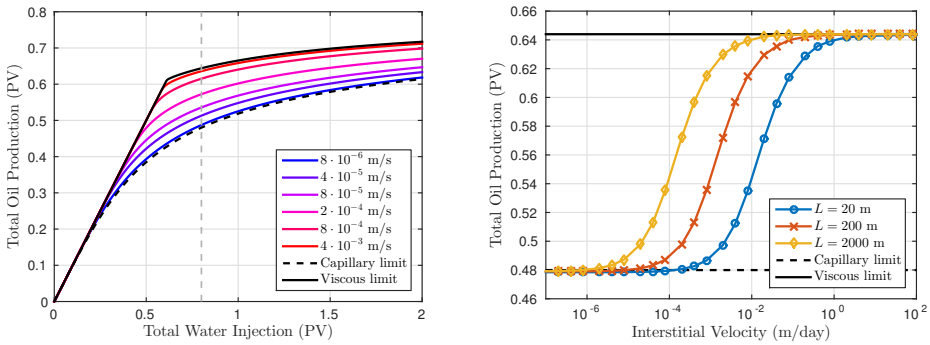

Figure 5.1: Total oil production for a homogenous 1D model from Paper I. Left: Total production for different interstitial velocities for model of length 2000 m. Right: The total production after 0.8 pore-volumes of water has been injected (at vertical dotted line in left plot) for models of different lengths.

For realistic flow-rates, viscous forces are seen to dominate the distribution of fluids in the flow direction. However, capillary and gravitational forces typically dominate the distribution normal to the flow. This directionally dependent force balance occurs because the length of the heterogeneities in vertical direction are typically much smaller than in the horizontal direction due to the very nature of sedimentary rock formations.

The paper continues by performing upscaling of the models, run the corresponding coarse-scale simulations, and then compare them to the fine-scale results. For all cases we consider, the capillary-limit upscaled models are able to reproduce the low-rate limit solution, as well as the transition from this limit and up to the point where capillary and gravitational forces no longer dominate the distribution of fluids normal to the flow direction. That is, the capillary-limit upscaling is valid outside of the low-rate limit solution. Also, the method is able to incorporate some of the gravitational effects, and we observe that it is important to including gravity in the

upscaling procedure.

Coarse models created by the viscous-limit upscaling are in general not able to reproduce the high-rate limit. The viscous-limit upscaling is only valid if the fractional flow is close to constant within each grid block, away from the water-front. For any upscaling method, the choice of coarse grid is important for the success of the upscaling. If a coarse grid is chosen to resolve the heterogeneities of a reservoir model, then also the viscous-limit method may be applicable.

Comments

This paper confirmed that the force balance during a water flooding often can be directionally dependent. We found this result very interesting, and it motivated us to investigate this force balance further. If the directional dependence is also present in realistic reservoirs, then it should be reflected in the upscaling procedure. This reasoning lead us to develop two novel steady-state methods, which compute the upscaling in two stages; a first stage where capillary equilibrium is assumed in the vertical direction, and a second stage assuming viscous equilibrium in the horizontal direction. These methods are presented as part of our Paper II.

Paper II

Comparison of Two-Phase Upscaling Methods on Field Models

Sindre Tonning Hilden and Carl Fredrik Berg

Submitted

The study of upscaling methods on simplified models is important to understand details of the methods and to highlight certain aspects. However, it is difficult to draw general conclusions, and to understand how well the methods work on more realistic models based on the simplified results. This paper compares different one-phase, and in particular, two-phase methods on realistic field-scale models. To assess how well the different methods perform, we run two-phase flooding simulations both on the original fine-scale and the upscaled coarse model, and compared the results.

As already noted as comments to Paper I, we propose two different steady-state upscaling methods which combine ideas from the capillary-limit and the viscous-limit upscaling. Both these methods compute the upscaling in two stages, where we first assume the forces to be in capillary equilibrium in vertical direction, and subsequently assume viscous equilibrium in the horizontal direction. The two methods are constructed slightly different, and our hope is that they are able to capture some of the directionally dependent force balance. Because of how they are constructed, we refer to these techniques as two-stage methods. Different upscaling methods are compared using numerical examples, and in these comparisons, we also include the two suggested methods.

We first run simulations on a simplified layered model, and then on two different realistic field-scale models. For the single phase upscaling we apply flow-based pressure upscaling, harmonic-arithmetic and arithmetic-harmonic mean, as well as a global transmissibility upscaling. For the two-phase upscaling, we consider both steady-state methods and simpler averaging techniques. To be able to quantify the error in the coarse scale simulations, we define an error norm, which measures the relative difference in well results (such as e.g., oil production rate) between the coarse-scale simulation and the corresponding fine-scale simulation, which is considered the true solution in this context. As an example, two error plots for the second realistic model of the paper is shown in Figure 5.2.

Considering the simulation results for all the models, we observe that in the case where the original fine-scale model only has a single pair of relative permeability curves, the choice of one-phase upscaling method has a larger impact on the solution than the two-phase method. On the other

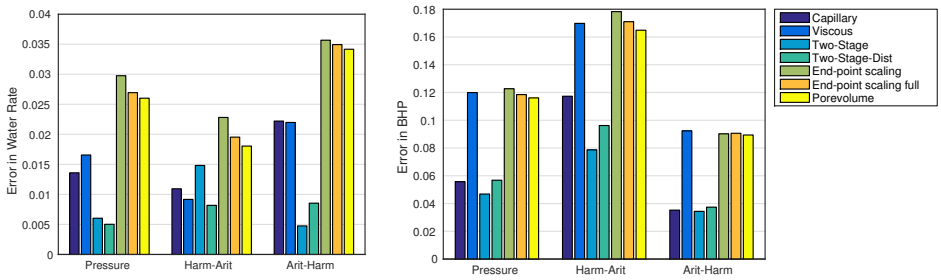

Figure 5.2: Error in well solution for the fluvial model in Paper II. The labels on the x-axis denote the one-phase upscaling method used, while the different colors denote the two-phase method and is explained in the legend.

hand, if the relative permeability varies in the original model, then the capillary-limit upscaling and the two novel methods give better results than the viscous-limit upscaling and simpler averaging techniques, which is also observed in Figure 5.2.

For typical reservoir rates, both the two-stage methods and the capillary-limit upscaling give good agreement with the fine-scale solution. In some cases, one can even argue that the two suggested methods give a slight improvement over the capillary-limit method. However, as the flow-rates are decreased, the capillary-limit solution changed in a similar fashion as the fine-scale solution. Because both the new methods include an assumption of viscous-equilibrium as part of the upscaling, their coarse models do not contain any capillary pressure, and so these methods do not capture the change of rates in the same fashion. At the same time, the rate-dependency of the capillary-limit method is not very accurate, and the match with the fine-scale solution is seen to be increasingly worse as the flow-rate is reduced further.

Comments

The results from this paper shows the complexity of upscaling in practice and how the best upscaling method is truly case-dependent, which was discussed in the introduction to this thesis. Our suggested two-stage methods do not offer an upscaling which is always better than other methods, but they offer an alternative, which can be considered when assessing a particular upscaling problem.

Paper III

Steady-State Upscaling of Polymer Flooding

Sindre Tonning Hilden, Knut-Andreas Lie, and Xavier Raynaud

ECMOR XIV - 14th European Conference on the Mathematics of Oil Recovery, Catania, Sicily, Italy, 8-11 September 2014

This article extends the ideas from two-phase upscaling to also include polymer properties in the upscaling procedure. The polymer equations studied are the two-phase oil-water equations including polymer (2.5), which are discussed above in Section 2.3.

By considering the equations at steady-state, when there is no time-dependency, and further assuming that there are no sealing faces in the grid block that is to be upscaled, we show that the polymer concentration is in fact constant within the block. This is relatively simple to show, but has important implications for the upscaling procedure. It means that for any average concentration, the steady-state distribution of polymer within the block is known, and there is no need for a full flow-simulation. Otherwise, a simulation would have to be run for each combination of water saturation and polymer concentration, which would amount to a significant computational cost.

The constant polymer concentration at steady-state has further implications. Considering the definition of the effective viscosities, we find that they now can be written as

$$\mu_{p,\text{eff}} = \alpha\mu_w, \qquad \text{and} \qquad \mu_{w,\text{eff}} = \beta\mu_w,$$

where both α and β are constants, meaning that both are proportional to the pure water viscosity. Inserting this into the conservation equations, the water and polymer equations reduce to the same equation, and we are left with

$$\nabla \cdot \left(\frac{k_{ro}}{B_o\mu_o} \mathbf{K}\big(\nabla p_o - \rho_o g \nabla z\big) \right) = 0, \tag{5.1a}$$

$$\nabla \cdot \left(\frac{\widetilde{k}_{rw}}{B_w\mu_w} \mathbf{K}\big(\nabla p_w - \rho_w g \nabla z\big) \right) = 0, \tag{5.1b}$$

where the altered water relative permeability is $\widetilde{k}_{rw} = k_{rw}/R_k$, and the reduction factor R_k is given by the definition (2.7).

Equations (5.1) are equal to the conservation equations for a pure oil-water system, except that the water relative permeability now is scaled

by the reduction factor. This means that to upscale (5.1), any steady-state relative-permeability upscaling procedure can be applied. Because the effective viscosities are proportional to the pure water viscosity and are constant for any choice of concentration, they are not natural candidates for upscaling. However, the reduction factor R_k both appears in the modified relative permeability $\widetilde{k}_{rw}$, and as it depends on adsorption, it may vary in space, even for constant concentration. The suggested upscaling method is therefore to upscale $\widetilde{k}_{rw}$ in (5.1b) using some relative permeability method to obtain an effective value $\widetilde{k}^*_{rw}$. Then, we find an upscaled value of the reduction factor by

$$R^*_k(s^*_w, c^*_p) = \frac{k^*_{rw}(s^*_w)}{\widetilde{k}^*_{rw}(s^*_w, c^*_p)}. \tag{5.2}$$

The upscaled value of the reduction factor will depend both on the water saturation and polymer concentration. The upscaling of R_k is run on two different models to validate our methodology. Both examples show that the upscaled values may also in practice depend on the water saturation. An example is shown in Figure 5.3, where the upscaling of a simple layered model clearly shows a saturation dependency in z-direction, when the flow is normal to the layers. This saturation dependence is not really desirable, as the amount of upscaled data potentially could be relatively large for a big model. Also, if the upscaled data is used in a coarse-scale simulation, there is a need to perform a two-dimensional table lookup and interpolation for every evaluation of R_k. To reduce the complexity, one could consider fitting the upscaled data to a (possibly nonlinear) parametric model.

To further evaluate our methodology and to also assess the errors introduced by upscaling, a third numerical example is performed where we consider a simplified 2D cross-section model. In this example, a simulation is run both using the original model and the upscaled coarse model, and the results are then compared. The most evident conclusion from these simulations is that the error introduced by the grid coarsening is much larger than the upscaling error. In our example, the choice of upscaling method is almost irrelevant in terms of coarse-scale error, compared to the choice of grid coarsening. This will however strongly depend on the scale of the model and the particular flow case considered.

Comments

In the last example in the paper, it is interesting to note that the match between the fine- and coarse-scale solutions is much better when using a mixing parameter of $\omega = 0.8$ instead of using $\omega = 1$. This is because when

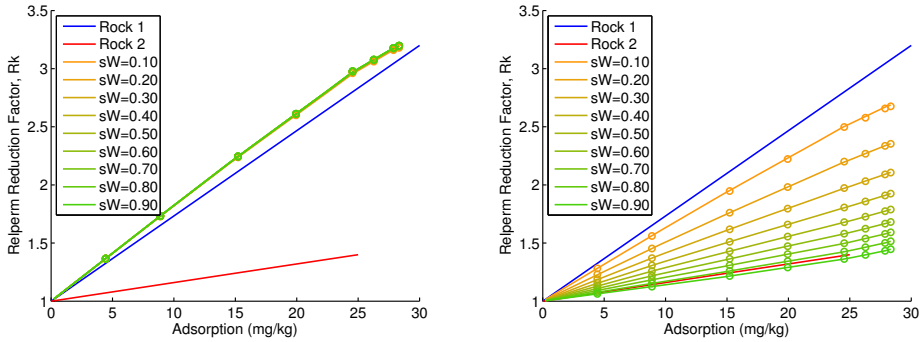

(a) x/y-direction (b) z-direction

Figure 5.3: Upscaled relative-permeability reduction factor R_k for a simple layered model, taken from Paper III. The fine-scale curves are shown in blue and red, and the yellow-to-green lines are upscaled curves.

$\omega = 1$, the polymer flux function is linear, and there is no self-sharpening effect, which there typical is for a pure water-front. However, if $\omega < 1$, then the polymer front will also be self-sharpening, reducing the smearing effect of the grid coarsening. As ω is lowered, the self-sharpening grows stronger.

This effect where reduction of the mixing parameter increases the self-sharpening is something we considered further. To counteract some of the smearing introduced by grid coarsening, it could be possible to reduce ω in the upscaled model. We performed some simple tests to see this in practice, and the resulting concentration from a simple 1D simulation is shown in Figure 5.4, where polymer is injected over the west boundary. The fine-scale simulation is run using $\omega = 1$, and the coarse-scale solution is using three different values. Running the simulation with $\omega = 1$ on the coarse scale, we observe how the polymer front is smeared out. However, lowering ω counteracts the coarsening effect, and for $\omega = 0.88$, the coarse-scale solution is almost identical to the fine-scale solution.

Unfortunately, this way of adjusting the mixing parameter is difficult to do in a general and robust manner. In our example, the fine-scale solution is known and the adjustment of ω is done manually. In a general scenario, one should somehow predict the amount of diffusion the coarsening introduces, as well as estimate a priori the value of ω in the coarse model. These are obstacles we did not see any good solution for, and therefore, we ended up not pursuing this idea further.

We finally note that upscaling of polymer properties has also later been discussed in [2], where a dynamic method is applied to create effective ad-

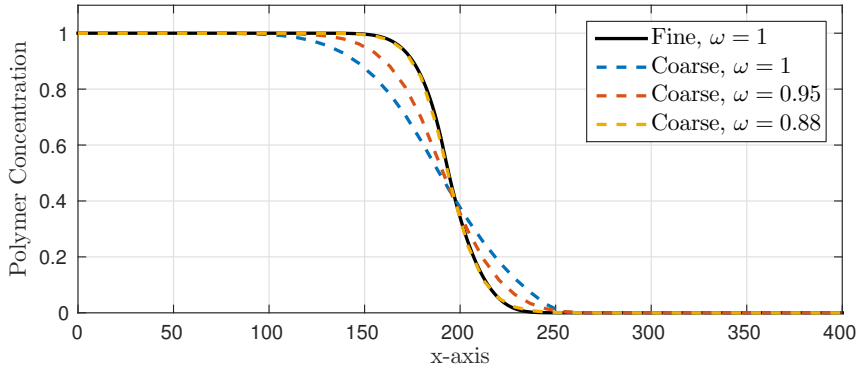

Figure 5.4: Polymer injection in a 1D domain, both on a fine-scale with 400 cells and on a coarse-scale grid with 50 cells. Different values for the mixing parameter ω are used.

sorption curves on simplified models. Dynamic upscaling requires flow-simulations on the fine-scale grid, which is computationally more expensive, but can possibly better approximate a particular flow-scenario, if this is known a priori.

Paper IV

Multiscale Simulation of Polymer Flooding with Shear Effects

Sindre Tonning Hilden, Olav Møyner, Knut-Andreas Lie, and Kai Bao

Submitted

Multiscale methods can be used to significantly reduce the computational time of reservoir simulation. This also enables simulations of more detailed models, which may reduce the need for upscaling. Simulations involving polymer flooding can be particularly numerically challenging due to large mobility contrasts, highly non-linear fluid properties and strong coupling between the primary variables. In addition, smaller time-steps may be required to maintain a relatively sharp displacement, as a fully mixed polymer solution front is not self-sharpening. All this makes the application of a multiscale solver to polymer simulations particularly interesting, and is what we consider in this paper.

A sequential formulation of the two-phase polymer equations is first presented, where also the effect of shear-thinning is included. This formulation has to our best knowledge not been described in the literature previously. The shear-thinning adds to the non-linearity of the equations, and needs to be handled properly in the solution scheme. When solving the sequential system, the pressure equation is solved approximately by a multiscale solver instead of using a fine-scale direct solver. The multiscale solver which we consider in this paper is the multiscale restricted smoothed bases method (MsRSB) [49, 50], where the restriction operator is constructed by an iterative scheme. This method has proved to be robust and able to handle both complex geometry and fluid physics. This paper does not deal with the details of the MsRSB method, but considers its application to the case of two-phase oil-water simulations including polymer, which is an extension to a more nonlinear problem than what has previously been studied in the literature.

The multiscale solver is also flexible in terms of tolerance levels, allowing control of the trade-off between accuracy and computational cost. The pressure can be approximated by a single multiscale solution, which by itself would give similar accuracy as an upscaling method. Alternatively, the pressure can be computed iteratively by several multiscale solutions, and as the tolerance level is lowered, this solution approaches a fine-scale pressure solution. An essential feature of the multiscale method is that regardless of the chosen accuracy, the fine-scale pressure solution will always be mass-conservative.

We perform different numerical experiments in the paper, both to illustrate the correctness of our formulation and implementation, and also to demonstrate the robustness and efficiency of the solutions scheme. Our formulation of the polymer equations are the same as in the commercially available simulator Eclipse 100 [27], and so we compare our results with simulations run in Eclipse as a verification example. The difference between the solutions is quite small, considering Eclipse uses a fully-implicit scheme, and the multiscale solver is based on a sequential scheme. But, because of the non-linearities of the problem, both simulators are forced to take small time-steps, and thus reducing the difference between the schemes.

To further demonstrate that our method is able to handle complex grid structures, we run an example on the SAIGUP model, which is shown in Figure 5.5. In this case, we compare the sequential solver using approximate multiscale pressures with a sequential formulation using a direct fine-scale pressure solver. This comparison for the oil production is also shown in Figure 5.5, where we observe that the solvers produces almost identical results. Timing results from this example also show that the multiscale method greatly reduces the cost of computing the pressure equation. For the fine-scale sequential solver, the pressure solution is the major contribution to the overall run-time.

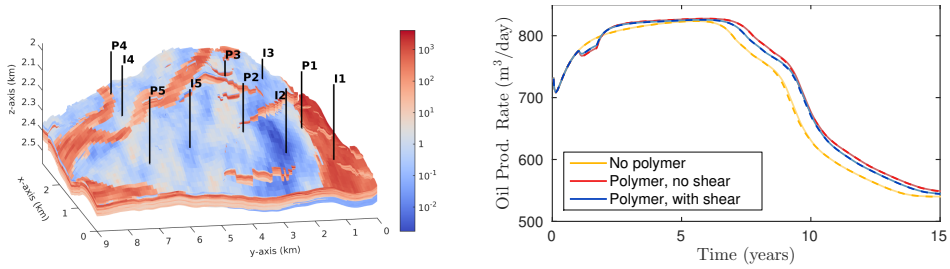

Figure 5.5: The SAIGUP example from Paper IV. Left plot show the permeability field of the model including the wells. Right plot show the oil production rates for producer P1. The reference solutions are plotted as solid lines, while the MsRSB solutions with a single multiscale cycle are plotted as dashed lines on top using slightly stronger colors.

Finally, a third example is also run on a model containing sealing faults and adaptive gridding. In this example, we also demonstrate that the multiscale solver converges to the fully-implicit solution by imposing an outer nonlinear-tolerance on each time-step. This further increases the flexibility of the multiscale method.

All the numerical examples performed in the paper show that the MsRSB

method can be applied to two-phase simulations with polymer, and that the solver is able to obtain highly accurate results at the same time as the computational cost is significantly reduced. The method is also able to handle complex geometry and a large set of different polymer effects, and in particular the shear-thinning effect.

Comments

The multiscale solver with polymer has shown to be both accurate and robust. For some of the cases run on the Upper Ness formation of the SPE 10 model, our multiscale solver was even seen to be more robust than the Eclipse fully-implicit simulator. To be able to significantly reduce the computational time of the simulations without sacrificing the details of the solution is highly beneficial. It would therefore be very interesting to extend the use of the MsRSB solver to other EOR-methods, such as e.g., surfactants, which lower the interfacial tension between fluids, alkaline-surfactant-polymer (ASP) flooding, which combines three chemical methods, or microbial enhanced oil recovery (MEOR), using microorganisms to increase recovery. Also, polymers are highly sensitive to salinity, so it would both useful and interesting to include salinity effects into the existing polymer solver. The MsRSB solver has shown to be able to handle complex fluid models robustly, and the different EOR-methods mentioned are modeled using similar equations as polymer flooding. Including other EOR-methods will not introduce any conceptual challenges, and such extensions should therefore be doable.

Paper V

A Well-Posed Model of Inaccessible Pore Volume for Polymer

Sindre Tonning Hilden, Halvor Møll Nilsen, and Xavier Raynaud

Submitted

When polymer is added to the injected water, there are a number of different physical effects which have an impact on the flow, and which need to be included into the modeling equations to simulate flooding scenarios as accurately as possible. Several of these effects are discussed in Section 2.3.

This paper considers in detail the modeling of inaccessible pore volume (IPV), which is one of the important physical effects. Due to the relatively large size of the polymer molecules, they are unable to enter the smallest pores of the rock, resulting in an accelerated flow relative to the water. The most common model for the IPV can for certain problems lead to un-physical solutions, where the polymer is allowed to travel through a water shock front, and into regions without water. This shortcoming of the conventional model has been shown earlier [9], and we also demonstrate it in this article through an analytical 1D example. An alternative IPV model was also suggested in [9], which was derived based on percolation concepts, but this model has the limitation that it assumes the inaccessible pore volume is smaller than the irreducible water saturation. Both the shortcoming in the convectional model, and also the limitation in the alternative model from [9], motivated us to look for another model that leads to well-posed equations and does not put restrictions on the problem parameters.

By considering shock-solutions in one dimension, we first derive a necessary condition, that any IPV model must fulfill in order for the equations to be well-posed. This condition is a useful tool when considering possible IPV models. Then, based on a simple heuristic physical understanding of flow in a porous media, we construct alternative IPV models. The first model we derive assumes a uniform polymer distribution, but does not fulfill our condition for well-posedness. As a modification, we assume a non-uniform polymer diffusion and slightly relax the IPV-assumption. That is, we assume that polymer may enter all pores, but that access to the smallest pores are limited. This non-uniform model fulfills the necessary condition for all relative permeabilities.

The different IPV models are then applied to numerical examples and we consider how they behave in practice. All models, except for the non-uniform model, show sharp peaks in the polymer solution near the water front for one or more of the examples. In several cases, these peaks seem

to grow uncontrolled, and could be a clear indication of potential problems. The solution of one of the examples from the paper is shown in Figure 5.6, where water and polymer is injected over the west boundary. The conventional IPV model is compared to the percolation based model from [9] and our two suggested modifications. This figure clearly shows the undesired behavior of most of the models, where the polymer solution seems to grow uncontrolled at the front. Only our suggested non-uniform model produces a well-behaved solution in this case.

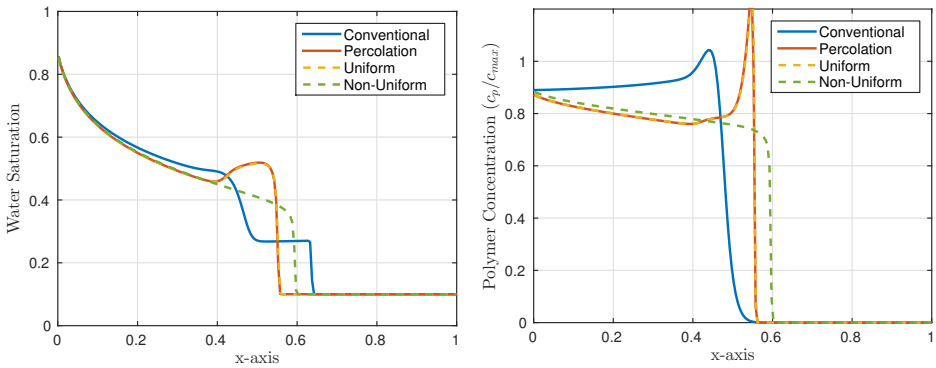

Figure 5.6: Solution of one example from Paper V, showing the difference between the various IPV models considered.

The non-uniform model produces well-behaving solutions in all the examples we consider and the polymer concentration is also always seen to be below the maximum value. We note that it is not mathematically guaranteed that the concentration always will be below maximum value, but we have not been able to construct an example where this happens. Thus, as the concentration in practice is limited to a priori known values, one can limit the solution space in a Newton solver, and in this way possibly improve convergence.

The alternative IPV model we suggest in this paper is simple to implement into an existing simulator, which was an important criterion for us, as this makes it a practical alternative to the conventional model.

Chapter 6

Future Work

There are several directions in which this work can be continued. Some possible topics for future work are given below.

- The upscaling of two-phase flow is considered in papers Paper I and Paper II. This work can be continued in a number of ways.
  - As the realistic field models we have worked with are mostly fluvial, models of other depositional environments may be considered, as the effects of upscaling may be different.
  - The considerations of force balance could be extended to include gas in simulations, and subsequently consider upscaling of gas relative permeability.
  - Upscaling of polymers have been considered to some extent in Paper III, but the upscaling of other EOR techniques could be investigated, such as e.g., alkaline, surfactants, or foam.
  - Relative permeability curves can be computed using dynamic pseudoization, which fits the upscaled curves to fine-scale simulation results. Such pseudo curves could be compared to other upscaling methods, and in particular the steady-state methods, to observe the difference in coarse-scale results. See also discussion in [7].
- While upscaling of polymer in two-phase flow is studied in Paper III, it is still not clear how well this upscaling performs on field models, and what upscaling method produces the best match with fine-scale solutions. How to best include polymer effects in coarser models is a subject that can be investigated further, and a comparison study similar to Paper II could be a possibility. Such a study could also consider

fitting of the upscaled data to a (possibly nonlinear) parametric model, and different dynamic upscaling methods can be applied, in addition to steady-state methods as we have discussed.

- The polymer model used in this thesis, and in particular in Paper IV, includes several polymer properties, but there are still many effects not included which have an impact to the flow. The polymer model could be extended to include more polymer physics, such as e.g., hydrolysis, multi-component polymers, and salinity effects.
- As already discussed in the comments to Paper IV (see page 42), the MsRSB method could be applied to other enhanced oil recovery methods, such as e.g., surfactants, ASP flooding or microbes.

Bibliography

[1] J. E. Aarnes et al. "Modelling of Multiscale Structures in Flow Simulations for Petroleum Reservoirs". English. In: *Geometric Modelling, Numerical Simulation, and Optimization*. Ed. by G. Hasle, K.-A. Lie, and E. Quak. Springer Berlin Heidelberg, 2007, pp. 307–360.

[2] A. Aldhuwaihi, P. King, and A. Muggeridge. "Upscaling Polymer Flooding to Model Sub-gridblock Geological Heterogeneity and Compensate for Numerical Dispersion". In: *IOR 2015 – 18th European Symposium on Improved Oil Recovery Dresden, Germany, 14-16 April 2015*. 2015.

[3] K. Aziz and A. Settari. *Petroleum reservoir simulation*. Applied Science Publishers, 1979.

[4] M. Babaei and P. R. King. "A Modified Nested-Gridding for Upscaling–Downscaling in Reservoir Simulation". In: *Transport Porous Med.* 93.3 (July 2012), pp. 753–775.

[5] M. Babaei and P. R. King. "An Upscaling–Static-Downscaling Scheme for Simulation of Enhanced Oil Recovery Processes". In: *Transport Porous Med.* 98.2 (Mar. 2013), pp. 465–484.

[6] J. W. Barker and P. Dupouy. "An analysis of dynamic pseudo-relative permeability methods for oil-water flows". In: *Pet. Geosci.* 5.4 (1999), pp. 385–394.

[7] J. W. Barker and S. Thibeau. "A Critical Review of the Use of Pseudorelative Permeabilities for Upscaling". In: *SPE Reservoir Eng.* 12.2 (1997), pp. 138–143.

[8] J. Barker and F. Fayers. "Transport Coefficients for Compositional Simulation With Coarse Grids in Heterogeneous Media". In: *SPE Advanced Technology Series* 2.2 (Apr. 1994), pp. 103–112.

[9] G. A. Bartelds, J. Bruining, and J. Molenaar. "The Modeling of Velocity Enhancement in Polymer Flooding". In: *Transport Porous Med.* 26.1 (Jan. 1997), 75–88.

[10] J. Bear. *Dynamics of Fluids in Porous Media*. Dover Publications, Sept. 1972.

[11] S. Begg, R. Carter, and P. Dranfield. "Assigning Effective Values to Simulator Gridblock Parameters for Heterogeneous Reservoirs". In: *SPE Reservoir Eng.* 4.4 (1989), pp. 455–463.

[12] S. Begg and P. King. "Modelling the Effects of Shales on Reservoir Performance: Calculation of Effective Vertical Permeability". In: *SPE Reservoir Simulation Symposium, 10-13 February, Dallas, Texas.* 1985.

[13] W. J. Cardwell and R. Parsons. "Average Permeabilities of Heterogeneous Oil Sands". In: *Transactions of the AIME* 160.1 (Dec. 1945), pp. 34–42.

[14] Y. Chen and L. J. Durlofsky. "Efficient Incorporation of Global Effects in Upscaled Models of Two-Phase Flow and Transport in Heterogeneous Formations". In: *Multiscale Model. Simul.* 5.2 (2006), pp. 445–475.

[15] Y. Chen, B. T. Mallison, and L. J. Durlofsky. "Nonlinear two-point flux approximation for modeling full-tensor effects in subsurface flow simulations". In: *Comput. Geosci.* 12.3 (2008), pp. 317–335.

[16] Z. Chen, G. Huan, and Y. Ma. *Computational Methods for Multiphase Flows in Porous Media*. Computational Science & Engineering. Society for Industrial and Applied Mathematics, 2006.

[17] Z. Chen and T. Y. Hou. "A mixed multiscale finite element method for elliptic problems with oscillating coefficients". In: *Math. Comp.* 72 (2003), pp. 541–576.

[18] M. Christie. "Flow in porous media - scale up of multiphase flow". In: *Curr. Opin. Colloid Interface Sci.* 6.3 (2001), pp. 236–241.

[19] M. Christie and M. Blunt. "Tenth SPE Comparative Solution Project: A Comparison of Upscaling Techniques". In: *SPE Reserv. Eval. Eng.* 4.4 (Aug. 2001), pp. 308–317.

[20] M. Christie and P. Clifford. "Fast Procedure for Upscaling Compositional Simulation". In: *SPE J.* 3.3 (Sept. 1998), pp. 272–278.

[21] M. Christie et al. “A Renormalisation-Based Upscaling Technique for WAG Floods in Heterogeneous Reservoirs”. In: *SPE Reservoir Simulation Symposium, 12-15 February, San Antonio, Texas*. 1995.

[22] K. Coats. “A Note on IMPES and Some IMPES-Based Simulation Models”. In: *SPE J.* 5.3 (Sept. 2000), pp. 245–251.

[23] N. Darman, G. Pickup, and K. Sorbie. “A Comparison of Two-Phase Dynamic Upscaling Methods Based on Fluid Potentials”. In: *Comput. Geosci.* 6.1 (Mar. 2002), pp. 5–27.

[24] L. J. Durlofsky. “Numerical Calculation of Equivalent Grid Block Permeability Tensors for Heterogeneous Porous Media”. In: *Water Resour. Res.* 27.5 (May 1991), pp. 699–708.

[25] L. J. Durlofsky. “Upscaling of Geocellular Models for Reservoir Flow Simulation: A Review of Recent Progress”. In: *7 th International Forum on Reservoir Simulation*. 2003, pp. 23–27.

[26] L. J. Durlofsky and Y. Chen. “Uncertainty Quantification for Subsurface Flow Problems Using Coarse-Scale Models”. In: *Numerical Analysis of Multiscale Problems*. Ed. by I. G. Graham et al. Vol. 83. Lecture Notes in Computational Science and Engineering. Springer, 2012, pp. 163–202.

[27] *ECLIPSE 2013.2 Technical Description*. Schlumberger. 2013.

[28] S. Ekrann and J. O. Aasen. “Steady-State Upscaling”. In: *Transport Porous Med.* 41.3 (Dec. 2000), pp. 245–262.

[29] C. Farmer. “Upscaling: A review”. In: *Int. J. Numer. Meth. Fluids* 40.1-2 (Sept. 2002), pp. 63–78.

[30] Y. Gautier and B. Nœtinger. “Preferential Flow-Paths Detection for Heterogeneous Reservoirs Using a New Renormalization Technique”. In: *Transport Porous Med.* 26.1 (Jan. 1997), pp. 1–23.

[31] J. J. Gomez-Hernandez and A. G. Journel. “Stochastic Characterization of Grid-Block Permeabilities: from Point Values to Block Tensors”. In: *ECMOR II - 2nd European Conference on the Mathematics of Oil Recovery*. 1990.

[32] A. Iranshahr, Y. Chen, and D. V. Voskov. “A coarse-scale compositional model”. In: *Comput. Geosci.* 18.5 (Oct. 2014), pp. 797–815.

[33] P. Jenny, S. Lee, and H. Tchelepi. “Multi-scale finite-volume method for elliptic problems in subsurface flow simulation”. In: *J. Comput. Phys.* 187.1 (May 2003), pp. 47–67.

[34] S. Jonoud and M. D. Jackson. “New criteria for the validity of steady-state upscaling”. In: *Transport Porous Med.* 71.1 (Jan. 2008), pp. 53–73.

[35] A. Journel, C. Deutsch, and A. Desbarats. “Power Averaging for Block Effective Permeability”. In: *SPE California Regional Meeting, 2-4 April, Oakland, California*. 1986.

[36] P. R. King. “The use of renormalization for calculating effective permeability”. In: *Transport Porous Med.* 4.1 (Feb. 1989), pp. 37–58.

[37] S. Krogstad et al. “MRST-AD - an Open-Source Framework for Rapid Prototyping and Evaluation of Reservoir Simulation Problems”. In: *SPE Reservoir Simulation Symposium held in Houston, Texas, USA, 23-25 February 2015*. 2015.

[38] A. T. Kumar and G. Jerauld. “Impacts of Scale-up on Fluid Flow from Plug to Gridblock Scale in Reservoir Rock”. In: *SPE/DOE Improved Oil Recovery Symposium, 21-24 April 1996, Tulsa, Oklahoma*. 1996.

[39] J. Kyte and D. Berry. “New Pseudo Functions To Control Numerical Dispersion”. In: *SPE J.* 15.4 (Aug. 1975), pp. 269–276.

[40] L. W. Lake. *Enhanced Oil Recovery*. Reprint 2010. Society of Petroleum Engineers, 1989.

[41] L. W. Lake and S. Srinivasan. “Statistical scale-up of reservoir properties: concepts and applications”. In: *J. Petrol. Sci. Eng.* 44.1-2 (Oct. 2004), pp. 27–39.

[42] T. R. Lerdahl et al. “Pore- to Field Scale Multi-Phase Upscaling for IOR”. In: *SPE Europec/EAGE Annual Conference, 13-16 June 2005, Madrid, Spain*. 2005.

[43] B. Li, Z. Chen, and G. Huan. “The sequential method for the black-oil reservoir simulation on unstructured grids”. In: *J. Comput. Phys.* 192.1 (Nov. 2003), pp. 36–72.

[44] H. Li and L. J. Durlofsky. “Upscaling for Compositional Reservoir Simulation”. In: *SPE J.* Preprint (2015).

[45] K.-A. Lie. *An Introduction to Reservoir Simulation Using MATLAB*. SINTEF ICT, Department of Applied Mathematics, 2015.

[46] K. Lie et al. “Open-source MATLAB implementation of consistent discretisations on complex grids”. In: *Comput. Geosci.* 16 (2 2012), pp. 297–322.

[47] A. Lohne, G. A. Virnovsky, and L. J. Durlofsky. "Two-Stage Upscaling of Two-Phase Flow: From Core to Simulation Scale". In: *SPE J.* 11.3 (Sept. 2006), pp. 304–316.

[48] T. Manzocchi et al. "Sensitivity of the impact of geological uncertainty on production from faulted and unfaulted shallow-marine oil reservoirs - objectives and methods". In: *Pet. Geosci.* 14.1 (Feb. 2008), pp. 3–15.

[49] O. Møyner and K.-A. Lie. "A Multiscale Method Based on Restriction-Smoothed Basis Functions Suitable for General Grids in High Contrast Media". In: *SPE Reservoir Simulation Symposium held in Houston, Texas, USA, 23-25 February 2015*. 2015.

[50] O. Møyner and K.-A. Lie. "A Multiscale Restriction-Smoothed Basis Method for Compressible Black-oil Models". 2015.

[51] O. Møyner and K.-A. Lie. "A Multiscale Restriction-Smoothed Basis Method for High Contrast Porous Media Represented on Unstructured Grids". In: *J. Comput. Phys.* 304 (2016), 46–71.

[52] O. Møyner and K.-A. Lie. "A Multiscale Two-Point Flux-Approximation Method". In: *J. Comput. Phys.* 275 (2014), pp. 273–293.

[53] R. Neidinger. "Introduction to Automatic Differentiation and MATLAB Object-Oriented Programming". In: *SIAM Rev.* 52.3 (2010), pp. 545–563.

[54] L. H. Odsæter, C. F. Berg, and A. B. Rustad. "Rate Dependency in Steady-State Upscaling". In: *Transport Porous Med.* 110.3 (Sept. 2015), pp. 565–589.

[55] D. W. Peaceman. "Effective Transmissibilities of a Gridblock by Upscaling - Comparison of Direct Methods with Renormalization". In: *SPE J.* 2.3 (1997), pp. 338–349.

[56] D. W. Peaceman. *Fundamentals of Numerical Reservoir Simulation*. Vol. 6. Developments in Petroleum Science. Elsevier, 1977.

[57] G. Pickup and K. Sorbie. "The Scaleup of Two-Phase Flow in Porous Media Using Phase Permeability Tensors". In: *SPE J.* 1.4 (Dec. 1996), pp. 369–382.

[58] G. E. Pickup and K. D. Stephen. "An assessment of steady-state scale-up for small-scale geological models". In: *Pet. Geosci.* 6 (2000), pp. 203–210.

[59] G. Pickup, P. Ringrose, and A. Sharif. "Steady-State Upscaling: From Lamina-Scale to Full-Field Model". In: *SPE J.* 5.2 (June 2000), pp. 208–217.

[60] P. Renard and G. de Marsily. “Calculating equivalent permeability: a review”. In: *Adv. Water Resour.* 20.5–6 (1997), pp. 253–278.

[61] N. Saad, A. Cullick, and M. Honarpour. “Effective Relative Permeability in Scale-Up and Simulation”. In: *Low Permeability Reservoirs Symposium, 19-22 March, Denver, Colorado*. 1995.

[62] E. H. Smith. “The Influence of Small-Scale Heterogeneity on Average Relative Permeability”. In: *Reservoir Characterization II*. Academic Press, Inc., 1991, pp. 52–76.

[63] H. Stone. “Rigorous Black Oil Pseudo Functions”. In: *SPE Symposium on Reservoir Simulation, 17-20 February 1991, Anaheim, California*. 1991.

[64] *The MATLAB Reservoir Simulation Toolbox, MRST 2015b*. `www.sintef.no/MRST/`. Dec. 2015.

[65] M. Todd and W. Longstaff. “The Development, Testing, and Application Of a Numerical Simulator for Predicting Miscible Flood Performance”. In: *J. Pet. Technol.* 24.7 (July 1972), pp. 874–882.

[66] J. A. Trangenstein and J. B. Bell. “Mathematical Structure of the Black-Oil Model for Petroleum Reservoir Simulation”. In: *SIAM J. Appl. Math.* 49.3 (1989), pp. 749–783.

[67] G. A. Virnovsky, H. A. Friis, and A. Lohne. “A Steady-State Upscaling Approach for Immiscible Two-Phase Flow”. In: *Transport Porous Med.* 54.2 (Feb. 2004), pp. 167–192.

[68] X.-H. Wen, L. J. Durlofsky, and Y. Chen. “Efficient 3D Implementation of Local-Global Upscaling for Reservoir Simulation”. In: *SPE J.* 11.4 (Dec. 2006), pp. 443–453.

[69] X.-H. Wen and J. J. Gómez-Hernández. “Upscaling hydraulic conductivities in heterogeneous media: An overview”. In: *J. Hydrol.* 183.1-2 (Aug. 1996), pp. ix–xxxii.

[70] C. White and R. Horne. “Computing Absolute Transmissibility in the Presence of Fine-Scale Heterogeneity”. In: *SPE Symposium on Reservoir Simulation, 1-4 February, San Antonio, Texas*. 1987.

[71] P. Zhang, G. E. Pickup, and M. A. Christie. “A New Practical Method for Upscaling in Highly Heterogeneous Reservoir Models”. In: *SPE J.* 13.1 (Mar. 2008), pp. 68–76.

Part II

Scientific Papers

Paper I

Rate Dependent Force Balance and Upscaling of Unsteady Flooding Processes

Sindre Tonning Hilden and Carl Fredrik Berg

Submitted

Rate Dependent Force Balance and Upscaling of Unsteady Flooding Processes

Sindre T. Hilden Carl Fredrik Berg

Preprint, March 29, 2016

Abstract

A widely used approach for upscaling relative permeability is based on a steady-state assumption. For small time intervals and at small scales, the flooding process can be approximated as being in a steady state. However, at large scales with large time steps, water flooding of a reservoir is an unsteady process.

In this article we investigate the balance of viscous, capillary and gravity forces during the water flooding of a reservoir at different flow velocities. We introduce a semi-analytical method to find the low-rate limiting solution, and the high-rate solution if found by running a simulation without gravity and capillary pressure. Numerical simulations with different flow rates give the transition between these limits. We perform a series of numerical simulations both on homogeneous models, on different layered models and on a more complex two-dimensional model to investigate the force balance. The rate-dependent simulations show smooth transitions between the low- and high-rate limits. However, these transitions are in general non-trivial and the limiting cases do not give outer bounds for the simulation results.

Based on the rate-dependence of the force balance, we evaluate when different steady-state upscaling procedures are applicable for an unsteady flooding process. We observe that the capillary-limit upscaling, which also takes gravity into account, reproduces the low-rate limit fine-scale simulations. Such capillary-limit upscaling is also able to reproduce the transition to capillary equilibrium normal to the flow direction. The viscous-limit upscaling is only applicable when we have close to constant fractional flow within each coarse grid block.

1 Introduction

Two-phase incompressible flow through porous media at a macroscopic (Darcy) scale is governed by viscous, capillary and gravity forces [2, 15, 22]. The balance of these forces affects the flooding process of a reservoir, and there is thus a need for quantifying the relative influence of them.

Traditionally, the balance of these forces has been calculated from dimensionless equations, or scaling groups, including capillary and gravity numbers [15, 22, 25, 31]. The capillary number characterizes the ratio of viscous to capillary forces, while the gravity number characterizes the ratio of gravitational to capillary forces. There exists a range of more of less equivalent forms of both the capillary and the gravity number. An overview of different capillary numbers can be found in e.g., [15, Table 3-2], and an overview of different gravity numbers can be found in e.g., [25].

Deciding whether the flow is capillary, gravity or viscous dominated will depend upon which dimensionless numbers are used. Also, as the balance of forces varies temporarily in a reservoir, any single number cannot fully characterize the flow process. In [27] the two phase transport equations were formulated with terms related to viscous, capillary and gravity forces. This enabled the visualization of the changing force balance between these three forces during a simulation, both in space and time.

Reservoirs are generally heterogeneous on different length scales [1, 13], and it can be important to capture the effect of small scale heterogeneities to determine large scale flooding processes [12]. As length scales for heterogeneities might differ by several orders of magnitude, it is not always

possible to represent them all in a single model. Upscaling of flow parameters is therefore necessary to include effects of smaller scale heterogeneities into coarser scale models.

There is a wide range of upscaling methods, see e.g., [4, 8] for an overview. Two main classes of upscaling procedures are averaging methods and flow-based methods. The latter is considered more accurate, however more computationally demanding. The flow-based methods can be further divided into global and local methods [8]. Global methods are typically applied to upscaling of viscous dominated flow from a geo-cellular model to a simulation model [14, 30], while local methods are typically applied to determine effective flow properties for rock types or facies in geo-cellular models [13, 24].

Steady-state upscaling is a local upscaling method [21, 26]. Water flooding of a reservoir is a transient process, but the flooding process at a small scale, e.g., on the core scale, can still often be approximated as steady-state because the saturation changes are small relative to the volume of fluids flowing through the rock [10]. With larger scales, the steady-state assumption becomes decreasingly valid. Steady-state upscaling is therefore mainly used on a relatively small scale, e.g. from a lamina scale (mm to cm) to a bed scale (cm to m) [23].

The main challenge for a multiphase steady-state upscaling is to determine the fine-scale saturation distribution, which is rate-dependent. The limiting cases of the force balance are important for upscaling, as determining the saturation distribution can be greatly simplified in these limits [10]. On small scales, i.e., from the pore scale and up to cell sizes of about a meter, it is common to assume that capillary forces dominate for typical reservoir flow rates [6]. For very high flow rates, the viscous forces will dominate, and simplifications can again be made [10]. For intermediate flow rates, simplifications are typically not possible, and one has to perform a flow simulation on each coarse grid block with some choice of boundary conditions until a steady state is reached. In special case of a one-dimensional model, an analytical solution was used in [6] to compute the saturation distribution for intermediate flow velocities, between the limiting low- and high-rate cases.

Another challenge in steady-state upscaling is to validate the steady-state assumption. In [10], the steady-state solutions of a two-dimensional medium were studied, and the validity of the steady-state limits where assessed depending on the boundary condition and the distance from the inlet. In [11], using the inspectional analysis of [25], the force balance between capillary and viscous forces was described using dimensionless groups. These groups were then used to determine the validity of either capillary- or viscous-limit steady-state upscaling for two-dimensional layered models. It was shows that three different scaling groups were required to describe the force balance, the end-point mobility ratio, and transverse and longitudinal Peclet numbers, for flow across and along layers, respectively. A capillary number that take the geometrical distribution of rock types into account was introduced in [19], and used to determine the validity of capillary- or viscous-limit steady-state upscaling for complex three-dimensional models with a set of flow parameters.

The transition between capillary and viscous limit steady-state upscaling has been investigated for two-dimensional models in [17, 28], and later extended to three-dimensional models in [19]. It was noted that the transition between the upscaled capillary- and viscous-limit flow parameters could be non-monotonic and not necessarily bounded by the limiting cases.

In this article we will investigate the balance of forces by numerical simulations on the fine scale. We introduce a semi-analytical method for obtaining solutions of the flooding process for vanishing flow rates. Running numerical simulations dominated by capillary forces and gravity is computationally heavy, and this semi-analytical method allows us to easily establish a lower limit solution for the rate-dependent simulations. For the high-rate limit, solutions can be obtained by ignoring capillary pressure and gravity in the flow simulations. These cases serve as boundaries for the rate-dependent flow. By then considering how the solution changes with respect to the flow rate, and how it compares to the solution limits, we are able to judge when the limiting cases are valid simplifications.

In addition to studying how different forces interact on the fine scale through a wide range of flow-rates, we perform steady-state upscaling and assess for what flow-rates and scales the upscaling is valid. We include gravity in addition to viscous and capillary forces, in contrast to e.g. [11, 28]. The validity of the upscaling methods is explained in light of the fine-scale force-balance.

Upscaling, general calculations and plotting in this article are performed by the use of the

Matlab Reservoir Simulation Toolbox (MRST) [16, 18], which is an open-source toolbox for rapid prototyping of new computational methods for reservoir engineering. The flow simulations are conducted using the fully implicit solver of the commercially available reservoir simulator Eclipse 100 [9].

This article has the following outline: We state the governing flow equations in Section 2. Section 3 presents limiting solutions for the rate-dependent flooding process. In particular, we introduce a semi-analytical low-rate solution. Thereafter, we present different steady-state upscaling procedures in Section 4. In Section 5 we use simulations at different rates to investigate the force balance between viscous, capillary and gravitational forces. We observe distinct rate ranges where forces dominate along or perpendicular to the flow direction, and investigate the transition between these distinct rate regimes. We investigate steady-state upscaling procedures for the different rate regimes in Section 6 to address when the different methods are applicable. To consider the force balance and upscaling in a general context, a more complex heterogeneous model is studied in Section 7. In Section 8 we summarize and discuss the results of this article.

2 Governing Equations

We consider incompressible two-phase flow. The two phases will be denoted oil and water, represented by subscripts o and w. The continuity equations for the two phases are

$$\phi \frac{\partial s_\alpha}{\partial t} + \nabla \cdot \vec{v}_\alpha = q_\alpha, \qquad \alpha \in \{o, w\}, \tag{1}$$

where ϕ is the porosity, s_α is the saturation and q_α a source term for each phase α. The phase velocities $\vec{v}_\alpha$ are given by Darcy's law:

$$\vec{v}_\alpha = -\frac{k_{r\alpha}}{\mu_\alpha} \boldsymbol{K} \left(\nabla p_\alpha - \rho_\alpha g \nabla z \right), \qquad \alpha \in \{o, w\},$$

where $\boldsymbol{K}$ is the absolute permeability, g is the gravity, z is height above a given datum, and p_α, ρ_α, μ_α and $k_{r\alpha}$ are the phase pressures, densities, viscosities and relative permeabilities, respectively. In addition, we have the closing relation $s_w + s_o = 1$, and the capillary pressure $p_{\text{cow}}(s_w) = p_o - p_w$. If we introduce the phase mobility $\lambda_\alpha = k_{r\alpha}/\mu_\alpha$, then

$$\vec{v}_o - \frac{\lambda_o}{\lambda_w} \vec{v}_w = -\boldsymbol{K} \lambda_o (\nabla p_{\text{cow}} - \Delta\rho g \nabla z),$$

where $\Delta\rho = \rho_o - \rho_w$. Let $\vec{v} = \vec{v}_o + \vec{v}_w$ be the total Darcy velocity, and substitute $\vec{v}_o$ with $\vec{v} - \vec{v}_w$ in the above equation to obtain

$$\vec{v}_w = \frac{\lambda_w}{\lambda_w + \lambda_o} \vec{v} + \boldsymbol{K} \frac{\lambda_w \lambda_o}{\lambda_w + \lambda_o} (\nabla p_{\text{cow}} - \Delta\rho g \nabla z).$$

This expression for $\vec{v}_w$ is then inserted into the water equation (1), where we now disregard sources and sinks. By observing that combining (1) and $s_w + s_o = 1$ yields $\nabla \cdot v = 0$, we obtain

$$-\phi \frac{\partial s_w}{\partial t} = \nabla f_w \cdot \vec{v} + \nabla \cdot \Big(\boldsymbol{K} \lambda_o f_w (\nabla p_{\text{cow}} - \Delta\rho g \nabla z) \Big), \tag{2}$$

where $f_w = \lambda_w/(\lambda_w + \lambda_o)$ is the fractional flow of water. Equation (2) is a useful formulation for considering the influence of the different forces, as we discuss in the following.

3 Limiting Solutions

In this section we will investigate the two limiting solutions of the simulation of the flooding of a reservoir, given by high flow rates and negligible flow rates.

3.1 High-Rate Limit

Whereas capillary and gravity forces are not affected by flow rate, the viscous forces increase with flow rate. This can be seen from (2), where the flow rate is only contained in the viscous term $\nabla f_w \cdot \vec{v}$. For high enough flow rates, the viscous term will dominate the capillary and gravity terms, such that $\nabla f_w \cdot \vec{v} \gg \nabla \cdot [\boldsymbol{K}\lambda_o f_w(\nabla p_{\text{cow}} - \Delta\rho g \nabla z)]$, and (2) can be reduced to the following form:

$$-\phi \frac{\partial s_w}{\partial t} = \nabla f_w \cdot \vec{v}. \tag{3}$$

As the fluids are assumed to be incompressible, flow rates $\vec{v}$ scale linearly with well rates q, which can be seen from (1). Therefore simulations with different well rates yield the same flooding pattern when scaled versus rate. To find this high-rate (viscous dominated) limit solution, a simulation is run where the capillary pressure p_{cow} and density difference $\Delta\rho$ (and hence the influence of gravity) are both set to zero.

3.2 Low-Rate Limit

With diminishing flow rates, both $\nabla f_w \cdot \vec{v} \to 0$ and $\frac{\partial S_w}{\partial t} \to 0$, and the capillary and gravity forces eventually become dominant so that (2) is reduced to

$$\nabla \cdot \Big[\boldsymbol{K}\lambda_o f_w(\nabla p_{\text{cow}} - \Delta\rho g \nabla z)\Big] = 0.$$

As $\boldsymbol{K}\lambda_o f_w$ in general is spatially dependent, we then have

$$\nabla p_{\text{cow}} = \Delta\rho g \nabla z. \tag{4}$$

Thus, with diminishing flow rates the capillary and gravity forces will be in equilibrium at all times. Note that this means equilibrium in all directions, in contrast to vertical equilibrium [29].

To construct a semi-analytical solution for this limit, consider a discretized reservoir model with N grid cells. Let $\hat{p}_{\text{cow}}$ be the capillary pressure at some reference height $z = \hat{z}$, and for each grid cell $i \in [1, \ldots, N]$, let s_w^i be the water saturation, z^i the height of the cell centroid, ϕ^i its porosity and V^i its volume. Given an average saturation s_w^* for the whole domain, we can solve (4) discretely on the grid using the following equations

$$p_{\text{cow}}^i(s_w^i) = \hat{p}_{\text{cow}} - \Delta\rho g z^i, \quad i \in [1, \ldots, N], \qquad \frac{\sum_{i=1}^N s_w^i \phi^i V^i}{\sum_{i=1}^N \phi^i V^i} = s_w^*. \tag{5}$$

Solving (5) then yields a relationship between the average saturation s_w^* and the cell saturations s_w^i. The reason for first choosing s_w^*, instead of choosing a value for $\hat{p}_{\text{cow}}$ and then simply computing s_w^i by inverting the capillary pressure curves, is that in the algorithm we present below, s_w^* is the known value, while $\hat{p}_{\text{cow}}$ is unknown.

For (5) to have a solution, the capillary pressure functions $p_{\text{cow}}^i(s_w^i)$ must yield pressures in the required range. Typically, this can be obtained by using functions with asymptotes at the endpoints. The special case when only gravity forces are present needs to be handled separately. The oil-water contact will then be a sharp interface at some height, and this height is simply computed from the mean water saturation s_w^* and the pore volume, yielding the sought fluid distribution for each grid cell.

As we now are able compute the relationship between the average saturation and the saturation distribution in the domain at any given time, we are in turn able to calculate the total production as a function of the amount of injected fluids. Let the injection rate of water and oil be given as r_{inj}^w and r_{inj}^o, respectively. Oil injection is also included as a possibility because the domain we consider could be part of a larger field, and so injection of fluids may either be well injection, or flow across the boundaries of our domain from other regions of the field. Denote the total production of phase α by P_α and the total injection by I_α.

Given an initial average water saturation $s_{w,0}^*$ in the domain, we iterate forward in time to compute the production. At each iteration k, the following steps are performed

i) Compute the total injected fluid volume during the current iteration

$$\Delta V_k = \Delta V_{o,k} + \Delta V_{w,k} = r^o_{\text{inj}} \Delta t_k + r^w_{\text{inj}} \Delta t_k,$$

where $\Delta t_k = t_k - t_{k-1}$ is the time step from previous iteration (see comment on time below).

ii) Find the cell saturations $s^i_w = s^i_w(s^*_{w,k})$ by solving (5).

iii) Given the saturation distribution, calculate the relative phase flow m_α for the sinks by taking a well index weighted sum over all sink cells

$$m_\alpha = \frac{\sum_i \text{WI}^i \lambda^i_\alpha}{\sum_i \text{WI}^i}, \qquad \alpha \in \{o, w\}, \tag{6}$$

where WI^i is the well productivity index of cell i, and the sums go over all sink (production well) cells in the domain. We use the Peaceman expression for the well index [20]. For a regular grid where all cells have the same height and also the wellbore radius is equal for all production cells, (6) simplifies to $m_\alpha = \sum_i K^i \lambda^i_\alpha / \sum_i K^i$. Using these phase flow values, we can compute the fractional flow for the sinks as

$$f_{s,\alpha} = \frac{m_\alpha}{m_w + m_o}, \qquad \alpha \in \{o, w\}.$$

Thus, the produced total amount of phase α during the current iteration is given by $f_{s,\alpha} \Delta V_k$.

iv) Update the total production

$$P_{\alpha,k} = P_{\alpha,k-1} + f_{s,\alpha} \Delta V_k, \qquad \alpha \in \{o, w\},$$

and the total injection

$$I_{\alpha,k} = I_{\alpha,k-1} + \Delta V_{\alpha,k}, \qquad \alpha \in \{o, w\},$$

as well as the average saturation

$$s^*_{w,k+1} = s^*_{w,k} + \frac{\Delta V_{w,k} - f_{s,w} \Delta V_k}{\sum_i \phi^i V^i}.$$

Then continue to next iteration.

The resulting production curves P_w and P_o are independent of the magnitude of the total injection rate $r^w_{\text{inj}} + r^o_{\text{inj}}$ and the time steps Δt_k. However, the step sizes Δt_k must be chosen small enough to limit numerical errors.

This semi-analytical solution is quasi-static. As we are in the low-rate limit, the fluids are given infinite time to redistribute, but the simulation is still dynamic as the saturations move forward in time at each iteration. Thus, in this limit, the concept of time is not properly defined, and the time-step Δt_k do not correspond to a physical reservoir time.

The low-rate solution is applicable to general heterogeneous models, including three-dimensional grids. Note also that more complex wells than presented here could be implemented by e.g. incorporating hydrostatic pressure fall in the wells.

We will use the high-rate and diminishing-rate solutions described above to investigate the rate-dependent balance of forces for several flooding processes. Note that these solutions do not depend on grid cell size, while they depend on the heterogeneities represented in the model, e.g., the thickness of layers.

4 Upscaling

The single and two-phase methods we use for upscaling, which are presented below, including the viscous- and capillary-limit cases, are described in several papers, see e.g., [4, 6, 10, 21]. In the following, we will let superscript '$*$' denote an upscaled value (which may be a scalar or a tensor), such that e.g. $\boldsymbol{K}^*$ denotes the upscaled value of the permeability field $\boldsymbol{K}$. We present the upscaling methods by considering a general domain Ω of a fine grid that is to be upscaled to a single coarse grid block Ω^c.

4.1 Single Phase Upscaling

For a single phase, Darcy's law $\vec{v} = -\boldsymbol{K}\nabla p$ and the continuity equation $\nabla \cdot \vec{v} = 0$ give the Laplace equation

$$\nabla \cdot (\boldsymbol{K}\nabla p) = 0. \tag{7}$$

The solution of this equation depends on the choice of boundary conditions applied. Assume first that fixed (Dirichlet) boundary conditions are applied. For each direction $d \in \{x, y, z\}$, a pressure drop Δp is applied across the domain Ω, and the pressure equation (7) is solved to obtain the pressure p, and thereby also the flux field $\vec{v}_d$. Let $\bar{v}_d$ then be the average flux through any cross-section perpendicular to the direction of the pressure drop. The upscaled permeability in direction d is then given by

$$\boldsymbol{K}^{*,d} = \frac{L_d}{\Delta p}\bar{v}_d, \tag{8}$$

where L_d is a representative distance between the inflow and outflow boundaries. This upscaling is performed in turn for each direction, and the upscaled permeability becomes a diagonal tensor

$$\boldsymbol{K}^* = \mathrm{diag}(K^{*,x}, K^{*,y}, K^{*,z}).$$

Herein, we apply Dirichlet boundary conditions in the flow direction with no-flow boundary conditions elsewhere, and thus get upscaled diagonal permeability tensors. If periodic boundary conditions are chosen instead, the upscaled permeability becomes a full 3×3 tensor as cross-flow may be present [7].

4.2 Two Phase Upscaling

It is well known that two-phase upscaling is rate dependent, with capillary and gravity forces dominating for small grid scales and at low flow rates, while viscous forces dominate for large grid scales and at high rates [10]. We consider upscaling in these two outer limits, where the situation can be simplified, whereas upscaling at intermediate flow rates is not considered herein.

The first step of a steady-state two-phase upscaling is calculating the saturation distribution $\hat{s}_w$ at steady-state. For the diminishing rate *capillary-limit* (or *capillary-gravity-limit*), this distribution is found by solving (5) for some given value of the average saturation s_w^*. Then, the phase permeabilities $\widetilde{\boldsymbol{K}}_\alpha = k_{r\alpha}(\hat{s}_w)\boldsymbol{K}$ are computed, and we apply a single-phase upscaling to obtain upscaled (effective) phase permeabilities $\widetilde{\boldsymbol{K}}_\alpha^{*,d}$. The upscaled relative permeabilities are then computed as

$$k_{r\alpha}^{*,d}(s_w^*) = \frac{\widetilde{\boldsymbol{K}}_\alpha^{*,d}}{\boldsymbol{K}^{*,d}}. \tag{9}$$

The capillary pressure is also upscaled using the same saturation distribution $\hat{s}_w$. In the solution of (5), the capillary pressure is constant at each height of the domain, and a natural choice for the upscaled capillary pressure value is to select the capillary pressure at the coarse cell centroid height z_c. That is,

$$p_{\mathrm{cow}}^*(s_w^*) = \hat{p}_{\mathrm{cow}} - \Delta\rho g\left(z_c - \hat{z}\right),$$

where we recall that $\hat{p}_{\mathrm{cow}}$ is the capillary pressure at the reference height $\hat{z}$. Note that if we choose the characteristic height in (5) to be $\hat{z} = z_c$, then simply $p_{\mathrm{cow}}^*(s_w^*) = \hat{p}_{\mathrm{cow}}$. This process of upscaling relative permeability and capillary pressure is repeated for different values s_w^* to obtain full upscaled curves. The upscaling is also performed for each spacial dimension. Note that we normally refer to this method by the term *capillary-limit* upscaling, but the upscaling also accounts for gravity forces if they are present.

The high-rate *viscous-limit* assumes that viscous forces dominate, and (3) applies. Assuming steady-state, the time derivative of the saturation goes to zero, and (3) further reduces to

$$\nabla f_w \cdot \vec{v} = 0. \tag{10}$$

Thus, the fractional flow is constant along streamlines, and the solution to (10) depends on the distribution of fractional flow over the inlet face of the coarse grid block. In particular, this means

the solution is not unique. A common choice is to assume a constant fractional flow on the whole inlet boundary, resulting in constant fractional flow throughout the coarse grid block [6]. With this assumption, the saturation distribution for each fractional-flow value $\hat{f}_w$ is obtained by inverting the fractional flow function f_w, such that $\hat{s}_w = f_w^{-1}(\hat{f}_w)$. Similar to the diminishing-rate limit, once the saturation distribution is found, we apply a single-phase upscaling for the phase permeabilities $\widetilde{\boldsymbol{K}}_\alpha = k_{r\alpha}(\hat{s}_w)\boldsymbol{K}$ to obtain upscaled (effective) phase permeabilities, and then the upscaled relative permeabilities are computed from (9). This process is repeated for different fractional-flow values $\hat{f}_w$ to obtain upscaled relative permeabilities for different values of the corresponding average saturation. We set the upscaled capillary pressure equal zero for the viscous-limit upscaling.

5 Simulation Examples

We will investigate how gravity, capillary pressure and viscous forces are present at different flow rates during a water flooding of a reservoir. In particular, we investigate at what rates each of these forces can be ignored, and thus find when the limiting solutions are valid. To this end, we consider different simplified examples of water flooding of an oil filled reservoir. We first use a homogeneous 1D example to investigate the balance of capillary versus viscous forces in the direction of flow. Then we extend the homogeneous model to 2D to investigate the balance of gravity versus viscous forces. Finally, to investigate the capillary (and gravity) redistribution of fluids both perpendicular and along the flow direction, we add heterogeneities by assigning different rock types to different layers.

The three forces considered will generally depend non-linearly on each other and are thus not truly separable. However, to quantify at what flow rates each force has significant impact on the solution, we simplify and consider the effects of the forces separately.

5.1 General Model Description

The example models considered in this section are all derived from the same base case that is of physical dimensions $2000 \times 5 \times 20$ m and has a grid size of $400 \times 1 \times 20$ cells. Sketches of two different variations are shown in Fig. 1 below. There are two rock types used; a higher permeable rock (type 1) with permeability $K_1 = 1000$ mD, and a lower permeable rock (type 2) with $K_2 = 10$ mD. The permeability within each rock type is homogeneous and isotropic, and the porosity is constantly equal $\phi = 0.25$ for the entire domain. Depending on the example, we use either equal mobilities and linear relative permeabilities,

$$\mu_o = 1.0\,\text{cP}, \quad \mu_w = 1.0\,\text{cP}, \quad k_{rw}(s_w) = \widetilde{s}_w, \quad k_{ro}(s_w) = 1 - \widetilde{s}_w. \tag{11}$$

or different phase viscosities and quadratic relative permeability curves,

$$\mu_o = 1.5\,\text{cP}, \quad \mu_w = 0.5\,\text{cP}, \quad k_{rw}(s_w) = 0.5(\widetilde{s}_w)^2, \quad k_{ro}(s_w) = (1 - \widetilde{s}_w)^2, \tag{12}$$

where $\widetilde{s}_w(s_w) = (s_w - s_{wir})/(1 - s_{wir} - s_{or})$. The same relative permeability functions apply to both rock types, the irreducible water saturation is $s_{wir} = 0.1$ and the residual oil saturation $s_{or} = 0.1$, and the initial water saturation is set equal the irreducible water saturation in the entire domain for all simulations. If nothing else is stated, then the densities are set to $\rho_o = 925\,\text{kg/m}^3$ and $\rho_o = 1025\,\text{kg/m}^3$. The capillary pressure curves are computed from a Leverett J-function, such that

$$p_{\text{cow}}(s_w) = J(s_w)\gamma\cos\theta\sqrt{\phi/K}, \tag{13}$$

where $J(s_w)$ is the Leverett J-function, γ is the surface tension and θ is the contact angle between water and oil, ϕ is porosity and K is permeability. For the examples herein, we have chosen to use $\gamma = 22\,\text{dyn/cm}$ and $\theta = 45°$. The J-function we use is from tabulated data, and the resulting p_{cow} curve for rock type 1 ($\phi = 0.25$, $K = 1000$ mD) can be seen in Fig. 4.

An injection well is included at the west end of the model, and a producer is included at the east end. For each model variation considered, simulations are performed for a series of different injection rates. Throughout each of these simulations, the wells are injecting and producing at a constant rate until 2 PV (pore volumes) of water have been injected.

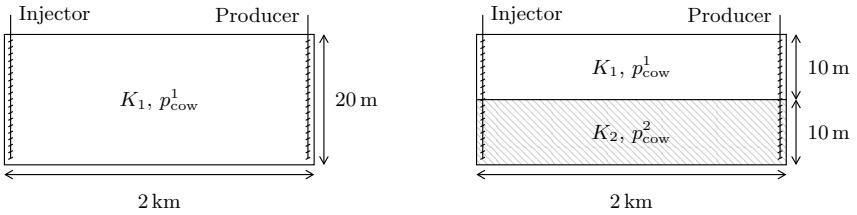

Figure 1: Sketches of two of the models considered in the examples. Left: Homogeneous model. Right: Model with two horizontal layers.

5.2 Homogeneous 1D Example

We start by investigating the force balance in a 1D homogeneous horizontal case. Since all grid cells have the same height above datum, there will be no contribution of gravity. The only competing forces are then the viscous and capillary forces, and (2) simplifies to

$$-\phi\frac{\partial S_w}{\partial t} = \nabla f_w \cdot \vec{v} + \nabla \cdot (\boldsymbol{K}\lambda_o f_w \nabla p_{\text{cow}})\,. \tag{14}$$

The homogeneous 1D model has the same physical dimensions as the general model, and consists only of rock type 1, such that the permeability is $K_1 = 1\,\text{D}$ in the entire domain. In this example, the viscosities are unequal and the relative permeabilities are quadratic, as given by (12).

To investigate the balance of forces, we run simulations for a range of different injection rates. The flow rate through the domain is represented by the *interstitial (seepage) velocity* $u = v/\phi = Q/(A\phi)$, where Q is the injection rate and $v = Q/A$ is the corresponding Darcy velocity (specific discharge). Thus, the interstitial velocity gives flow in the units of length per time, and we use m/day. To maintain approximately the same numerical accuracy, the time steps are adjusted relative to the flow rate, such that the same number of time steps are used in all simulations.

Some of the resulting total oil production curves are plotted as a function of total injected water for different interstitial velocities in Fig. 2, where also the limiting solutions are shown. These limits are computed as described in Section 3. We observe that the rate dependent solutions converge to the low-rate (capillary dominated) limit for lower rates and to the high-rate (viscous dominated) limit for higher rates.

To better visualize the transition of the solution between the low-rate and high-rate solution limits, and also to see at what rates the solution converges, another comparison of the simulations is shown in Fig. 3. Here, the total oil production is plotted as a function of the velocity at the point where 0.8 PV (pore volume) of water has been injected into the domain. In other words, Fig. 3 shows the intersection of the curves in Fig. 2 at the point indicated by the dotted vertical line. The results for two shorter models are also included in Fig. 3 to show how the results depend on the model length.

At low injection rates, the viscous term $\nabla f_w \cdot \vec{v}$ in (14) will go towards zero as $|\vec{v}| \to 0$. Then the capillary forces are given enough time to redistribute the fluids throughout the domain, resulting in the capillary forces being in equilibrium. For the homogeneous model, this means that the saturation will be close to constant in space at each point in time. Considering Fig. 3, we see that the rate dependent solutions converge towards the low-rate limit as the flow velocity decreases. However, for the 2000 m model the velocity needs to be as low as 10^{-6} m/day for the rate-dependent solutions to converge to the calculated low-rate limit.

For high enough injection rates, on the other hand, the Darcy velocity $\vec{v}$ in equation (14) becomes so large that $\nabla f_w \cdot \vec{v} \gg \nabla \cdot (\boldsymbol{K}\lambda_o f_w \nabla p_{\text{cow}})$, and the viscous forces dominate the flow. We see in Fig. 3 that the rate-dependent solutions converge to the high-rate limiting case, and the transition going from the low-rate to the high-rate limit is relatively smooth.

The time needed for the capillary forces to redistribute the fluids is proportional to the length the fluids need to be transported. Thus when the length of the model is reduced by one order of magnitude, e.g., from 2000 to 200 meters, the time needed to redistribute the fluids is reduced by

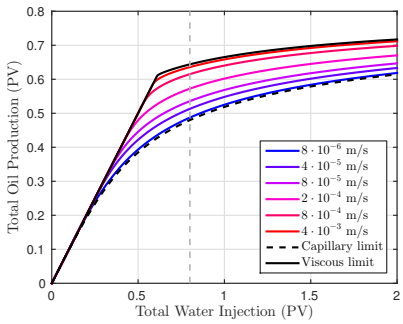

Figure 2: Total oil production for the homogeneous 1D model of length 2000 m for different interstitial velocities.

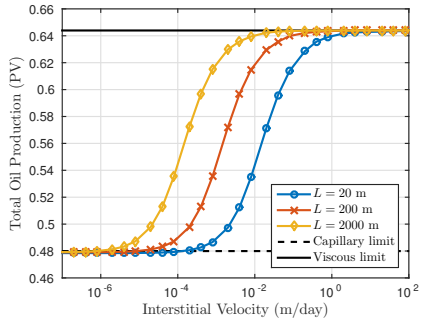

Figure 3: Total oil production after 0.8 PV of water injection (at vertical line in Fig. 2) for homogeneous 1D model of different lengths.

one order of magnitude too. This is clearly seen in Fig. 3, where the solutions for three different model lengths are plotted.

A realistic interstitial velocity for water flooding of an oil reservoir is in the order of 1 m/day [3]. In Fig. 3 we observe that all three model lengths are in the viscous-dominated regime for this velocity. However, by just considering the plot, it does seem like models shorter than 20 meters start to move away from the high-rate limit for an interstitial velocity of 1 m/day. If the same trend continues, we need models shorter than approximately 2 mm to be at the low-rate limit solution for realistic velocities. Note that this length is for an isolated domain, giving a maximum possible change of water saturation through the simulation. Also note that this is not a length restriction for capillary-limit *upscaling*. As we will see in later examples, capillary-limit upscaling may be valid for flow-rates larger than the low-rate limit solution.

This force balance depends on relative permeability, capillary pressure curves and the viscosity of the fluids. Still, for realistic flow parameters, viscosities and flow rates we cannot assume capillary equilibrium in the flow direction for typical reservoir models.

5.2.1 Capillary Number

We now define a dimensionless capillary number N_c to describe the ratio of viscous to capillary forces in the flow direction. This capillary number is given as

$$N_c = \frac{\widetilde{\nabla p}}{\widetilde{\nabla p}_{\text{cow}}},$$

where $\widetilde{\nabla p}$ is a characteristic number for the pressure change in the domain, and $\widetilde{\nabla p}_{\text{cow}}$ for the capillary pressure change.

The characteristic number for the pressure change is constructed from Darcy's law. Setting the relative permeability to one, we obtain

$$\widetilde{\nabla p} = \frac{v\widetilde{\mu}}{\widetilde{K}},$$

where $\widetilde{\mu} = (\mu_w + \mu_o)/2$, and $\widetilde{K}$ is a representative value of the permeability over the domain, and v is the Darcy velocity.

The characteristic number for the capillary pressure change is constructed as follows. Given the capillary pressure function $p_{\text{cow}}(s_w)$, divide its domain into N intervals of equal length, such that interval i is $[s_w^i, s_w^{i+1}]$, and thus $s_w^1 = s_{wir}$ and $s_w^{N+1} = 1 - s_{or}$. On each interval, compute the the discrete slope of the function by

$$d^i = \frac{p_{\text{cow}}(s_w^{i+1}) - p_{\text{cow}}(s_w^i)}{s_w^{i+1} - s_w^i}, \qquad i = 1, \ldots, N.$$

Let M be the median of all the discrete slopes d^i, and let L be the length of the domain we consider. We then define

$$\widetilde{\nabla p}_{\text{cow}} = \frac{(1 - s_{or} - s_{wir})|M|}{L}.$$

Note that we choose the median and not the mean, because we do not want extreme asymptotes at the ends to dominate.

For the 1D homogeneous example discussed just above, the constants appearing in N_c are given by $s_{wir} = 0.1$, $s_{or} = 0.1$, $\widetilde{\mu} = 1\,\text{cP}$, $\widetilde{K} = 1\,\text{D}$, $M \approx -0.05\,\text{bar}$ and the model length L varies. To illustrate how the number M relates to the capillary pressure, the line $p_c(s_w) = Ms_w + b$ is plotted on top of p_{cow} in Fig. 4, where b is chosen to minimize the distance from p_{cow}.

In Fig. 5, each of the three transition curves from Fig. 3 are plotted against the capillary number

$$N_c = \frac{\widetilde{\nabla p}}{\widetilde{\nabla p}_{\text{cow}}} = \frac{v\widetilde{\mu}}{\widetilde{K}} \frac{L}{(1 - s_{or} - s_{wir})|M|} \approx (2.93\,\text{day/m}^2)vL,$$

where the velocity v is given in units of m/day (for direct comparison with Fig. 3), and the length L is given in m. We see that the capillary number $N_c = 1$ in the middle of the transition from low-rate to high-rate limit for each of the three model lengths. Also, the capillary number is seen to be independent of the model length. Thus the capillary number N_c is reasonable for this example.

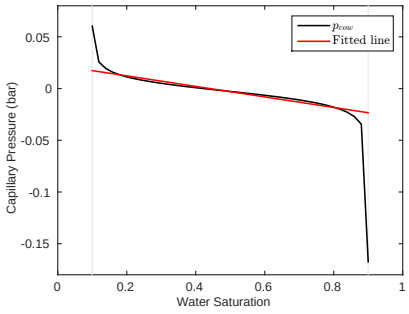

Figure 4: Capillary pressure and the fitted line found from median slope fit.

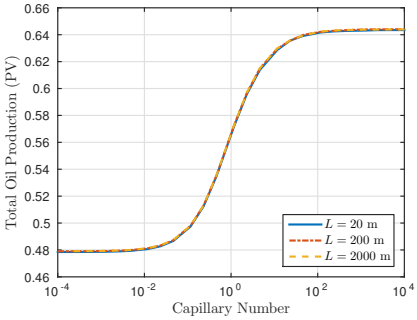

Figure 5: The production from Fig. 3 plotted against the capillary number N_c.

5.3 Homogeneous 2D Example

To consider gravitational forces, we now move to a two-dimensional model. Consider the base case of length 2000 m and height 20 m with 20 grid cells in the vertical direction. For simplicity, and to be able to study the effect of gravity, we ignore capillary forces. The competing forces are then the viscous and gravitational forces, and (2) simplifies to

$$-\phi \frac{\partial S_w}{\partial t} = \nabla f_w \cdot \vec{v} - \nabla \cdot (\boldsymbol{K}\lambda_o f_w \Delta\rho g \nabla z)\,. \tag{15}$$

The simulations are once again run for a range of injection rates, and similar to the 1D case, we plot in Fig. 6 the total oil production after 0.8 PV of water has been injected. The fluid density difference $\Delta\rho = \rho_w - \rho_o$ is varied, and both linear and quadratic relative permeability curves are considered.

For the lowest injection rates, the simulations become numerically challenging because it is difficult for gravity alone to distribute the water in the horizontal direction. To be able to run these lowest rates, a small capillary pressure is added, which helps to distribute the water and does not change the results notably.

Analogous to the balance between capillary and viscous forces in the previous example, the gravitational forces will now be dominant for small enough injection rates, as can be seen from (15). At the low-rate limit, the solution will be at vertical equilibrium. This gives a sharp oil-water contact at some height in the domain, with residual oil saturation below and irreducible water saturation above. This horizontal interface will gradually move upwards as the domain becomes water-filled from the bottom up.

Going from the low-rate solutions towards higher rates, the viscous forces will become more dominant, and the flow gradually changes character to a piston-like flooding. This transition can be seen in both plots in Fig. 6. In the case of linear relative permeability, for rates above this transition, the water front is a sharp vertical interface, such that almost all mobile oil has been produced at water breakthrough. For the case of quadratic relative permeability, however, there is a second transition. At the top of the transition curve, the water front is tilted, as gravity still has time to segregate the fluids and create a gravity tongue (shown in Fig. 7a). Due to the fluid segregation, the saturation in the tongue is close to residual oil. When the velocity is increased further, gravity does not have time to separate the fluids, and the water front is perpendicular to the flow direction (Fig. 7b). Significant oil is left behind the water front due to the shape of the relative permeability curves, causing less oil to be produced after 0.8 PV of water than when we had a gravity tongue. This can be seen as the second transition down towards the high-rate limit.

For water and oil a typical density difference $\Delta\rho = \rho_w - \rho_o$ can be approximately $150\,\mathrm{kg/m^3}$. For a realistic interstitial velocity of $1\,\mathrm{m/day}$, we see from Fig. 6 that we are at the high-rate limit solution in the case of linear relative permeability curves, but not for quadratic curves. If the trend of the density difference continues similarly, we need almost equal fluid densities to be at the high-rate limit at realistic flow rates with quadratic curves. Thus, in this example we cannot ignore the effect of gravity, and it seems like neither of the limit solutions are valid assumptions.

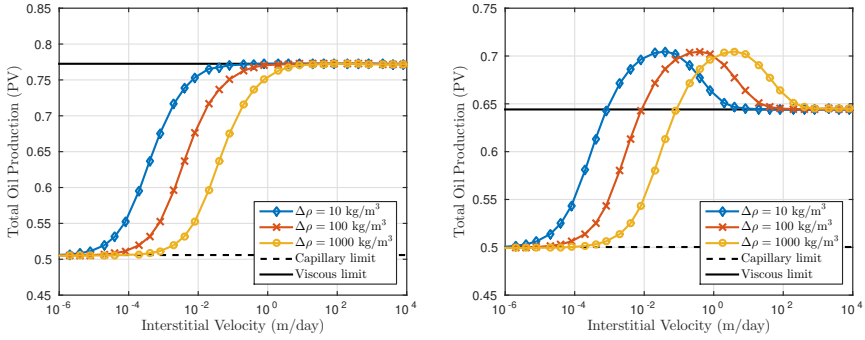

(a) Linear relative permeability, $\mu_o = \mu_w$. (b) Quadratic relative permeability, $\mu_o > \mu_w$.

Figure 6: Total oil production after injection of 0.8 PV of water for the homogeneous 2D model with gravity and without capillary pressure. Different fluid density differences $\Delta\rho = \rho_w - \rho_o$ are used.

To observe how capillary pressure now affects the results, we add capillary forces into the system. The capillary pressure is scaled with the density difference $\Delta\rho$ to get equal relative difference between capillary and gravity forces. We compute p_{cow} from (13) based on permeability $K = |\Delta\rho| \times 100\,\mathrm{mD}$ in Fig. 8a, and based on $K = |\Delta\rho| \times 1000\,\mathrm{mD}$ in Fig. 8b. Thus, for the case where $\Delta\rho = 10\,\mathrm{kg/m^3}$ in Fig. 8a, the capillary forces are based on the true permeability of $K = 1000\,\mathrm{mD}$. For all the remaining cases, the capillary pressure is larger than its normal value. As the capillary forces increase relative to the gravity, the diffusion increases both normal to and along the flow direction. In Fig. 8b, the capillary forces become so large that capillary diffusion dominates gravitation normal to the flow direction, and the flow becomes essentially one-dimensional. This can also be seen as the shape of the curves in Fig. 8b are similar to the one-dimensional results in Fig. 3.

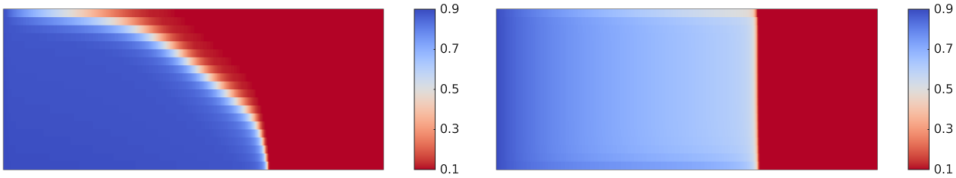

(a) Interstitial velocity 0.04 m/day, at the top of the transition curve in Fig. 6b.

(b) Interstitial velocity 8 m/day, to the right of the transition, at the high-rate limit in Fig. 6b.

Figure 7: Water saturation after injection of 0.4 PV of water for the homogeneous 2D model with gravity and without capillary pressure, using quadratic relative permeability, $\mu_o > \mu_w$, and $\Delta\rho = 10\,\mathrm{kg/m^3}$ for two different velocities.

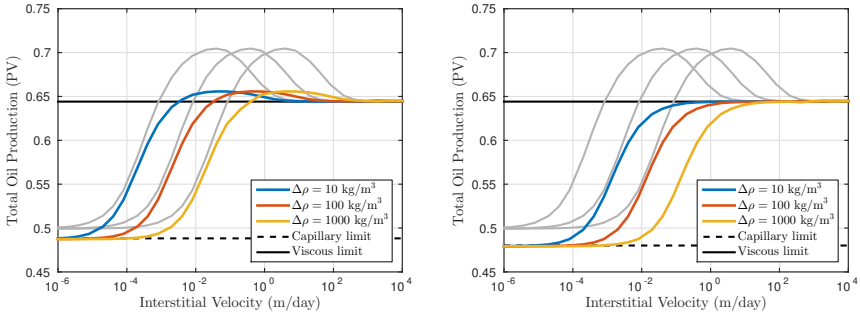

(a) p_{cow} based on $K = |\Delta\rho| \times 100\,\mathrm{mD}$.

(b) p_{cow} based on $K = |\Delta\rho| \times 1000\,\mathrm{mD}$.

Figure 8: Total oil production after injection of 0.8 PV of water for the homogeneous 2D model with gravity and capillary pressure computed from (13). The curves without any capillary pressure from Fig. 6b is shown in gray for comparison.

5.4 Layered 2D Example

To investigate the balance between capillary and viscous forces perpendicular to the flow direction, we consider a 2D model consisting of horizontal layers of two different rock types. To isolate the forces arising from capillary pressure, we let the oil density be equal to the water density to remove gravity effects. We use equal viscosities and linear relative permeabilities as given by (11), causing equal total mobility in the two rock types. There is then no viscous cross-flow between the layers arising from total mobility contrast. The capillary pressure curves for the two rock types are computed from (13).

We consider three different models, where the physical size in all cases is $2000 \times 5 \times 20\,\mathrm{m}$, while the number of layers changes. Thus, the thickness of each layer is the height of the model divided by the number of layers. Alternate layers were of rock type 1 and 2, starting from the top with the high permeable rock type 1. A sketch of the model with two layers is shown in Fig. 1.

As in previous examples, simulations are carried out for a range of injection rates. The resulting total oil production after injection of 0.8 PV of water for the different layered models is plotted in Fig. 9. This plot reveals two distinct transitions. At interstitial velocities below $10^{-5}\,\mathrm{m/day}$, the capillary forces dominate the distribution of the fluids, and the solutions are seen to converge to the low-rate limit. That is, the capillary forces are both in vertical and horizontal equilibrium. When increasing the flow rate up towards $10^{-2}\,\mathrm{m/day}$, the viscous forces become dominant in the distribution of fluids in the direction of flow. However, the distribution of fluids perpendicular to the flow is still dominated by capillary forces, and we thus still have a vertical equilibrium. That there are different forces dominating along and perpendicular to the flow direction is mainly due to differences in lengths; the model length horizontally is much larger than the lengths between the

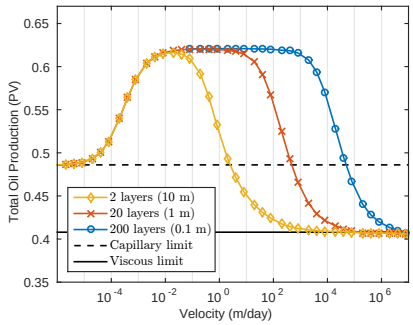

Figure 9: Total oil production after injection of 0.8 PV of water for the horizontally layered models without gravity. The height of a single layer is written in parenthesis.

layers in the vertical direction. Thus, the capillary pressure uses less time to redistribute the fluids vertically between the layers than horizontally along the layers. For velocities around 10^{-2} m/day this results in a piston-like flooding scenario where capillary forces are in equilibrium normal to the flow direction. In Fig. 9 we observe that the transition from capillary equilibrium in both directions to a plateau where we only have equilibrium normal to the flow direction is similar for different number of layers. This transition is also similar to what was observed in the 1D homogeneous case plotted in Fig. 3, thus the force balance in the direction of flow appears similar to the 1D homogeneous case.

The three models considered here all have equal volume of each of the two rock types, which causes the transition from capillary equilibrium to vertical equilibrium to be equal, and all three models end at the same plateau at 10^{-2} m/day. With even higher rates, the viscous forces become so large that capillary forces no longer have time to redistribute the fluids perpendicular to the flow direction. This is seen as the second transitions in Fig. 9, where the solutions go from vertical equilibrium at the plateau and down towards the high-rate limit. In this transition, the solutions move from a piston-like flooding with vertical equilibrium (perpendicular to the flow), to a scenario where the high-permeable layers are flooded before the low-permeable layers. This causes negligible production of oil from the low-permeable layers after injection of 0.8 PV of water, and therefore the production at 0.8 PV seen in Fig. 9 drops from vertical equilibrium to the high-rate limit. As the constant total mobility ensures no viscous cross-flow between the layers at higher rates, all models have the same high-rate limit solution.

Observe that the transition from the plateau to the high-rate limit is different for the different layered models. When increasing the number of layers, the vertical distance between grid cells of different rock type is reduced. Increasing the number of layers thus increases the gradient of the capillary pressure $\nabla p_{\text{cow}} = \Delta p_{\text{cow}}/l$ by reducing the distance l between grid cells of different rock types. At the same time we also reduce the distance the fluids need to be transported between the layers. Decreasing the distance l by an order of magnitude will then increase the capillary-pressure gradient by an order of magnitude and at the same time reduce the transport distance by an order of magnitude. Consequently, increasing the number of layers by *one* order of magnitude will shift the transition from the plateau to the high-rate limit by *two* orders of magnitude. This is seen in Fig. 9.

We also see from Fig. 9 that with a layer thickness of approximately 1 m (model of 20 layers), the transition from the plateau to the high-rate limit starts at an interstitial velocity of just above 10 m/day. Thus, for a model with layers thinner than approximately 1 m, a typical reservoir flow rate is at the plateau where viscous forces dominate in direction of the flow, while capillary forces dominate perpendicular to the flow.

6 Upscaling Examples

In this section we investigate the validity of steady-state upscaling methods. The models are upscaled from a fine grid to a coarse grid, and then these upscaled parameters are used in simulations to observe how well they are able to reproduce the fine-scale flow and how large errors the upscaling introduces.

6.1 Upscaling the Horizontally-Layered Models Without Gravity

Consider the layered models introduced above with 2, 20 and 200 horizontal layers. We upscale these models to a coarse grid of size $40 \times 1 \times 1$. In all three models, half the domain of each coarse grid block is filled by rock type 1 and the other half by rock type 2, therefore the upscaled flow parameters will be identical.

As the layers are parallel to the flow direction, the upscaled absolute permeability is simply the arithmetic mean, such that $K^* = (1000\,\text{mD} + 10\,\text{mD})/2 = 505\,\text{mD}$. The relative permeabilities are upscaled using both the viscous- and capillary-limit methods, and are shown in Fig. 10a together with the original input curves. Note that the viscous-limit upscaling reproduces the input curves, in contrast to the capillary-limit. The upscaled capillary pressure is shown in red in Fig. 10b.

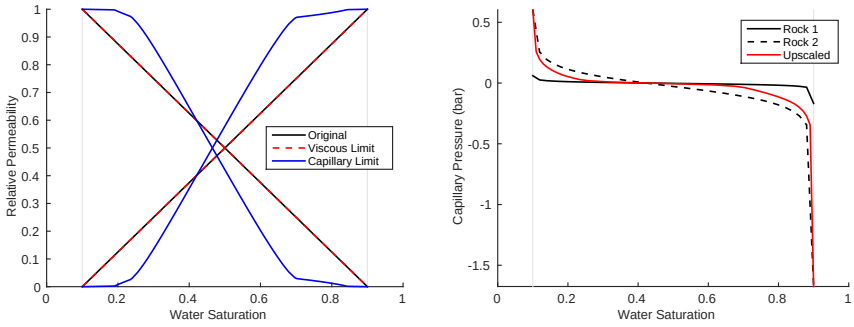

(a) Relative permeability.

(b) Capillary pressure.

Figure 10: Upscaled fluid properties for the horizontally layered models.

As before, simulations are run using a range of injection rates to observe how well the upscaled curves reproduce the fine-scale results. The total oil production resulting from simulations with lower velocities using capillary-limit upscaled data are shown in Fig. 11. The fine-scale solutions in the low and high-rate limits are shown for comparison, and we observe how the coarse simulations converge to the low-rate limit.

To better visualize how the solutions depend on velocity, the total oil production for all solutions are plotted after injection of 0.8 PV of water in Fig. 12. As there is no capillary pressure in the viscous coarse model, these results are rate-independent when plotted against total injection. We also observe that the viscous-limit upscaling do *not* reproduce the fine-scale solution at the high-rate limit. The coarse results give approximately two times the total production compared to the fine scale. The reason for this mismatch becomes evident when considering the fractional flow during the flooding. For the fine-scale models, once the water saturation front has passed through in the high-permeable layers, the water fractional flow will be close to one in these layers, and still close to zero in the low-permeable layers. The steady-state viscous-limit upscaling procedure assumes constant fractional flow inside each coarse grid block, and this assumption is clearly violated in this case. We therefore cannot expect the viscous-limit upscaling to capture the characteristics of the flow. However, if the coarse grid resolved the layered structure, i.e., if each coarse block only contained a single rock type, then the fractional flow would be close to constant within each block, away from the water front. In this case, the viscous-limit upscaling could be applied, and would match the high-rate limit solution.

Another point about the high-rate limit is worth noting. In the high-rate limit, close to all flow in the fine-scale solution happens in the high-permeable layers, which adds up to only half the flow-area. For the coarse models, on the other hand, the flow is equal for the full area of the model. This causes the water front in the coarse model to move slower than in the fine-scale model, and water break through happens at a later point in time. Thus, for this choice of coarse grid, both upscaling methods are incorrect for the high-rate limit, even before the water break through.

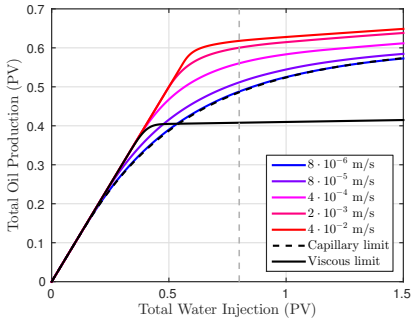

Figure 11: Total oil production for different interstitial velocities using the capillary-limit upscaled parameters for the horizontally-layered models.

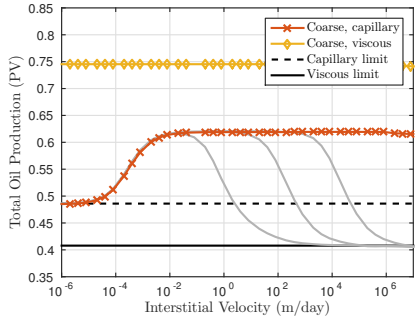

Figure 12: Total oil production after injection of 0.8 PV of water for upscaled horizontally-layered models without gravity. Fine-scale results from Fig. 9 are shown in gray.

Considering the capillary-limit results in Fig. 12, we see the coarse capillary simulations not only converge to the fine-scale low-rate limit, but also have the same transition from the low-rate limit and up to the plateau where the capillary forces are in equilibrium in the direction perpendicular to flow. At this plateau and for lower rates the vertical fluid distribution is captured by the capillary-limit upscaling procedure. For higher flow rates the viscous forces begin to influence the vertical fluid distribution, and this distribution is not captured by the upscaled model, as seen in Fig. 12, where the upscaled results are unchanged when increasing the flow rates after reaching the plateau.

6.2 Upscaling Horizontally-Layered Models with Gravity

In this subsection we combine capillary and gravity forces and study the horizontally layered model with 20 layers. Three different density differences $\Delta\rho = \rho_w - \rho_o$ are used. The upscaled relative-permeability and capillary-pressure curves are shown in Fig. 13. When upscaling a gravity case, we observe how the gravity effect is included into both the upscaled relative permeability and capillary pressure curves. For the largest density contrast, the resulting capillary curve is dominated by the effect of gravity. Note that the horizontally-layered model has alternate layers, starting with the high permeable rock type at the top. The results in this section would be slightly different if the layer ordering was switched, but for as many as 20 layers, this difference is minimal.

The model is upscaled to a 1D grid of size $40 \times 1 \times 1$ and then simulations are run on the coarse scale. The total oil production after 0.8 PV water injected versus interstitial velocity is shown in Fig. 14a. As expected, the solution for the relatively low density difference of $10\,\mathrm{kg/m^3}$ in Fig. 14a is similar to the solution without gravity in Fig. 12. As the gravity forces are increased, the shape of the transition changes.

To make Fig. 14a more readable, we do not include the viscous-limit results, but as for the results without gravity, the viscous-limit upscaling do not reproduce the fine scale high-rate limit solution here either. The capillary-limit upscaling does however have a good match with the fine-scale results from the low-rate limit and up the point where viscous forces become dominant in the coarse simulations. Note that the low-rate limit is slightly different depending on the density difference, which reflects the change in the balance between gravity and capillary forces at this limit.

At high rates, the coarse simulation reproduces vertical equilibrium, which seems to correspond to the top of the fine-scale simulation curves. Viscous influence on fluid distribution normal to the flow direction is not captured by the upscaled models, thus the transition from vertical equilibrium to the high-rate limit solution is not captured by the upscaled models. Depending on the size of the density difference $\Delta\rho$, the coarse results match the fine-scale results up to around $0.01 - 1\,\mathrm{m/day}$.

To illustrate the effect of including the effect of gravity in the capillary-pressure upscaling, the coarse results are shown in Fig. 14b where gravity has been disregarded when upscaling p_{cow}, but still included when upscaling relative permeability. We observe how the coarse models do not match the low-rate limit as the density difference increases, and the transitions towards higher flow rates are not matching the fine-scale simulations. This shows the importance of including gravity also in the capillary-pressure upscaling.

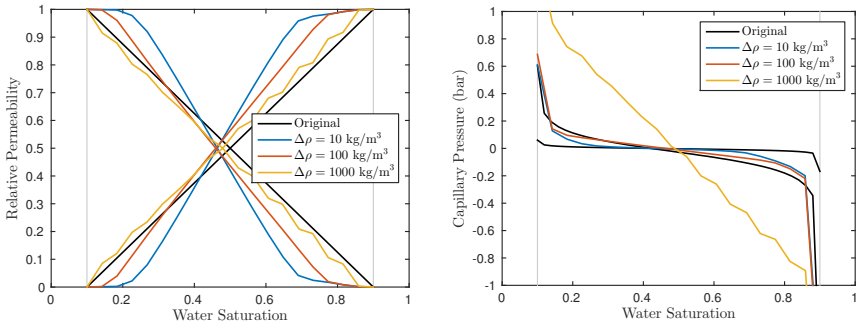

(a) Relative permeability.

(b) Capillary pressure.

Figure 13: Upscaled fluid properties for the horizontally layered model with 20 layers, including gravity and capillary pressure forces for different fluid density differences $\Delta\rho = \rho_w - \rho_o$.

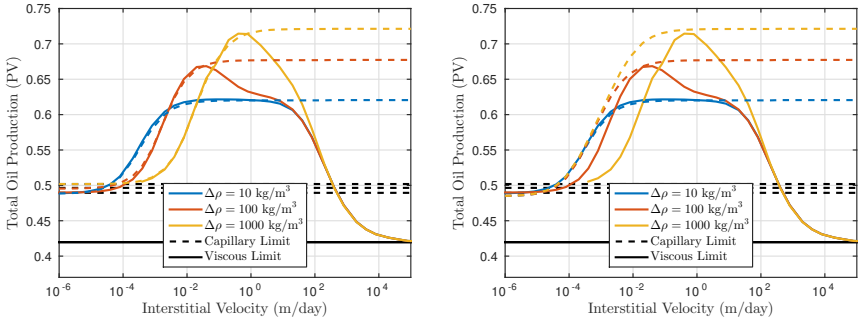

(a) Default upscaling.

(b) Disregarding gravity in p_{cow}-upscaling.

Figure 14: Total oil production after injection of 0.8 PV of water injection for the model with 20 horizontal layers with capillary pressure and gravity for different fluid density differences $\Delta\rho = \rho_w - \rho_o$. Fine-scale results are shown in solid lines and capillary-limit upscaling results are shown in dashed lines.

7 A More Complex 2D Example

As the homogeneous and layered models are highly simplified, we would also like to consider a more complex model and see if we can generalize our conclusions. To this end, we consider

model 1 of the 10th SPE Comparative Solution Project [5]. The model has $100 \times 1 \times 20$ cells and physical dimensions $762 \times 7.62 \times 15.24\,\mathrm{m}$. To avoid any upscaling effects of the wells, extra cells with homogeneous porosity and permeability are added to both sides of the domain and the wells are then placed in these padding cells. The wells are shown together with the permeability field in Fig. 15. The porosity is $\phi = 0.2$ everywhere. The fluids are incompressible, with densities $\rho_o = 700\,\mathrm{kg/m^3}$ and $\rho_w = 1025\,\mathrm{kg/m^3}$, and viscosities $\mu_o = 1\,\mathrm{cP}$ and $\mu_w = 0.5\,\mathrm{cP}$.

The original model does not contain any capillary pressure data. As we want consider the balance between capillary, viscous and gravitational forces, capillary pressure curves are added into the model. We will compute the capillary pressure from the same Leverett J-function as before. This J-function is given as tabulated data, and the resulting p_{cow} curve for a rock type with $\phi = 0.25$ and $K = 1000\,\mathrm{mD}$ can be seen in Fig. 4. Now, to obtain different curves, the domain is divided into R rock types based on the value of $\sqrt{K/\phi}$, which is a factor in the capillary pressure function (13). For each cell i, we first define the number $q_i = \log_{10}(\sqrt{K_i/\phi_i})$, then let $\Delta q = (\max(q_i) - \min(q_i))/R$, and finally define the bins

$$Q_r = \big[\min(q_i) + (r-1)\Delta q, \min(q_i) + r\Delta q\big],$$

for $r = 1, \ldots, R$. Then, we let cell i be of rock type r if $q_i \in Q_r$. The capillary pressure of each rock type is computed from (13) with permeability taken as the log-average and porosity as the average of all cells which is part of that rock type. We consider both the case of a single rock type ($R = 1$), and four different types ($R = 4$). The relative permeability is the same in the whole model, and are quadratic Corey-type curves with end-points $k_{ro}(0) = 1$ and $k_{rw}(1) = 0.5$.

Similar to what was done for the simpler models, we run the SPE10 model on the fine scale for a range of injection rates. Then, the model is upscaled both to a coarse grid with $25 \times 1 \times 1$ cells and one with $25 \times 1 \times 5$ cells, and the coarse models are then run for the same range of injection rates as the fine-scale model. Plots of the total oil production after 0.8 PV of water has been injected is shown in Fig. 16, both with a single capillary-pressure curve ($R = 1$), and with four different curves ($R = 4$).

The first observation we make is that for both models, the fine-scale simulations and the upscaled capillary-limit simulations converge to the low-rate limits, as anticipated. The fine-scale solution converges to the low-rate limit for a velocity about $10^{-5}\,\mathrm{m/day}$ and to the high-rate limit just below $10^{2}\,\mathrm{m/day}$. We note that both these convergence rates and also the shape of the curves are quite similar to the homogeneous 2D case with quadratic relative permeability and $\Delta\rho = 100\,\mathrm{kg/m^3}$, as shown in Fig. 6b, though the gravitational forces are now larger as $\Delta\rho = 325\,\mathrm{kg/m^3}$.

The difference between a 1D coarse model, and a coarse model with five cells in the vertical direction is clearly seen in Fig. 16. The 1D model does not include gravity in the coarse simulation. In particular, this causes the viscous-limit upscaled model to be independent of rate when plotted versus injected volume, as seen before. The 1D capillary-limit coarse model behaves similar as for the upscaled horizontally-layered model in Fig. 14a, following the fine-scale simulation from the low-rate limit and up to a point, before flattening out to a constant for higher velocities. Increasing the vertical coarse resolution to five cells, the match improves for both viscous- and capillary-limit coarse models. The saturation at water break through is compared for these models in Fig. 17, where we observe that the gravity tongue now is reproduced in the coarse models. Here we also see how the coarse capillary-limit results match the fine-scale better than the viscous-limit coarse results for the lower flow rate, while they are more similar for the higher flow rates.

8 Conclusion

In this article we have introduced a semi-analytical solution for low-rate (capillary and gravity dominated) flooding of a reservoir. Together with the high-rate (viscous dominated) limit, they give the limiting solutions for the rate-dependent flooding process. For all models considered in this article, the rate-dependent simulations converge to both the low-rate limit and the high-rate limit solutions, which indicates correctness of our semi-analytical low-rate solution. The rate-dependent simulations also show smooth transitions between these limits, though the transitions in general

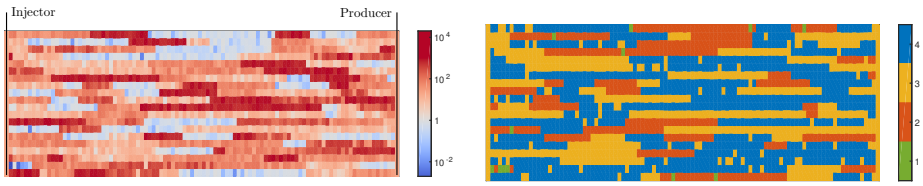

(a) Permeability field. (b) Rock types with $R = 4$ different types.

Figure 15: The SPE10 model 2.

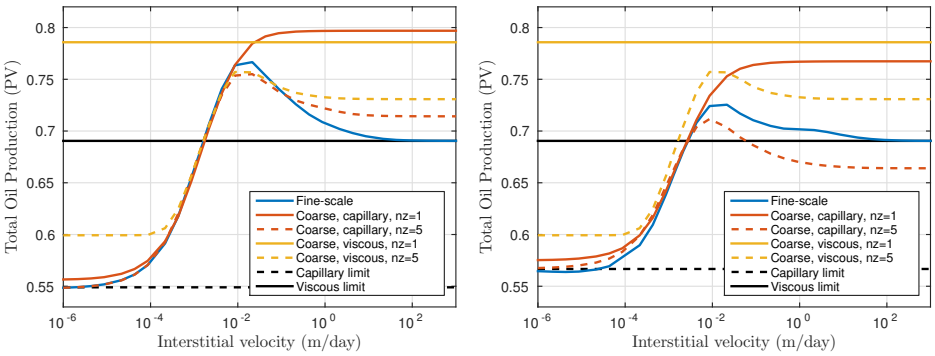

(a) A single p_{cow} curve ($R = 1$). (b) Four different p_{cow} curves ($R = 4$).

Figure 16: Total oil production after injection of 0.8 PV of water for the SPE10 model 2, both upscaled to coarse grid with nz = 1 cell in vertical direction and nz = 5 cells.

are neither trivial nor monotonic. Also, in several cases, the limiting solutions do not provide outer bounds for the rate-dependent solutions. It is seen in [28] that there is a non-monotonous transition between the upscaled relative permeability curves in the capillary-limit and viscous-limit, and here we observe that also the fine-scale simulation results have a similar non-monotonicity.

When considering a homogeneous 1D model, we only have driving forces in the flow direction. Our 1D model was clearly viscous dominated for realistic reservoir flow rates for model lengths down to 20 m. The cases considered indicate that for realistic flow parameters, viscosities, and flow-rates, we cannot assume capillary equilibrium in the flow direction. We also suggested a dimensionless capillary number to describe the ratio of viscous to capillary forces in the flow direction, which also accounts for the model length. For this homogeneous 1D model, the capillary number is reasonable.

To include the effect of gravity we used homogeneous 2D models. It was seen that gravity forces were important at realistic reservoir rates, but they were not dominant. For quadratic relative permeabilities, we observed a non-trivial transition from gravity-dominated to viscous-dominated flow. This was explained by gravity having a positive impact on residual oil behind the water front. It was also seen that when capillary forces were included, this positive impact of the gravity was reduced as the capillary forces were increased. For very large capillary forces relative to gravity, the flow became essentially one-dimensional, as capillary forces became dominant normal to the direction of flow.

The effect of capillary versus viscous forces for redistribution normal to the flow direction was investigated in horizontally layered models, where we disregarded gravity and used linear relative-permeability curves to remove viscous cross-flow. The force balance in the direction of flow was similar to the 1D homogeneous case, thus for realistic rates it was viscous dominated. Also, the force balance in the flow direction was not affected by the size of the layering, which is in contrast to the force balance normal to the flow direction. As lengths in the direction normal to flow typically are several orders of magnitude smaller than lengths in the direction of flow, we often have capillary

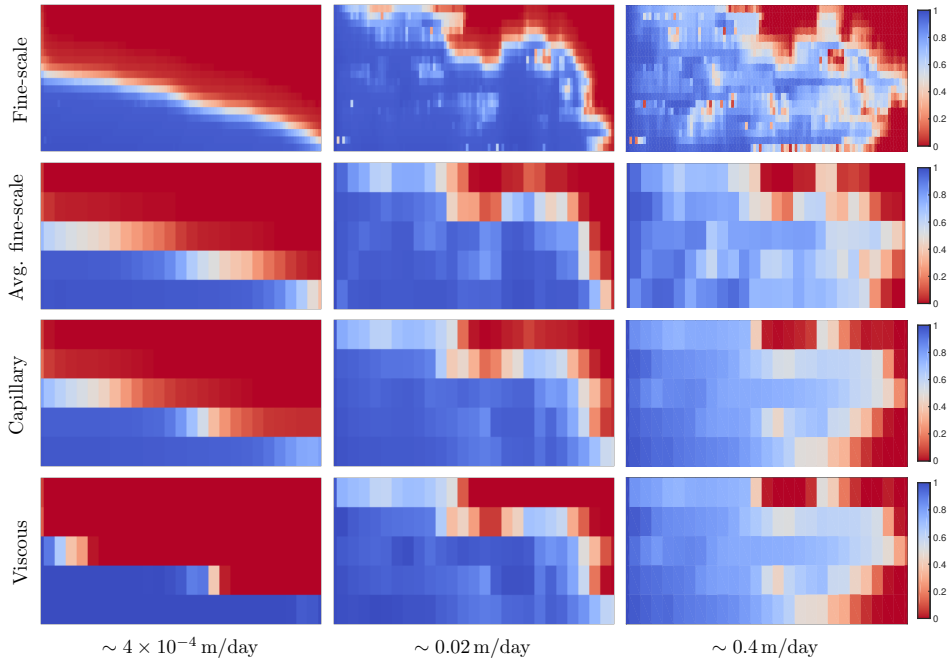

Figure 17: Water saturation for SPE10 at the point of water break through for different interstitial velocities and different models. The second row is the fine-scale results, averaged in each coarse block.

equilibrium normal to the flow direction, while viscous forces dominate the force balance along the direction of flow. At which thickness viscous forces start to influence the force balance normal to the flow will depend on different parameters, such as fluid properties and flow parameters.

When upscaling the horizontally layered models using capillary-limit upscaling, the coarse results reproduce the transition from the low-rate limit to vertical equilibrium. Thus capillary-limit upscaling has validity outside the low-rate limit solution. For higher flow rates, the solution equals the vertical-equilibrium solution. We observe that the capillary upscaling works well up to realistic flow rates for thin layers, when the fine-scale solutions are always at vertical equilibrium. Capillary-limit upscaling procedure thus seems fair for most situations when going from a lamina scale to a bed scale.

In the horizontally-layered case, viscous-limit upscaling failed to capture the flow dynamics because the assumption of constant fractional flow was not valid. Though not included in this paper, we have investigated the upscaling of a vertically-layered model. In this case, the fractional flow is constant in the direction normal to the flow, and we have seen that the viscous-limit upscaling reproduced the high-rate limit in this case.

In general, the viscous-limit upscaling can be applied in cases where the fractional flow is relatively constant within each coarse grid block, away from the water front. When this assumption of constant fractional flow holds is highly case-dependent, and is difficult to predict a priori for general models. For a horizontally-layered model, the viscous-limit upscaling would be accurate if all the layers are resolved by the coarse grid resolution, which is not the case for our examples herein. Similarly, if there is a relatively clear layered structure of a more complex model, then viscous-limit upscaling could be suitable if the coarse grid is chosen to resolve this layering.

We also considered a horizontally-layered model where we included gravity in addition to capillary forces. In this case, the capillary-limit upscaling was able to reproduce the transition from

the low-rate limit and up close to realistic flow rates, depending on the density difference. The capillary-limit upscaling is applicable for highest flow-rates when the gravitational forces are insignificant, i.e., upscaling to coarse blocks with limited vertical length.

Finally, we investigated the more complex SPE10, model 1, where we considered upscaling both to a one-dimensional coarse model and to a coarse model with five cells in vertical direction. Even with the heterogeneities of the model, similar results where seen as for the simpler models. The capillary-limit upscaling is able to reproduce the low-rate limit, as well as the transition up to flow-rates where capillary and gravity forces no longer dominate the distribution of fluids normal to the flow direction. It was also seen that we can improve the coarse models by increasing the vertical grid resolution, as the coarse model is then able to capture more of the gravity effects.

Acknowledgements

The research is funded by VISTA, which is a basic research program funded by Statoil and conducted in close collaboration with The Norwegian Academy of Science and Letters. The authors thank Knut-Andreas Lie and Vegard Kippe for helpful discussions.

References

[1] J. E. Aarnes, V. Kippe, K.-A. Lie, and A. B. Rustad. Modelling of multiscale structures in flow simulations for petroleum reservoirs. In *Geometric Modelling, Numerical Simulation, and Optimization*, pages 307–360. Springer, 2007.

[2] J. Bear. *Dynamics of Fluids in Porous Media*. Dover Publications, September 1988.

[3] A. L. Chen and A. C. Wood. Rate effects on water-oil relative permeability. In *Society of Core Analysis Conference Paper SCA 2001-19*, 2001.

[4] M. Christie. Flow in porous media - scale up of multiphase flow. *Curr. Opin. Colloid Interface Sci.*, 6(3):236–241, 2001.

[5] M. Christie and M. Blunt. Tenth SPE comparative solution project: A comparison of upscaling techniques. *SPE Reserv. Eval. Eng.*, 4(4):308–317, August 2001.

[6] M. Dale, S. Ekrann, J. Mykkeltveit, and G. Virnovsky. Effective relative permeabilities and capillary pressure for one-dimensional heterogeneous media. *Transp. Porous Media*, 26(3):229–260, March 1997.

[7] L. J. Durlofsky. Numerical calculation of equivalent grid block permeability tensors for heterogeneous porous media. *Water Resour. Res.*, 27(5):699–708, May 1991.

[8] L. J. Durlofsky. Upscaling and gridding of fine scale geological models for flow simulation. In *8th International Forum on Reservoir Simulation Iles Borromees, Stresa, Italy, June 20-24, 2005*, 2005.

[9] ECLIPSE 100 reservoir simulator, Schlumberger. `http://www.slb.com/eclipse/`.

[10] S. Ekrann and J. O. Aasen. Steady-state upscaling. *Transp. Porous Media*, 41(3):245–262, December 2000.

[11] S. Jonoud and M. D. Jackson. New criteria for the validity of steady-state upscaling. *Transp. Porous Media*, 71(1):53–73, January 2008.

[12] D. Kjonsvik, J. Doyle, T. Jacobsen, et al. The effects of sedimentary heterogeneities on production from a shallow marine reservoir - what really matters? In *SPE Annual Technical Conference and Exhibition*. Society of Petroleum Engineers, 1994.

[13] T. Kløv, P. Øren, J. Stensen, T. Lerdahl, L. Berge, S. Bakke, T. Boassen, G. Virnovsky, et al. Pore-to-field scale modeling of wag. In *SPE Annual Technical Conference and Exhibition*. Society of Petroleum Engineers, 2003.

[14] J. R. Kyte, D. Berry, et al. New pseudo functions to control numerical dispersion. *Society of Petroleum Engineers Journal*, 15(04):269–276, 1975.

[15] L. W. Lake. *Enhanced Oil Recovery*. Society of Petroleum Engineers, reprint 2010 edition, 1989.

[16] K.-A. Lie, S. Krogstad, I. Ligaarden, J. Natvig, H. Nilsen, and B. Skaflestad. Open-source MATLAB implementation of consistent discretisations on complex grids. *Comput. Geosci.*, 16:297–322, 2012.

[17] A. Lohne, G. A. Virnovsky, L. J. Durlofsky, et al. Two-stage upscaling of two-phase flow: from core to simulation scale. *SPE Journal*, 11(03):304–316, 2006.

[18] The MATLAB Reservoir Simulation Toolbox, MRST 2015a, May 2015. `http://www.sintef.no/MRST/`.

[19] L. H. Odsæter, C. F. Berg, and A. B. Rustad. Rate dependency in steady-state upscaling. *Transport in Porous Media*, pages 1–25, 2015.

[20] D. W. Peaceman. Interpretation of well-block pressures in numerical reservoir simulation with nonsquare grid blocks and anisotropic permeability. *SPE J.*, 23(3):531–543, June 1983.

[21] G. Pickup, P. Ringrose, and A. Sharif. Steady-state upscaling: From lamina-scale to full-field model. *SPE J.*, 5(2):208–217, June 2000.

[22] L. A. Rapoport. Scaling laws for use in design and operation of water-oil flow models. *Petroleum Transactions*, 204:143–150, 1955.

[23] P. S. Ringrose, K. S. Sorbie, P. W. M. Corbett, and J. L. Jensen. Immiscible flow behaviour in laminated and cross-bedded sandstones. *J. Petrol. Sci. Eng.*, 9(2):103–124, April 1993.

[24] A. B. Rustad, T. G. Theting, and R. J. Held. Pore space estimation, up scaling and uncertainty modeling for multiphase properties. In *SPE Symposium on Improved Oil Recovery, 20-23 April 2008, Tulsa, Oklahoma, USA*, 2008.

[25] M. Shook, D. Li, and L. W. Lake. Scaling immiscible flow through permeable media by inspectional analysis. *In Situ*, 16(4):311–349, January 1992.

[26] E. H. Smith. The influence of small-scale heterogeneity on average relative permeability. In *Reservoir Characterization II*, pages 52–76. Academic Press, Inc., 1991.

[27] K. D. Stephen, G. E. Pickup, and K. S. Sorbie. The local analysis of changing force balances in immiscible incompressible two-phase flow. *Transp. Porous Media*, 45(1):63–88, October 2001.

[28] G. A. Virnovsky, H. A. Friis, and A. Lohne. A steady-state upscaling approach for immiscible two-phase flow. *Transp. Porous Media*, 54(2):167–192, February 2004.

[29] Y. C. Yortsos. A theoretical analysis of vertical flow equilibrium. *Transp. Porous Media*, 18(2):107, February 1995.

[30] P. Zhang, G. E. Pickup, M. A. Christie, et al. A new method for accurate and practical upscaling in highly heterogeneous reservoir models. In *International Oil & Gas Conference and Exhibition in China*. Society of Petroleum Engineers, 2006.

[31] D. Zhou, F. Fayers, F. Orr Jr, et al. Scaling of multiphase flow in simple heterogeneous porous media. *SPE Reservoir Engineering*, 12(03):173–178, 1997.

Paper II

Comparison of Two-Phase Upscaling Methods on Field Models

Sindre Tonning Hilden and Carl Fredrik Berg

Submitted

Comparison of Two-Phase Upscaling Methods on Field Models

Sindre T. Hilden Carl Fredrik Berg

Preprint, March 29, 2016

Abstract

In this article we consider two-phase flow, where we investigate and compare different one-phase and two-phase upscaling methods. For single phase upscaling we apply flow-based pressure upscaling, harmonic-arithmetic and arithmetic-harmonic mean, as well as a global transmissibility upscaling. For the two-phase upscaling, we consider both steady-state methods and simpler averaging techniques. The upscaling is performed on two different realistic field-scale models, in addition to a simplified layered model. To assess how well the different methods perform, we run two-phase flooding simulations both on the original fine-scale and the upscaled coarse model, and compared the results.

Motivated by differences in the balance between gravity, capillary and viscous forces perpendicular and along the flow direction, two different steady-state methods are proposed which combine ideas from the capillary-limit and the viscous-limit upscaling methods. These methods are included when comparing upscaled model simulation results.

The simulation examples show that if the variation in the fine-scale relative permeability curves are not too large in the original model, then the choice of one-phase upscaling method has a larger impact on the solution than the two-phase method. Local flow-based permeability upscaling and global transmissibility upscaling give better results than averaging techniques, while the difference between the two-phase upscaling methods are almost negligible. On the other hand, if the relative permeability varies significantly in the fine-scale model, then the capillary-limit upscaling and the two novel methods give better results than the viscous-limit upscaling and simpler averaging techniques. In some cases the two novel methods give a slight improvement over the capillary-limit method, however the capillary-limit method partly captures the effect of varying flow rates.

1 Introduction

There exist a wide range of different upscaling methods for one-phase and two-phase flow [14, 1, 4]. Even though upscaling has been studied for decades, the problem of choosing an appropriate upscaling technique remains a difficult task, and it is highly case dependent. In this article, we consider the water flooding of a reservoir, and investigate and compare different one-phase and two-phase upscaling methods applied to field-scale models.

One-phase upscaling methods can be divided into local, local-global and global methods [6]. We mainly focus on local methods, where we consider both flow-based steady-state methods, and simpler averages such as the harmonic-arithmetic and arithmetic-harmonic mean [14]. For one example considered herein, we include global transmissibility upscaling for comparison [9]. The flow-based upscaling methods require the computation of pressure solutions, and the upscaling will depend on the choice of boundary conditions, which can be e.g. Dirichlet or periodic boundaries. Averaging methods are faster to compute and are widely used because of their simplicity. Global methods require one or more pressure solutions of the whole domain, which is computationally more demanding than the other methods, but at the same time include more information into the upscaling.

As for one-phase methods, also two-phase methods can roughly be grouped into local, local-global and global methods. We consider local methods, both flow-based steady-state methods,

and simpler averaging techniques. There has been a string of articles discussing the mathematical background of steady-state upscaling, see e.g., [20, 3, 5], and these methods have been applied both to small-scale models [8, 16], and recently also to larger scale models [12], as part of upscaling workflows. The water flooding of a reservoir is a transient process. However, the flow at smaller scales, e.g., on the core-scale, can often be approximated as steady-state because there is small saturation changes relative to the volume of fluids flowing through the rock [5]. With larger scales, the steady-state assumption becomes decreasingly valid, and steady-state upscaling is therefore mainly used on a relatively small scale, e.g., from a lamina scale (mm to cm) to a bed scale (cm to m) [15].

In a previous paper [7], the authors investigated the balance of viscous, capillary and gravity forces during the water flooding of a reservoir at different flow velocities. One of the main conclusions from that work is that for realistic flow-rates in a reservoir model, one may have a situation where the capillary forces dominate perpendicular to the flow direction, while viscous forces dominate in the flow direction. This directional-dependent force balance suggests an upscaling strategy where one applies a capillary-limit assumption perpendicular to the flow direction, and a viscous-limit assumption in the flow direction. In this paper, we investigate such an upscaling methodology and suggest two different upscaling methods built on this principle.

As the steady-state methods require a series of pressure-solutions in each coarse block of the domain, there is a significant cost of computing the upscaling. In addition, the upscaled model has a unique set of flow parameters for each grid cell, which increases the complexity of the model. To defend the use of such upscaling methods on a field-scale model, the upscaled models should perform notably better in terms of improved coarse-scale simulation results, compared to simpler averaging techniques.

In this article, we apply the different one- and two-phase upscaling methods on two different realistic field-scale models and on a simple layered model. To assess how well the upscaling methods work, we run two-phase flooding simulations both on the original fine-scale grid and on the upscaled coarse grid, and compare the results.

The upscaling and plotting in this article are performed using the Matlab Reservoir Simulation Toolbox (MRST) [9, 10, 19], which is a powerful open-source toolbox, especially useful for rapid prototyping. The simulations are run using the commercially available reservoir simulator Eclipse 100 [18].

2 Upscaling

The general concept of upscaling is illustrated in Fig. 1, where each grid block of fine-scale cells is upscaled to a single coarse cell. We present below the single- and two-phase local methods we consider herein. These methods, including the capillary- and viscous-limiting cases, are described in several papers, see e.g., [3, 5, 1, 13]. We also present two different two-stage methods, which to our knowledge are novel.

In the following, we consider a single grid block Ω, which is a subsection of the fine grid consisting of N cells, that is to be upscaled to a single coarse grid cell Ω^C, as shown in Fig. 1. Let superscript '$*$' denote an upscaled value (which may be a scalar or a tensor), such that e.g., $\boldsymbol{K}^*$ denotes the upscaled value of the absolute permeability $\boldsymbol{K}$.

2.1 Governing Equations

We start of by introducing the underlying governing equations. Consider a two-phase flow, which for simplicity of presentation is assumed incompressible. The two phases will be denoted oil and water, represented by subscripts o and w, respectively. The continuity equations for the two phases are

$$\phi \frac{\partial s_\alpha}{\partial t} + \nabla \cdot \vec{v}_\alpha = q_\alpha, \qquad \alpha \in \{o, w\},$$

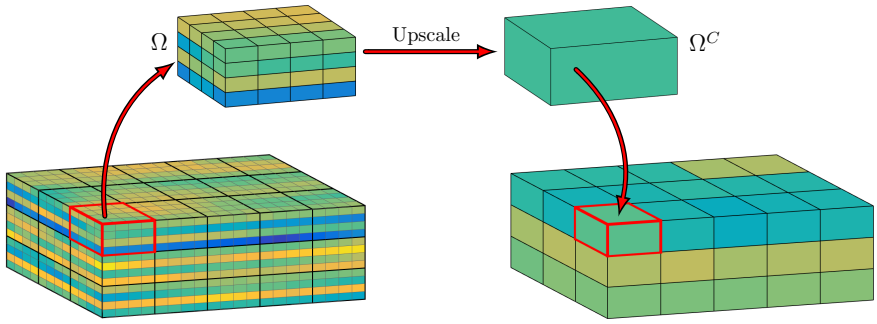

Figure 1: Illustration of upscaling a fine grid to a coarse grid. The fine grid is divided into grid blocks, where each block is upscaled in turn to a single coarse cell.

where ϕ is the porosity, s_α is the phase saturation and q_α is a source term. The phase velocities $\vec{v}_\alpha$ are given by Darcy's law:

$$\vec{v}_\alpha = -\frac{k_{r\alpha}}{\mu_\alpha}\boldsymbol{K}\left(\nabla p_\alpha - \rho_\alpha g \nabla z\right), \qquad \alpha \in \{o, w\},$$

where $\boldsymbol{K}$ is the absolute permeability, g is gravity, z is height above a given datum, and p_α, ρ_α, μ_α and $k_{r\alpha}$ are the phase pressure, density, viscosity and relative permeability, respectively. In addition, we have the closing relation

$$s_w + s_o = 1,$$

and the capillary pressure equation

$$p_{\text{cow}}(s_w) = p_o - p_w.$$

2.2 Single Phase Upscaling

There are a number of different methods for upscaling absolute permeability (see e.g., [14] for an overview of many such methods). Herein, we will consider simple local averaging and flow-based upscaling of single phase flow. These methods are presented in the following.

2.2.1 Averages

One of the simpler forms of permeability upscaling is to perform a simple power average. Denote the arithmetic mean in ξ-direction for μ_a^ξ, and similarly denote the harmonic mean for μ_h^ξ. By combining these two averages, one can obtain the *harmonic-arithmetic average*, where the upscaled permeability is $\boldsymbol{K}^* = \text{diag}(K^*_{xx}, K^*_{yy}, K^*_{zz})$, with the diagonal entries given by

$$K^*_{xx} = \mu_a^z(\mu_a^y(\mu_h^x)), \quad K^*_{yy} = \mu_a^x(\mu_a^z(\mu_h^y)), \quad K^*_{zz} = \mu_a^y(\mu_a^x(\mu_h^z)).$$

Similarly, by reversing the order, we obtain the *arithmetic-harmonic average*, where the diagonal entries of the upscaled permeability are given by

$$K^*_{xx} = \mu_h^x(\mu_a^y(\mu_a^z)), \quad K^*_{yy} = \mu_h^y(\mu_a^z(\mu_a^x)), \quad K^*_{zz} = \mu_h^z(\mu_a^x(\mu_a^y)).$$

These two averages are of special interest, because they create outer bounds for the coarse scale permeability, where e.g., $\mu_h^x(\mu_a^y(\mu_a^z)) \leq K^*_{xx} \leq \mu_a^z(\mu_a^y(\mu_h^x))$.

2.2.2 Local Flow-Based Upscaling

In a local flow-based method, the pressure equation $\nabla \cdot (\boldsymbol{K} \nabla p) = q$ is solved on each grid block for some set of boundary conditions. The upscaling is highly dependent on the choice of boundary conditions. Herein, we only consider Dirichlet boundaries in the flow direction with no-flow restriction on the other boundaries. Even though periodic boundaries can produce more accurate upscaling results, they will also give full permeability tensors. As we will perform two-phase upscaling, it is easier to deal with diagonal upscaled relative-permeabilities than full tensors in the coarse scale simulations.

When the pressure equation is solved, the average flux in the direction of flow is computed, which we denote $\bar{v}_d$. The upscaled permeability in direction d is then given by

$$\boldsymbol{K}^*_{dd} = \frac{L_d}{\Delta p} \bar{v}_d,$$

where L_d is a representative distance between the inflow and outflow boundaries. The upscaled permeability is a diagonal tensor for each coarse grid block, given by $\boldsymbol{K}^* = \mathrm{diag}(K^*_{xx}, K^*_{yy}, K^*_{zz})$.

2.3 Two-Phase Upscaling Methods

It is well known that two-phase upscaling is rate dependent, with capillary and gravity forces dominating for small grid scales and at low flow rates, while viscous forces dominate for large grid scales and at high rates [5]. Herein, we consider the steady-state limit upscaling methods, with the capillary-limit assuming low rates and viscous-limit assuming high rates. We wish to investigate how well these two steady-state limits perform in practice for realistic field models, and also how they compare to simpler averaging methods. The steady-state limit methods are presented below [1, 13, 17].

Layered models were considered in [7], where the authors investigated the force balance during a water flooding for different flow velocities. For realistic rates on the field scale, the flow was seen to be at capillary-equilibrium in the vertical direction, while viscous forces dominated the horizontal flow. Based on these observations, we suggest two different upscaling methods below that attempt to capture this directionally dependent force balance. Both methods perform the upscaling calculations in two stages, where one stage assumes capillary equilibrium in the vertical direction, and the other assumes viscous equilibrium in the horizontal direction. We will refer to these methods as *two-stage methods*.

2.3.1 Capillary-Limit Upscaling

The first step of a steady-state two-phase upscaling is to calculate the saturation distribution $\hat{s}_w$ at steady-state in the grid block Ω. For the *capillary-limit* (or *diminishing rate limit*), the capillary and gravity forces are assumed to be in equilibrium. Recall that there are N fine cells in the grid block Ω, and let superscript i denote the value of some property in cell i. For a given value $\hat{p}_{\mathrm{cow}}$ of the capillary pressure, the saturation distribution is found by solving the N equations

$$p^i_{\mathrm{cow}}(s^i_w) = \hat{p}_{\mathrm{cow}} - \Delta \rho g z^i, \qquad i \in [1, \ldots, N], \tag{1}$$

where the value z^i is the height of the centroid of cell i relative to the block centroid. Given the saturation distribution $\hat{s}_w = \{s^i_w\}$, the phase permeabilities are computed as $\widetilde{\boldsymbol{K}}_\alpha = k_{r\alpha}(\hat{s}_w)\boldsymbol{K}$, and a single-phase upscaling is applied to obtain upscaled (effective) phase permeabilities $\widetilde{\boldsymbol{K}}^*_\alpha$. The upscaled relative permeabilities are then computed as

$$k^*_{r\alpha}(s^*_w) = (\boldsymbol{K}^*)^{-1} \widetilde{\boldsymbol{K}}^*_\alpha, \tag{2}$$

where the upscaled saturation is given by

$$s^*_w = \frac{\sum_{i=1}^N s^i_w \phi^i V^i}{\sum_{i=1}^N \phi^i V^i}.$$

Also, the upscaled capillary pressure is given by $p^*_{\text{cow}}(s^*_w) = \hat{p}_{\text{cow}}$.

As we herein apply Dirichlet boundary conditions to perform the one-phase upscaling, the upscaled relative permeabilities also become a diagonal tensor. This process of upscaling relative permeability and capillary pressure is repeated for different values of $\hat{p}_{\text{cow}}$ to obtain full upscaled curves.

2.3.2 Viscous-Limit Upscaling

The *viscous-limit* (or *high rate limit*) assumes that viscous forces dominate. Assuming steady-state, the time derivative of the saturation goes to zero, and then the fractional flow formulation of the conservation equation reduces to (see e.g., [7] for details)

$$\nabla f_w \cdot \vec{v} = 0, \tag{3}$$

where f_w is the fractional flow of water. Thus, the fractional flow is constant along streamlines, and the solution to (3) depends on the distribution of fractional flow over the inlet face of the domain Ω. In particular, this means the solution is not unique. A common choice is to assume a constant fractional flow on the whole inlet boundary, resulting in constant fractional flow throughout the entire domain [3]. With this assumption, the saturation distribution for each fractional flow value $\hat{f}_w$ is obtained by inverting the fractional flow function f_w, such that $\hat{s}_w = f_w^{-1}(\hat{f}_w)$. Similar to the capillary-limit, once the saturation distribution is found, we apply a single-phase upscaling for the phase permeabilities $\widetilde{\boldsymbol{K}}_\alpha = k_{r\alpha}(\hat{s}_w)\boldsymbol{K}$ to obtain upscaled (effective) phase permeabilities, and then the upscaled relative permeabilities are computed from (2). This process is repeated for different fractional flow values $\hat{f}_w$ to obtain upscaled relative permeabilities for different values of the corresponding average saturation. The upscaled capillary pressure is set to zero for the viscous-limit method.

2.3.3 Two-Stage Upscaling

This is the first of the two-stage methods we present. The method performs upscaling in two stages, and is therefore referred to as the *two-stage upscaling method*. The steps involved in the relative permeability upscaling is illustrated in Fig. 2, and these steps are used to explain the two-stage upscaling as follows;

1. Consider a block Ω of fine cells that is to be upscaled.
2. Divide the block into slices normal to the chosen direction $d \in \{x, y, z\}$.
3. Upscale each slice by using capillary-limit upscaling.
4. Merge the upscaled slices back into a single intermediate grid block.
5. Upscale this intermediate block into a single cell Ω^C using the viscous-limit upscaling method.

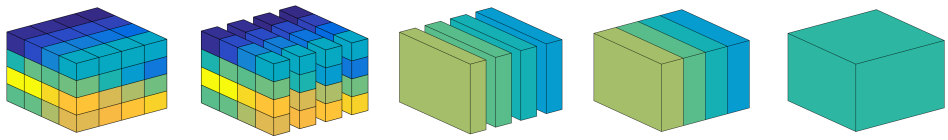

Figure 2: The steps of the proposed two-stage upscaling method, showing the permeability field of each step.

Viscous-limit upscaling is performed at the second stage, which sets the capillary pressure to zero, and consequently the coarse model does not have any capillary pressure.

As capillary-limit upscaling is performed for each of the intermediate slices in addition to the final viscous-limit upscaling, there is an increase in the computational cost of the two-stage upscaling compared to the capillary- and viscous-limit methods. The one-phase pressure equation needs to be solved multiple times, though on a smaller domain.

2.3.4 Two-Stage Distribution

We also present a second two-stage method using the same principle of assuming capillary equilibrium in the vertical direction and viscous equilibrium in the horizontal direction, but this method applies the assumptions to the saturation distribution instead of using the limit upscaling methods. This *two-stage distribution method* computes the water saturation for the grid block, and then performs a single relative permeability upscaling for each upscaled saturation value. The steps in Fig. 3 are used to explain this methods as follows;

1. For some given value of the upscaled water saturation s_w^*, compute the capillary-limit saturation distribution from Equation (1).
2. Divide the block into horizontal slices.
3. For each horizontal slice, compute the viscous-limit distribution, assuming the fractional flow is constant within the slice, while keeping the same upscaled saturation in the slice as in step 2.
4. Merge the slices to obtain the saturation distribution for the whole block. With this distribution, upscale the relative permeability using Equation (2).

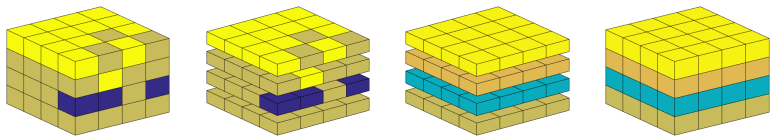

Figure 3: The steps of the proposed two-stage distribution computation, showing the water saturation of each step.

Viscous-limit distribution is assumed at the second stage of this method, where the capillary pressure is neglected, and we therefore also assume that the resulting coarse will not contain any capillary pressure. In contrast to the two-stage upscaling method in the previous section, this method do not need any additional one-phase pressure solutions, compared to the capillary- and viscous-limit method.

2.3.5 Pore-Volume Averaging

A simple alternative to the steady-state upscaling methods is to perform a pore-volume averaging of both the relative permeability curves and the capillary pressure. This is fast to compute relative to the steady-state methods as there is no need for the solution of a pressure equation. We expect the steady-state methods to produce at least as good results as this simple averaging, and we will therefore include the pore-volume averaging in the numerical examples below for comparison.

Define first the pore-volume average of a cell property x in grid block Ω as

$$\Phi(x) = \frac{\sum_{i=1}^{N} x^i \phi^i V^i}{\sum_{i=1}^{N} \phi^i V^i}, \tag{4}$$

where the sums go over all cells i in Ω, and ϕ^i is the porosity and V^i is the volume of cell i. Each grid cell may have different values for the irreducible water saturation s_{wir} and the residual oil

saturation s_{or}. The saturation distribution in Ω is scaled with these values, such that the water saturation in cell i is given by

$$s_w^i = s_{wir}^i + s(1 - s_{wir}^i - s_{or}^i),$$

for $s \in [0, 1]$. When the saturation distribution $\hat{s}_w = \{s_w^i\}$ is found, we compute the pore-volume averages as follows; $s_w^* = \Phi(\hat{s}_w)$, $k_{rw}^* = \Phi(k_{rw}(\hat{s}_w))$, $k_{ro}^* = \Phi(k_{ro}(\hat{s}_w))$ and $p_{\text{cow}}^* = \Phi(p_{\text{cow}}(\hat{s}_w))$.

2.3.6 Endpoint-Scaling

This method assumes that the relative permeability and capillary pressure curves for all the upscaled blocks are scaled versions of the same curves, where the end-points, the maximum water relative permeability and the maximum capillary pressure value changes. Most reservoir simulators has functionality for implementing such endpoint-scaled flow functions. Using the pore-volume average function $\Phi(x)$ as defined in (4), we compute for each block Ω the values

$$s_{wir}^* = \Phi(s_{wir}), \quad 1 - s_{or}^* = 1 - \Phi(s_{or}), \quad p_{cow,\max}^* = \Phi(\max(p_{\text{cow}})).$$

In addition, an upscaling of the maximum point of the water relative permeability curve is computed as in (2), such that

$$k_{rw,\max}^* = k_{rw}^*(1 - s_{or}^*) = (\boldsymbol{K}^*)^{-1}\big(k_{rw}(1 - s_{or})\boldsymbol{K}\big)^*. \tag{5}$$

Then, for the *entire model*, the pore-volume average of the relative permeability curves and the capillary-pressure curve are computed, which we denote $\hat{k}_{rw}$, $\hat{k}_{ro}$ and $\hat{p}_{cow}$. These average curves are then scaled by the block-wise values, such that for block Ω, the upscaled curves are given by

$$k_{ro}^*(s_w^*) = \hat{k}_{ro}(\hat{s}_w), \qquad k_{rw}^*(s_w^*) = \hat{k}_{rw}(\hat{s}_w)\frac{k_{rw,\max}^*}{\max(\hat{k}_{rw})},$$

$$p_{cow}^*(s_w^*) = \hat{p}_{cow}(\hat{s}_w)\frac{p_{cow,\max}^*}{\max(\hat{p}_{cow})}.$$

Assuming the domain of the pore-volume average functions are scaled to $[0, 1]$ for simplicity, the saturation $\hat{s}_w$ is given by

$$\hat{s}_w = \frac{s_w^* - s_{wir}^*}{1 - s_{wir}^* - s_{or}^*}.$$

2.3.7 Pore-Volume Averaging with Endpoint-Scaling

This is a combination of the two previous methods, where all curves are computed as in the pore-volume averaging method, but in addition, we scale the water relative permeability curves using the *upscaled* value $k_{rw,\max}^*$ from (5).

Note that the saturation endpoints s_{wir}^* and s_{or}^* are equal for all the upscaling methods considered above, while the water relative permeability endpoint $k_{rw,\max}^*$ is equal for all methods except for the pore-volume averaging. Thus comparing the upscaling methods with the endpoint-scaling or pore-volume averaging with endpoint-scaling gives an indication of the effect of the curve shape of the relative permeability curves.

3 Numerical Examples

For the numerical examples presented below, we run the different combinations of the one and two-phase upscaling methods presented above. To sum up, we consider the following upscaling methods:

One-phase Methods

1) Harmonic-arithmetic mean
2) Arithmetic-harmonic mean
3) Local flow-based pressure upscaling

Two-phase Methods

1) Steady-state viscous-limit
2) Steady-state capillary-limit
3) Steady-state two-stage upscaling
4) Steady-state two-stage distribution
5) Pore-volume average
6) End-point scaling
7) Pore-volume average with end-point scaling

For each numerical model we consider below, the model is upscaled using the different combinations of the one- and two-phase methods, and then the corresponding coarse-scale simulations are run. As a measure of the success of each combination of upscaling methods, the coarse-scale simulation results are compared to the fine-scale solution, which in this context is considered the true solution. To be able to consistently discuss the differences between the methods, we define an error norm as follows. Consider a well property, either oil or water production rate, or injection bottom hole pressure. Let Q_w be the vector of the fine-scale solution of this property for well w at a given set of discrete times, and let q_w be the corresponding coarse-scale solution vector obtained at the same discrete times. We then define the error E in the coarse-scale value to be

$$E = \sum_w \frac{\|Q_w - q_w\|_2}{\|Q_w\|_2}, \tag{6}$$

where the sum goes over all wells of the same type, either all injectors or all producers, depending on the property.

3.1 Layered Model

Consider a two-dimensional horizontally layered model as illustrated in Fig. 4. The model has physical dimensions $2000 \times 5 \times 20\,\mathrm{m}$ and a grid size of $200 \times 1 \times 20$ cells. The layers alternate between a higher permeable rock type 1, and a lower permeable rock type 2. Starting from the top with type 1, there are 5 layers of each rock type. The permeabilities are given by $K^1 = 1000\,\mathrm{mD}$

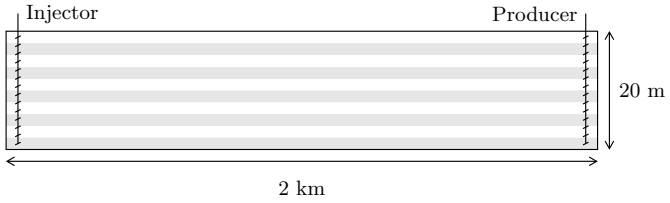

Figure 4: Sketch of the layered model.

and $K^2 = 10\,\mathrm{mD}$, and are homogeneous and isotropic within each rock type. The porosities are $\phi^1 = 0.3$ and $\phi^2 = 0.1$, and the relative permeabilities are given by

$$k^1_{rw} = 0.6(\widetilde{s}_w/2)^2, \quad k^2_{rw} = 0.4(\widetilde{s}_w/2)^{2.2}, \quad k^1_{ro} = (1-\widetilde{s}_w)^2, \quad k^2_{ro} = (1-\widetilde{s}_w)^{2.2},$$

where the scaled saturation is given by $\widetilde{s}_w(s_w) = (s_w - s_{wir})/(1 - s_{wir} - s_{or})$, and the irreducible water saturation is $s_{wir} = 0.1$ and the residual oil saturation is $s_{or} = 0.1$. The viscosities for oil and water are set to $\mu_o = 1.5\,\mathrm{cP}$ and $\mu_w = 0.5\,\mathrm{cP}$. The capillary pressure curves are computed as

$$p_{\mathrm{cow}}(s_w) = J(s_w)\gamma\cos\theta\sqrt{\phi/K}, \tag{7}$$

where $J(s_w)$ is a Leverett J-function, γ is the surface tension, θ is the contact angle between water and oil, ϕ is porosity and K is permeability. For this example, we use $\gamma = 22\,\text{dyn/cm}$ and $\theta = 45°$, and the J-function is given by tabulated data.

An injection well is included at the west end of the model, and a producer is included at the east end. The domain is initialized with water saturation $s_w = s_{wir}$ everywhere. Then, water is injected at a constant rate until a total of 1.5 PV (pore-volumes) of water have been injected. The rate is set such that the flow rate through the model is about 1 m/day.

The model is upscaled to a coarse grid of size $25 \times 1 \times 5$, meaning that each coarse block contains 32 fine cells. For the layered model, the three one-phase methods we consider, local pressure solution, harmonic-arithmetic average and arithmetic-harmonic average, all give the same upscaling. Thus, this example will not show any difference between the one-phase upscaling, and so we only discuss the different two-phase methods in the following.

The upscaled relative permeability curves are shown in Fig. 5a. Only four of the methods are shown, but the two-stage upscaling and the two-stage distribution method both give the same upscaled curves as the capillary-limit. For the two-stage upscaling, this is because the first stage gives the same capillary-limit upscaled curve in all slices and the second stage does not change the curves. For the two-stage distribution method, the second stage do not alter the saturation distribution, and it is thus equal to the capillary-limit distribution. Also, the end-point scaling methods give the same curves, and only one of them is shown in Fig. 5a. We observe that the viscous-limit and the end-point scaling methods give upscaled curves which are quite similar to the high-permeable rock input curves.

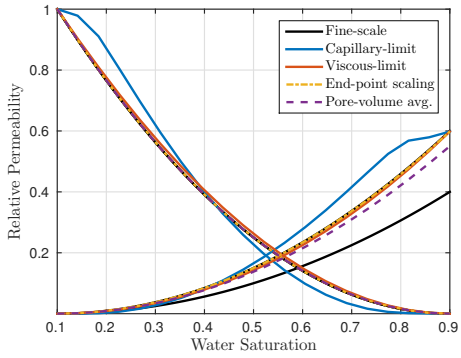

(a) Relative permeabilities.

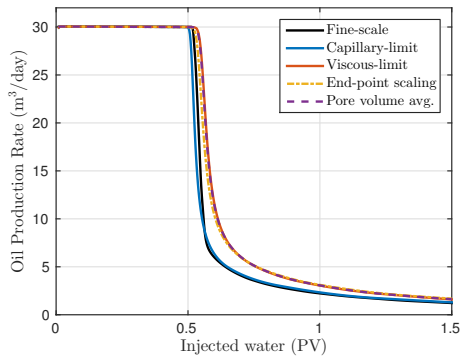

(b) Oil production rates.

Figure 5: Results for the layered model. Left: fine-scale and upscaled relative permeability curves. Right: oil production rate from the corresponding simulations.

Simulations are run using the different upscaled models, and the oil production is shown in Fig. 5b for the same methods as plotted in Fig. 5a. The capillary-limit method (and also the two-stage methods, which are not shown) give a better match with the fine-scale results than the other methods. Even though the flow is not in capillary equilibrium in the flow direction across the water front, the flow is close to capillary equilibrium within each grid block before and after the front. Thus, the capillary-limit assumption works well for the layered model. The viscous-limit upscaling matches the fine-scale results poorly. Because the injected water mainly flows in the high permeable layers on the fine scale, the flow is not close to constant fractional flow in the vertical direction, and so the viscous-limit assumption fails. Note that the viscous-limit method will also fail in the absence of capillary pressure in the model.

To better compare the methods and to quantify the match with the fine-scale solution, the error as defined in (6) is plotted in Fig. 6 both for the oil production rate and the injector BHP. Both these plots show similar results, where the capillary-limit and the two different two-stage methods give the smallest error.

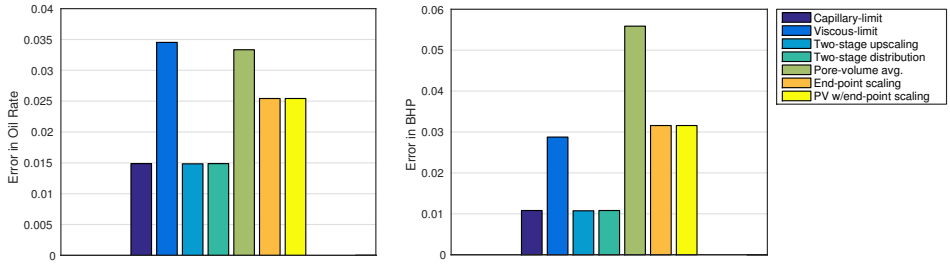

Figure 6: Error in oil rate (left) and injector BHP (right) for the different two-phase upscaling methods in the layered model.

3.2 Realistic Model 1: SPE10

The first realistic model we consider is Model 2 of the 10th SPE Comparative Solution Project [2]. This project's aim is to consider upgridding and upscaling methods, and Model 2 was chosen as a model which is computationally heavy to run on the fine scale. The model has physical size $1200 \times 2200 \times 170\,\mathrm{ft}^3$ and grid dimensions $60 \times 220 \times 85$, resulting in just above 1.1 million cells. The permeability field and the well locations are shown in Fig. 7. The injector has a constant injection rate of 5000 stb/day, while all four producers operate at a constant pressure of 4000 psi. There is a single set of Corey-type relative permeability curves in the model and the fluids have low compressibility. For more details of the model, see reference [2] and also the project webpage[1].

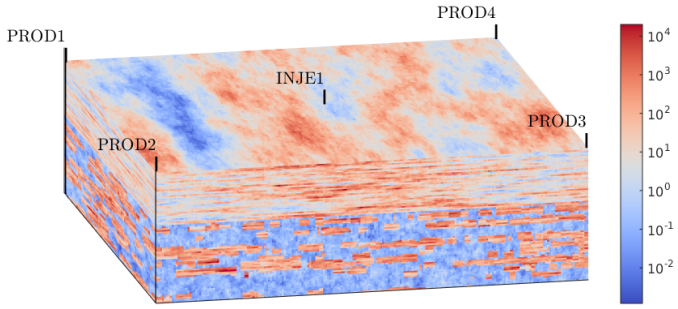

Figure 7: Horizontal permeability field in milli Darcy of the SPE10 model.

The SPE10 model as presented in [2] does not contain capillary-pressure data. As we herein are interested in the force balance between capillary and viscous forces, we create capillary curves that we introduce into the model. This is done by using a Leverett J-function, which we analytically construct as

$$J = \alpha \left(\frac{1}{(s_w - s_{wir} + \delta)^2} - \frac{1}{(1 - s_{or} - s_w + \delta)^2} \right). \tag{8}$$

The δ parameter is added to create a capping of the curves. If $\delta = 0$, the J-function will go to infinity at the edges. However, if $\delta > 0$, the curves are capped and J only takes on finite values. We make the choice of $\delta = 0.05$, and set the multiplier to $\alpha = 0.01$.

Instead of having a unique capillary pressure curve for each cell, we divide the cells into $R = 10$ regions based on the rock properties. We first define, for each cell i, the number $q_i = \log_{10}(\sqrt{K_i/\phi_i})$, which is chosen because $\sqrt{K/\phi}$ appears in the capillary pressure scaling,

[1] `http://www.spe.org/csp`

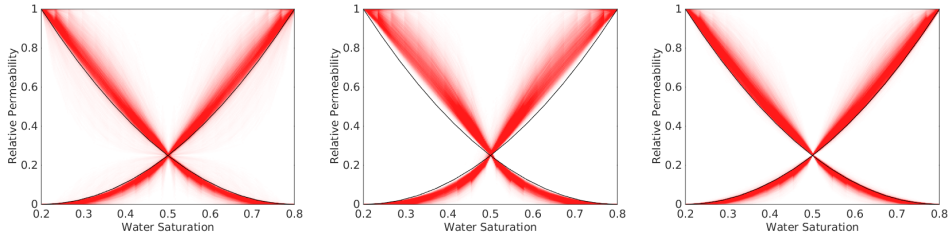

(a) Capillary-limit (b) Two-stage upscaling (c) Two-stage dist.

Figure 8: Upscaled relative permeabilities for all the 8976 coarse blocks of the SPE10 model shown as clouds, where stronger color indicates higher occurrence of curves. The input curves are shown in black on top.

as seen in (7), and the permeability is more evenly distributed on the log-scale. With this definition, we divide the span of q_i into evenly sized sets, where we say that cell i belongs to set r if $Q_{r-1} \leq q_i < Q_r$, where

$$Q_r = \begin{cases} \min_i q_i + (r/R)(\max_i q_i - \min_i q_i), & r \in [0, R-1], \\ \infty, & r = R. \end{cases}$$

For each set r, the capillary pressure is computed from (7) using average porosity and log-scale average permeability of that region. Note that even though the capillary pressure varies throughout the domain, the relative permeabilities are unchanged and are thus equal everywhere.

The model is then upscaled to a coarse grid of size $12 \times 44 \times 17$, meaning that each coarse block contains $5 \times 5 \times 5$ fine cells. The model is upscaled using the different combinations of the one- and two-phase methods as summarized at the beginning of Section 3. The upscaled relative permeability curves are shown for the capillary-limit and the two-stage methods in Fig. 8. Because there are only a single pair of input relative permeability curves, the remaining four methods give back the original fine-scale curves.

The oil production and water cut are shown for the first production well in Fig. 9. To improve the readability of the plot we have only included three of the upscaling methods. The oil production rate shows a relatively good match between the upscaled models and the fine-scale model. Water breakthrough has a fair match, while the rest of the water curve shows some deviation between the upscaled models and the fine-scale solution. There are small variations between the different upscaling methods. The water cut for the three producers which are not plotted here, show a better match than seen in Fig. 9.

As it is difficult to quantify the match from well curve plots as Fig. 9, we instead consider the error as defined in (6). The error in water production rate and injector BHP are plotted in Fig. 10.

The first observation we make about the error plot, is that the choice of one-phase upscaling method has larger impact on the error than the choice of relative permeability upscaling. The local pressure upscaling has a significantly smaller error than the two averaging methods for the injector BHP, and just slightly higher error than the arithmetic-harmonic method for the water rate. For the oil production rate (which is not plotted here), the two one-phase averaging methods have close to equal errors, and are slightly larger than the local pressure method. Thus, the pressure upscaling is the preferable one-phase method for this model.

Considering the two-phase methods, it is difficult to make any clear distinction, as the difference in the errors are small, and not consistent between the different well properties. Thus, from these results, we can not conclude that one of the two-phase upscaling methods is notably better or worse than the others. Even the averaging methods give equally good match with the fine-scale solution as the steady-state methods.

To check the influence of the capillary forces in this model, the upscaling and simulations are also run with the multiplier of the Leverett J-function in (8) set to both $\alpha = 0.1$ and $\alpha = 1$. This

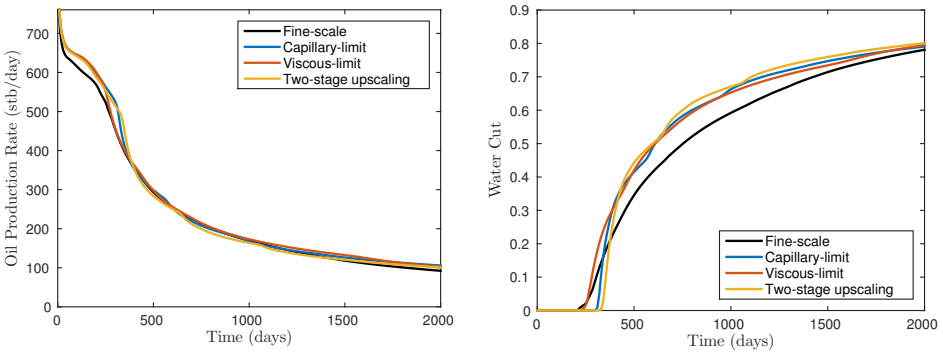

(a) Oil production rate.

(b) Water-cut.

Figure 9: Well-results for producer 1 in the SPE10 case for a selection of the upscaling methods.

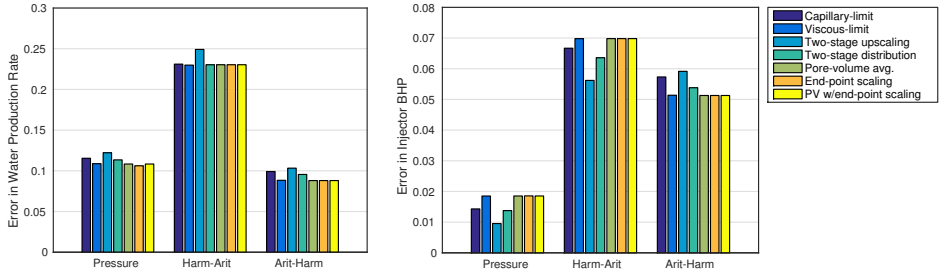

Figure 10: Error in well properties for the different upscaling methods in SPE10, as defined by (6). The different colors indicate the two-phase upscaling method used.

increases the capillary forces in the model, but the results show that it does not change any of the conclusions. That is, all upscaling methods still give about the same match with the fine-scale solution.

Also, to consider the impact of the relative permeabilities, we run the upscaling and simulations using varying relative permeability curves. In each region, the curves are scaled with the log-average permeability of that region. The endpoints are scaled between 0.05 and 0.15, and $k_{rw,\max}$ is scaled between 0.4 and 1. Also for these simulations, the error plots are still very similar to Fig. 10. The only notable difference is that the two-phase averaging methods are now slightly different from each other, but the differences are small and all two-phase methods still give about the same error.

As the absolute permeability upscaling is seen to have the largest impact on the solution, we also run the same simulations where the upscaled absolute permeability is replaced by *globally upscaled transmissibilities* [9]. To perform this upscaling, the pressure equation is solved on the whole fine-scale grid using some set of global boundary conditions, and then the fluxes from this global solution are used as boundary conditions when upscaling the transmissibility on each coarse face. Herein, we use the wells from the simulation as a single boundary condition. The two-phase upscaling is not changed, and we still apply the different local one-phase methods when upscaling the phase permeabilities as part of the relative permeability upscaling.

The error plots using global transmissibility upscaling are shown in Fig. 11. First, we note that the choice of one-phase method used as part of the two-phase upscaling has small impact on the solution. This shows that the difference in results seen in Fig. 10 is caused by the difference in permeability upscaling, and not by the one-phase method used as part of relative permeability upscaling. Second, the error using global transmissibility upscaling is about the same, or slightly larger, than the error using a local pressure upscaling. Thought the transmissibility upscaling takes

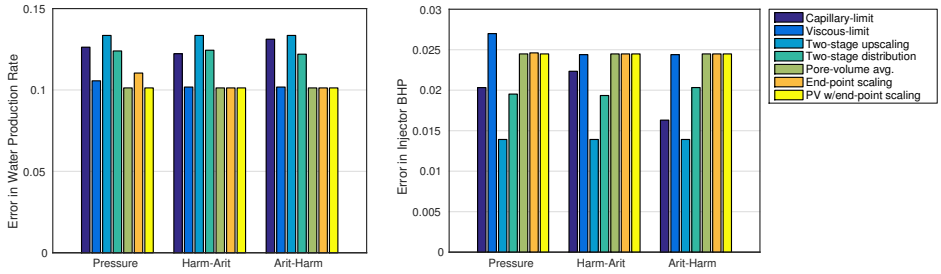

Figure 11: Error in well properties for the different upscaling methods in SPE10. Same plot as in Fig. 10, but now replacing the upscaled permeability by global upscaled transmissibilities.

into account the global flow pattern, this is computed using a single phase flow. As the saturation distribution changes in the model throughout the simulation, the transmissibility upscaling becomes less accurate.

As another test of the importance of two-phase upscaling and averaging, we create an upscaled model where both relative permeability and capillary pressure are simply pore-volume averaged across the *whole domain*. The upscaled model still has the same coarse grid and the same upscaled absolute permeability as before. Running the simulation with this coarse model, the results are almost identical to results using viscous-limit upscaling and block-wise pore-volume averaging. Thus, for this model and this choice of coarse grid, creating a single pair of relative permeability and a single capillary pressure curve simply by averaging gives equally good results as using the steady-state upscaling methods. This further shows that the choice of one-phase upscaling has the largest impact on the coarse-scale solution for this model.

In Fig. 12, we plot our fine-scale results and the results using the average model, together with non-pseudo upscaled results reported in [2]. Both for the fine-scale and average model simulations we now disregard gravity, in line with the simulations presented in in [2]. Both our fine-scale solution and the upscaled results are comparable with those presented in [2], however one must keep in mind the span of different upscaling methods and coarse grids used therein.

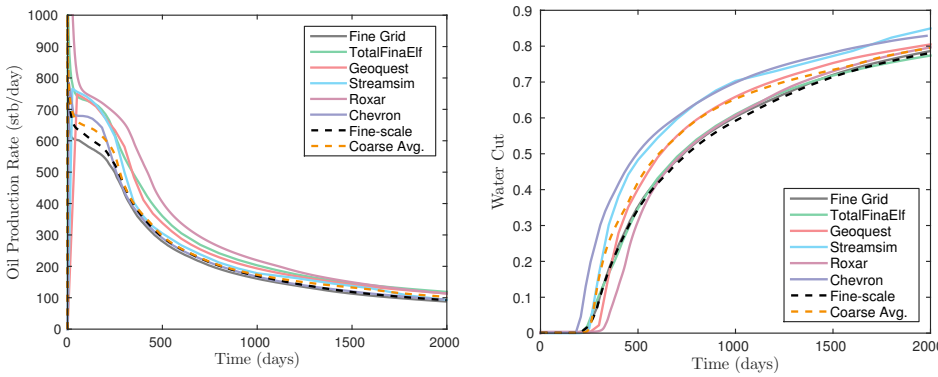

(a) Oil rate, producer 1.

(b) Water-cut, producer 1.

Figure 12: Comparison of our average models (shown in dotted lines) with the non-pseudo upscaled results reported in the original SPE10 paper [2]. Spreadsheets with original data is downloaded from `http://www.spe.org/csp`.

Even though computational efficiency is not the focus of this paper, it is of interest to note the dramatic speedup the upscaling brings. The full fine-scale system is computational heavy to solve;

on the computer we used, the full-scale simulations took between 4 and 6.5 days. The coarse-scale simulations, on the other hand, took between 10 and 15 seconds to complete. Even though tuning of the simulator parameters could impact simulation times significantly, the upscaled models all give relatively good agreement with the fine scale solution at a small fraction of the run-time.

3.3 Realistic Model 2: Fluvial Reservoir

In this section we will further investigate the impact of the different upscaling techniques discussed above. For simplicity, we will mostly use the local flow-based pressure method for single phase upscaling. At the end of this section, we will discuss the use of other one-phase methods.

We consider a fluvial reservoir model from the Norwegian continental shelf (NCS) described in [11]. The model is originally represented on a corner-point grid, but it has been regularized to make the simulations more efficient and upscaling easier to perform, and the grid has also been duplicated and mirrored to make it symmetric in the x-direction [12]. The model is shown in Fig. 13. The reservoir dimensions are $2000 \times 1000 \times 20$ m, and the grid dimensions are $100 \times 50 \times 80$, which gives grid cells of size $20 \times 20 \times 0.25$ m.

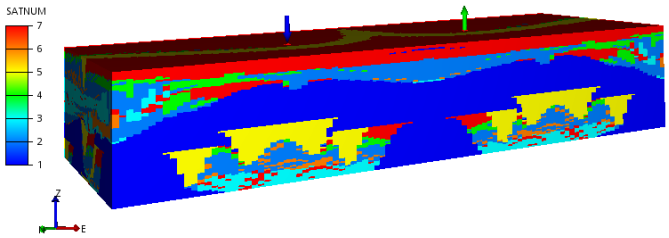

Figure 13: The representative fluvial reservoir model taken from a field on the NCS. The figure displays the rock type (SATNUM) distribution and the position of the wells.

There are seven different rock types in the model. Porosity and permeability vary throughout the domain, and also within a rock type. Each rock type has an associated pair of unique relative permeability curves and a capillary pressure curve, as shown in Fig. 14. This is in contrast to the SPE10 case above, where we applied J-function scaling and a single relative permeability curve to the whole domain.

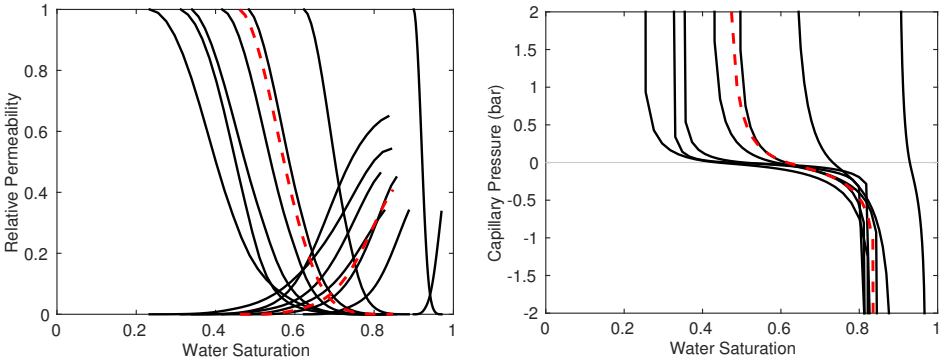

(a) Relative permeability.

(b) Capillary pressure.

Figure 14: Input curves for the different rock types of the fluvial model are plotted in black. A pore-volume weighted average of the curves are shown in dashed red lines.

Two vertical wells completed in all layers are placed 700 m apart. They are both placed away

from the no-flow boundaries to minimize boundary effects. We initialize the reservoir with $s_w = s_{wir}$, i.e. the irreducible water saturation, and pressure $p = 200\,\text{bar}$. In the simulations, the bottom hole pressure of the producer is kept constant at 200 bar. The injection rate is also kept constant within each simulation, but we run scenarios with different injection rates.

The model is upscaled to a coarse-scale model of grid size $20 \times 10 \times 4$, and thus each grid cell in the coarse grid have a physical size of $100 \times 100 \times 5\,\text{m}$, which is a typical size of a grid cell in a full field reservoir model. The upscaled relative permeability curves are plotted in Fig. 15 for all methods except for the end-point scaling methods. The relative permeability curves used for the end-point scaling method are plotted in Fig. 14 in red dashed lines, while the relative permeability curves used in the pore-volume average with end-point scaling are equal to the pore-volume average curves shown in Fig. 15f. Comparing the upscaled curves from the different methods, they are all strikingly similar.

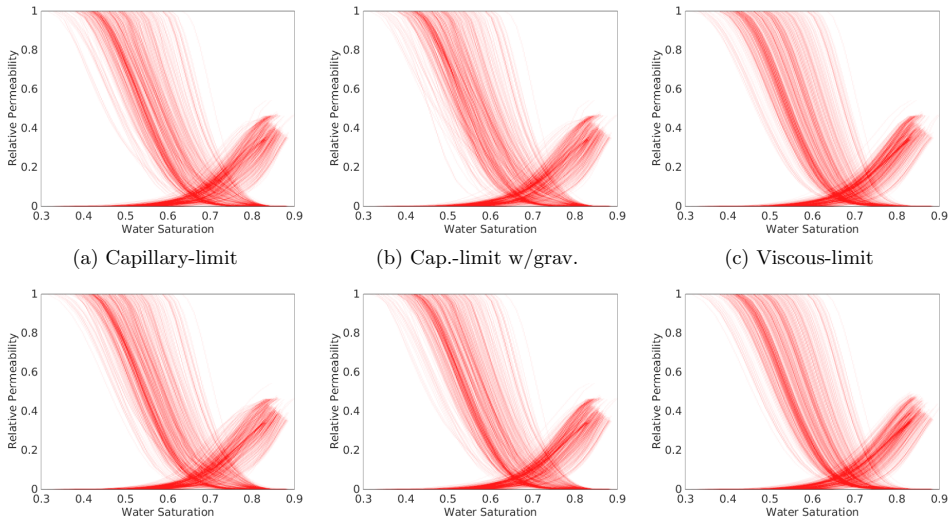

(a) Capillary-limit (b) Cap.-limit w/grav. (c) Viscous-limit

(d) Two-stage upscaling (e) Two-stage dist. (f) Pore-volume average

Figure 15: Upscaled relative permeabilities for all the 800 coarse blocks of the fluvial model shown as clouds, where stronger color indicates higher occurrence of curves.

3.3.1 Gravitational Forces

For viscous-limit upscaling, the gravitational forces are assumed negligible, and are therefore not included in the upscaling procedure. For capillary-limit and both two-stage method, however, gravity *may* be included in the upscaling procedure. As a sensitivity test, we perform the upscaling both including and disregarding the effect of gravity, and observe how this influences the coarse-scale simulations. The upscaled relative permeabilities are shown for the capillary-limit upscaling both with and without gravity in Fig. 15. Though it is possible to see slight differences, it seems like gravity has little impact on the upscaling for this model.

To further investigate the influence of including gravity in the upscaling procedure, we compare simulation results from the different coarse models with the fine-scale solution, using an injection rate of $200\,\text{m}^3$. The water cut for the different simulations are shown in Fig. 16, where gravity is included in all simulations. We observe almost no difference in the results depending on whether we have included or disregarded gravity in the upscaling process. Even though we have a clear fluid segregation due to gravity in the full model, the segregation inside a coarse block is relatively small, such that it has minor influence on the upscaled parameters. Larger density contrast or higher coarse blocks will increase the effect of gravity in the upscaled flow parameters.

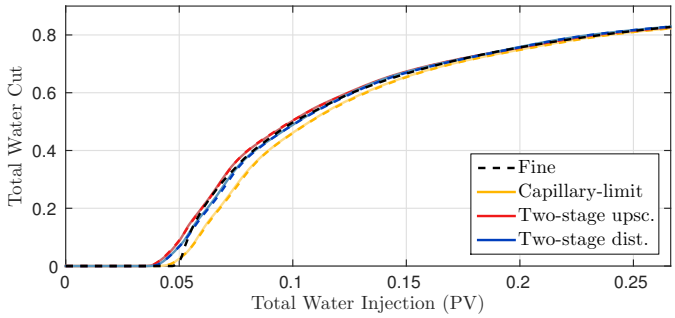

Figure 16: Water-cut versus cumulative water injection for the fluvial model. Coarse-scale results where gravity is included in the upscaling procedure are plotted in solid lines, while gravity is excluded in the upscaling for coarse-scale results plotted with dashed lines.

3.3.2 Capillary Forces

In the following, we will disregard gravity in both the upscaling and in the simulations to single out the effect of capillary forces. Flow simulations using the viscous-limit and both two-stage methods are compared to the fine-scale model for a range of injection rates in Fig. 17. An injection rate of $200\,\mathrm{m}^3$/day corresponds to an average water front velocity of $\sim 1.2\,\mathrm{ft}$/day, considered typical for this reservoir. As viscous-limit upscaling assumes that capillary forces are negligible, the upscaled models obtained using the viscous-limit and both two-stage methods do not contain any capillary pressure data. Thus, the results are equal for all injection rates when plotted versus cumulative injected water. The fine-scale model does on the other hand have capillary pressure data, and is therefore rate-dependent. As the capillary forces get more dominant for lower rates, the match between the coarse-scale results and the fine-scale solution deteriorates. We note that the two-stage methods gives a better match with the fine-scale solution than the viscous-limit for the typical injection rate of $200\,\mathrm{m}^3$/day.

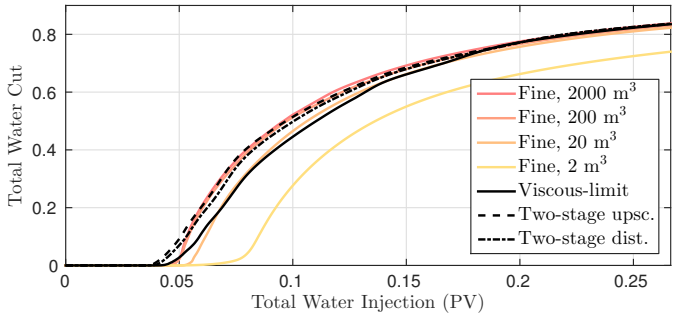

Figure 17: Field water-cut versus cumulative water injection volume for different injection rates in the fluvial model.

The flow simulation results using the other upscaling methods are plotted in Fig. 18. Even for high rates, where the capillary forces are assumed to be negligible, the capillary-limit upscaling gives a better match than the viscous-limit upscaling. In addition, as the capillary-limit coarse model includes capillary pressure, the water-cut curves move in the same direction as the fine-scale simulations. This is in contrast to the two-stage and viscous-limit methods, which are not rate-dependent. The capillary-limit upscaling is consistently better than the averaging and end-point scaling methods for all flow-rates.

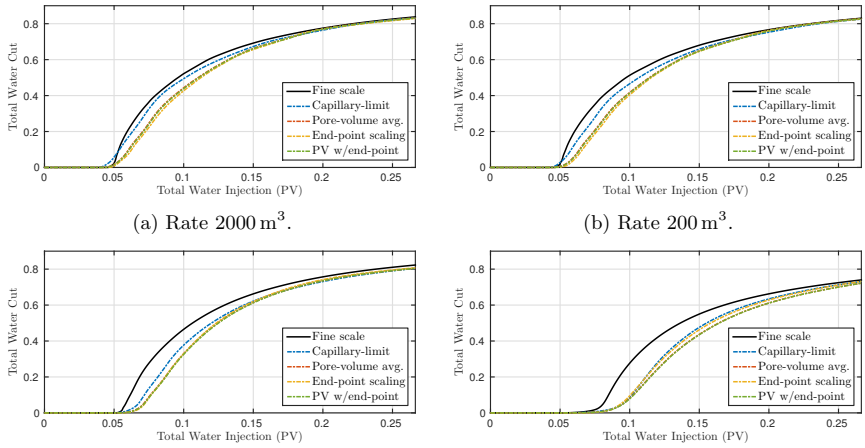

(a) Rate 2000 m^3. (b) Rate 200 m^3.

(c) Rate 20 m^3. (d) Rate 2 m^3.

Figure 18: Field water-cut for different upscaling methods and different rates in the fluvial model.

3.3.3 Different Upscaling Methods

As for the SPE10 example, we now perform both the single phase and the two-phase upscaling using the all the methods introduced. Error in the well properties for the different methods are displayed in Fig. 19. We observe a much larger variation between the different two-phase upscaling methods than was seen in Fig. 10 for SPE10. Even though we also ran the SPE10 model with relative permeabilities varying between the rock types, the variation in the fine-scale input curves is larger for the fluvial model, and we believe this is the main cause of the larger difference between the upscaled models.

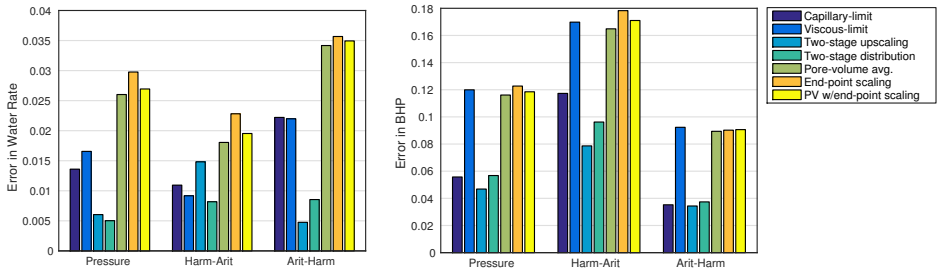

Figure 19: Error in well properties for the different upscaling methods in the fluvial model.

Arguably, the pressure and the aritmethic-harmonic one-phase methods produce better results than the harmonic-arithmetic. For both these one-phase methods, the two-stage methods yields somewhat better results than the capillary-limit method. Also, the capillary-limit method tends to give better results than the viscous-limit, which again is better than the simpler averaging and end-point scaling techniques.

For the water rate, the improvement gained by using the two-stage methods compared to capillary-limit upscaling is on the same order as the improvement gained by using capillary-limit compared to simple averaging techniques. However, as seen from Fig. 17 and also discussed earlier, the two-stage methods have a smaller range of applicability with respect to flow rates.

4 Conclusion

We have compared the use of different two-phase upscaling and averaging methods on a simplified model and on realistic field-scale models. We have also presented two different two-stage steady-state methods which assumes a capillary equilibrium normal to the flow direction and viscous equilibrium along the flow direction. These methods were suggested based on a previous study of force balance [7].

For the simple layered model, the capillary-limit method and both two-stage methods all gave equally good match with the fine-scale solution, and they performed notably better than the remaining methods. Thus, even though capillary forces dominate normal to the flow and viscous forces dominate in the flow direction during the flooding in this case, the capillary-limit upscaling still gave good results. This is because both before and after the water front, the saturation is close to capillary equilibrium within each coarse block, also in the flow direction.

In the SPE10 example, we observed that the choice of one-phase upscaling method had a larger impact on the solution than the two-phase method. The local flow-based permeability upscaling and global transmissibility upscaling gave the best results, with a slightly lower error seen for the flow-based method. This is in contrast to typical results from one-phase flow, where global transmissibility upscaling often is seen to perform better (see e.g. examples in [9]). The difference between the two-phase upscaling methods were almost negligible, and we were not able to characterize one method as better or worse than another. It is especially interesting to note that a simple pore-volume average of the two-phase properties give about the same results as the steady-state upscaling methods. For this example, we conclude that as long as the absolute permeability upscaling is performed using an appropriate method, the coarse simulation match the fine-scale simulation well, regardless of what two-phase strategy is chosen.

For the fluvial model, the impact of gravity in the upscaling was first considered. Even though it was seen that gravity created clear fluid segregation in the fine-scale simulations, it made little difference whether gravity was included in the upscaling or not.

In contrast to the SPE10 model, the choice of two-phase upscaling method was seen to be important for the fluvial model. Even though we also ran the SPE10 example using variable fine-scale relative permeabilities, the variance in the input curves was larger for the fluvial model, and this is believed to be the main cause of the larger variation between the upscaling methods. For the fluvial model, the capillary-limit method and both two-stage methods performed notably better than the other methods. Arguably, the two-stage upscaling method has a slightly closer match with the fine-scale solution than the other two. It is interesting to note that the two-stage methods give significantly better results than the viscous-limit upscaling. None of these three methods include capillary pressure in the coarse model, but the two-stage methods are able to capture some of the capillary effects in the upscaled relative permeabilities.

A single set of relative permeability curves in the coarse model was sufficient for the SPE10 example. This was however not the case for the fluvial model, where a single relative permeability gave notably worse results.

For typical reservoir rates, both two-stage methods and the capillary-limit upscaling gave good agreement with the fine-scale solution. However, as the flow-rate was decreased, the capillary-limit solution changed in a similar fashion as the fine-scale solution. At the same time, the match was seen to be increasingly worse. Thus, the capillary-limit captures some rate-dependency that the two-stage methods do not, but the dependency is not very accurate, and the low-rate solutions are not necessarily better than the two-stage or viscous-limit results.

Considering all simulations carried out, the capillary-limit method and both two-stage methods give the best results for the two-phase upscaling, and their results are quite similar. For the fluvial model, the two-stage upscaling method has a slightly better match with the fine-scale solution.

Acknowledgments

The research is funded by VISTA, which is a basic research program funded by Statoil and conducted in close collaboration with The Norwegian Academy of Science and Letters. The authors

thank Knut-Andreas Lie and Vegard Kippe for helpful discussions.

References

[1] M. Christie. Flow in porous media - scale up of multiphase flow. *Curr. Opin. Colloid Interface Sci.*, 6(3):236–241, 2001.

[2] M. Christie and M. Blunt. Tenth spe comparative solution project: A comparison of upscaling techniques. *SPE Reserv. Eval. Eng.*, 4(4):308–317, August 2001.

[3] M. Dale, S. Ekrann, J. Mykkeltveit, and G. Virnovsky. Effective relative permeabilities and capillary pressure for one-dimensional heterogeneous media. *Transp. Porous Media*, 26(3):229–260, March 1997.

[4] L. J. Durlofsky. Upscaling and gridding of fine scale geological models for flow simulation. In *8th International Forum on Reservoir Simulation Iles Borromees, Stresa, Italy, June 20-24, 2005*, 2005.

[5] S. Ekrann and J. O. Aasen. Steady-state upscaling. *Transp. Porous Media*, 41(3):245–262, December 2000.

[6] C. Farmer. Upscaling: A review. *Int. J. Numer. Meth. Fluids*, 40(1-2):63–78, September 2002.

[7] S. T. Hilden and C. F. Berg. Rate dependent force balance and upscaling of unsteady flooding processes. 2015.

[8] T. R. Lerdahl, A. B. Rustad, T. G. Theting, J. Å. Stensen, P. E. Øren, S. Bakke, T. Boassen, and B. Palatnik. Pore- to field scale multi-phase upscaling for IOR. In *SPE Europec/EAGE Annual Conference, 13-16 June 2005, Madrid, Spain*, 2005.

[9] K.-A. Lie. *An Introduction to Reservoir Simulation Using MATLAB.* SINTEF ICT, Department of Applied Mathematics, 2015.

[10] K.-A. Lie, S. Krogstad, I. Ligaarden, J. Natvig, H. Nilsen, and B. Skaflestad. Open-source MATLAB implementation of consistent discretisations on complex grids. *Comput. Geosci.*, 16:297–322, 2012.

[11] K. Nordahl, C. Messina, H. Berland, A. B. Rustad, and E. Rimstad. Impact of multiscale modelling on predicted porosity and permeability distributions in the fluvial deposits of the Upper Lunde Member (Snorre Field, Norwegian Continental Shelf). volume 387. Geological Society of London, 2014.

[12] L. H. Odsæter, C. F. Berg, and A. B. Rustad. Rate dependency in steady-state upscaling. *Transport in Porous Media*, 110(3):565–589, 2015.

[13] G. Pickup, P. Ringrose, and A. Sharif. Steady-state upscaling: From lamina-scale to full-field model. *SPE J.*, 5(2):208–217, June 2000.

[14] P. Renard and G. de Marsily. Calculating equivalent permeability: a review. *Adv. Water Resour.*, 20(5–6):253 – 278, 1997.

[15] P. S. Ringrose, K. S. Sorbie, P. W. M. Corbett, and J. L. Jensen. Immiscible flow behaviour in laminated and cross-bedded sandstones. *J. Petrol. Sci. Eng.*, 9(2):103–124, April 1993.

[16] A. B. Rustad, T. G. Theting, and R. J. Held. Pore space estimation, up scaling and uncertainty modeling for multiphase properties. In *SPE Symposium on Improved Oil Recovery, 20-23 April 2008, Tulsa, Oklahoma, USA*, 2008.

[17] Schlumberger. *ECLIPSE 2013.2 Reference Manual*, 2013.

[18] Schlumberger. ECLIPSE 100 reservoir simulator, 2015. http://www.software.slb.com/products/eclipse.

[19] Sintef. The MATLAB Reservoir Simulation Toolbox, MRST 2015a, May 2015. http://www.sintef.no/MRST/.

[20] E. H. Smith. The influence of small-scale heterogeneity on average relative permeability. In *Reservoir Characterization II*, pages 52–76. Academic Press, Inc., 1991.

Paper III

Steady-State Upscaling of Polymer Flooding

Sindre Tonning Hilden, Knut-Andreas Lie, and Xavier Raynaud

ECMOR XIV - 14th European Conference on the Mathematics of Oil Recovery, Catania, Sicily, Italy, 8-11 September 2014

Is not included due to copyright

Paper IV

Multiscale Simulation of Polymer Flooding with Shear Effects

Sindre Tonning Hilden, Olav Møyner, Knut-Andreas Lie, and Kai Bao

Submitted

Multiscale Simulation of Polymer Flooding with Shear Effects

Sindre T. Hilden Olav Møyner Knut-Andreas Lie Kai Bao

Preprint, March 29, 2016

Abstract

We formulate a sequentially-implicit solution procedure for simulating polymer flooding with non-Newtonian rheology and use this as a basis to formulate an efficient and versatile multiscale solver that potentially can be used to increase the resolution in field-scale simulations. The multiscale method relies on a coarse partition of the underlying fine grid and uses a set of local prolongation operators to map unknowns in cells to unknowns associated with blocks in the coarse partition. These mappings are computed by restricted smoothing: Starting from a constant inside each block, a localized iterative scheme is applied to the fine-scale discretization to numerically construct prolongation operators that are consistent with the local properties of the spatial differential operators. The result is a flexible method in which partitions and robust prolongation operators can easily be constructed semi-automatically for complex geo-cellular models with high media contrasts and unstructured cell connections. Likewise, transient behavior caused by dynamic mobility changes can easily and inexpensively be incorporated by continuing to iterate a few extra steps on the existing prolongation operators. The prolongation operators are then combined with a finite-volume restriction operator to formulate a global coarse-scale system that can be used to iterate the fine-scale pressure residual below a prescribed tolerance. Once a sufficiently accurate pressure approximation is obtained, mass-conservative fluxes can be reconstructed by solving a set of local flow problems.

Our sequential solution procedure and multiscale solver are verified against a well-established commercial simulator on a test case with simple geometry, highly heterogeneous media properties, and strongly nonlinear fluid behavior. Next, the sequential fine-scale and multiscale solvers are validated on a synthetic simulation model of a shallow-marine reservoir. Here, the computational time is dominated by the pressure solves, and 5–6 times speedup is observed when replacing the fine-scale pressure solver by the iterative multiscale method. We also demonstrate the flexibility of the method by applying it to model with unstructured polyhedral cells that adapt to well positions and faults.

1 Introduction

Water-based methods for enhanced oil recovery (EOR) consist of adding active chemical or biological substances that modify the physical properties of the fluids and/or the porous media at the interface between oil and water. Herein, we consider polymer flooding, in which polymer molecules of relatively large size are added to the injected water to improve the local displacement as well as the global sweep efficiency of the waterflood. While polymer flooding is a relatively mature technology onshore, it has proved difficult to demonstrate the business case of polymer flooding for offshore fields. There are many reasons for this, including high-salinity formation water, well placement and large well spacing, stability under injection, HSE requirements, logistic difficulties, etc. Herein, however, we will focus on the challenge of being able to perform simulations with sufficient spatial resolution, as it is well known that unresolved simulations of EOR schemes can lead to misleading predictions of injectivity and recovery profiles, see e.g., [44, 20].

Today, most geological reservoir models are made with much higher spatial resolution than what can be utilized in a conventional reservoir simulator, except if the simulator utilizes massive parallelization. Some form of model upscaling is therefore necessary, which inevitably introduces two forms of errors: (i) *homogenization errors* induced by neglecting subscale heterogeneities, and (ii) *truncation errors* induced by lower resolution in the numerical discretization. Various types of

multiscale methods have been proposed over the past two decades to reduce homogenization errors and to overcome the limitations of traditional upscaling methods, see [17, 4, 8, 18, 30, 12]. Some of these methods have been developed to a point where they can handle realistic reservoir models [23, 41, 2, 34, 35, 42, 21, 11]. The key idea of such multiscale methods is to construct a set of prolongation operators (or basis functions) that map between unknowns associated with cells in a grid that represents the petrophysical properties of the reservoir and unknowns on a coarser grid used for dynamic simulation. The prolongation operators are computed numerically by solving localized flow problems, much in the same way as for flow-based upscaling methods, and can be used to construct a reduced coarse-scale system of flow equations that describe the macro-scale displacement driven by global forces. Unlike effective parameters, the multiscale basis functions have subscale resolution which ensures that fine-scale heterogeneity is correctly accounted for in a systematic manner. Linear combinations of basis functions will only resolve a linearized elliptic part of the system, and most multiscale methods therefore employ some kind of residual iteration to eliminate localization errors and account for nonlinear parabolic flow effects.

Multiscale methods have so far predominantly been used to study single-phase flow or secondary recovery methods. The latter are characterized by a combination of spreading and shelf-sharpening waves and are hence somewhat forgiving towards numerical truncation errors. The simulation of EOR methods, on the other hand, is much more sensitive to grid resolution. The reason for this is a complex interplay between the transport of chemical substances and how these substances affect the flow by changing the properties of the fluids and the surrounding rock. The transport of chemical substances is largely a linear process and thus strongly affected by numerical diffusion. The effects chemicals have on fluid and rock properties are generally highly nonlinear and highly sensitive to threshold parameters that determine sharp transitions between regions of very different behavior. For polymer flooding, in particular, the polymer fronts are not self-sharpening like water fronts. High numerical resolution is therefore required to limit numerical diffusion which would otherwise bias or deteriorate simulation results.

The high grid resolution needed to accurately account for polymer effects, will in most cases make field-scale simulation of offshore polymer flooding computationally intractable by traditional reservoir simulators. To overcome this problem, one can either reduce the computational time through massive parallelization, use dynamic gridding strategies [16], and/or reduce the overall computational cost by exploiting weak couplings in the flow equations to formulate efficient sequential solution procedures. One example is streamline simulation [3, 10], another example is methods based on identification of connected components in the transport equations [40], which may provide order-of-magnitude speedup compared with standard Newton–Raphson type solvers for the saturation-concentration part of the problem, see [28, 29]. In many cases, resolving the pressure component of the equation system is the part that contributes most to the overall computational cost. Similar to the multiscale methods, nested-gridding [13, 5] reduces this cost by solving the pressure system on a coarse grid, and these methods have also been applied to polymer flooding [6]. However, in contrast to the multiscale methods, nested-gridding does not offer a consistent way of the reducing the fine-scale residual. Herein, we will therefore investigate to what extent one can utilize a state-of-the art multiscale method [37, 39, 38] developed for standard black-oil type flow models to reduce homogenization errors and accelerate the simulation of polymer flooding with shear-thinning and thickening effects. Truncation errors will be reduced by solving the saturation-concentration part of the problem on the underlying geological grid.

To enable the use of the multiscale method, we first formulate a sequential solution procedure. To the best of our knowledge, this has not yet been reported in the literature. We can then easily adapt our iterative multiscale method to the resulting pressure equation, even though this has a different type of nonlineary, because of the non-Newtonian fluid rheology, than what has previously been studied with multiscale methods. In the particular multiscale method, called MsRSB [37, 39, 38], elliptic prolongation operators are constructed by restricted smoothing: Starting from a constant inside each block of the coarse partition, a localized iterative scheme is applied to the fine-scale discretization to numerically construct basis functions that are consistent with the local properties of the spatial differential operators. The basis functions have support inside a small interaction region surrounding each coarse block, form a partition of unity by construction, and

can easily be modified to account for transient flow phenomena by continuing to iterate a few extra steps with updated dynamic mobility changes. The corresponding prolongation operator is then combined with a standard finite-volume restriction operator to derive a multiscale equation system for the global flow problem. By using the multiscale solver along with an inexpensive smoother to efficiently reduce the fine-scale error, we can compute an approximate pressure field that satisfies a prescribed tolerance, and subsequently reconstruct a set of mass-conservative fluxes that can be used to evolve the saturation and polymer concentration on the original fine grid. The result is a flexible method that can either be used as a robust upscaling-downscaling method, or as an accelerated iterative solver that is guaranteed to produce a conservative flux field for any stopping criterion on the fine-scale residual. To the best of our knowledge, the method presented herein is the first multiscale method designed to account for non-Newtonian fluid rheology.

Through a series of numerical experiments, we verify and validate the multiscale method. First, the correctness of the sequential formulation and our multiscale solver are first verified against ECLIPSE 100 for idealized tests cases with heterogeneity sampled from the SPE 10 benchmark [9]. Then, the multiscale solver is validated on a model of a shallow-marine reservoir by showing that it can effectively resolve the highly nonlinear flow physics of a shear-thinning polymer flooding on a model with industry-standard complexity. Last, but not least, we demonstrate the geometrical flexibility of the MsRSB method by applying it to a test case with general polyhedral cells that adapt to wells and faults. Through the different examples, we show that the multiscale method can be set to reproduce the results of a fully-implicit simulator, but also can be used to trade accuracy for computational efficiency by computing approximate flux fields that are mass-conservative and satisfy a prescribed residual tolerance.

2 Model Description

As our basic flow model, we consider an immiscible, two-phase, three-component, black-oil system that includes the flow effects offered in contemporary commercial simulators. This includes adsorption of polymer onto the reservoir rock, fluid and rock compressibilities, permeability and porosity reduction, a Todd–Longstaff model for the mixing of polymer into water, and non-Newtonian fluid rheology for the diluted polymer. Understanding the rheological behavior of the polymer-water mixture on a reservoir scale is particularly important to successfully design and evaluate an offshore polymer flooding project. In most cases, the diluted polymer solution is a pseudoplastic (non-Newtonian) fluid, whose apparent viscosity decreases when subjected to sufficiently high shear rates, which causes the polymer molecules to uncoil, untangle, and align and elongate with the flow direction. Shear-thinning behavior is beneficial in that it improves injectivity by lowering the viscosity in the near-well zone where shear rates are high. As the injected fluids move away from the well, shear rates decline and viscosity increases, gradually establishing the desired mobility control in terms of a more stable and sharper displacement front. The disadvantage of a shear-thinning fluid is that it has a higher tendency to flow in high-permeable regions, which may impair sweep efficiency and hence reduce attainable recovery and/or lead to significantly higher operation and processing costs. Diluted polymer solutions may also exhibit shear-thickening (pseudodilatant) behavior, which can improve sweep efficiency but reduces injectivity.

The primary physical variables in the mathematical model are the oil and water pressures, p_o and p_w, the oil and water saturations, s_o and s_w, and the polymer concentration c_p. The concentration is given in units of mass per volume of water. It is assumed that the presence of polymer changes the properties of the water, but does not influence the properties of the oil phase. The conservation equations for oil, water, and water with polymer are

$$\frac{\partial}{\partial t}\left(\phi b_o s_o\right) + \nabla\cdot\left(b_o v_o\right) = b_o q_o, \tag{1a}$$

$$\frac{\partial}{\partial t}\left(\phi b_w s_w\right) + \nabla\cdot\left(b_w v_w\right) = b_w q_w, \tag{1b}$$

$$\frac{\partial}{\partial t}\left(\phi b_w(1-s_{\mathrm{ipv}})s_w c_p\right) + \frac{\partial}{\partial t}\Big((1-\phi_{\mathrm{ref}})\rho_r c_a\Big) + \nabla\cdot\left(b_w c_p v_p\right) = b_w q_p, \tag{1c}$$

with the closing relation $s_w + s_o = 1$. The Darcy velocities are given by the multiphase extension of Darcy's law

$$v_o = -\frac{k_{ro}}{\mu_o} K \left(\nabla p_o - g\rho_o \nabla z\right), \tag{2a}$$

$$v_w = -\frac{k_{rw}}{\mu_{w,\text{eff}} R_k} K \left(\nabla p_w - g\rho_w \nabla z\right), \tag{2b}$$

$$v_p = -\frac{k_{rw}}{\mu_{p,\text{eff}} R_k} K \left(\nabla p_w - g\rho_w \nabla z\right). \tag{2c}$$

The porosity ϕ, absolute permeability K, phase pressures p_α, fluid densities ρ_α, and formation volume factors $b_\alpha = 1/B_\alpha$ which relate surface and reservoir volumes of fluid phase α are familiar from the two-phase black-oil equations, where $\alpha = \{o, w\}$. The inclusion of polymer in the reservoir has a number of different effects on the flow, which is modeled through a number of parameters related to the polymer: R_k is the permeability reduction factor, s_{ipv} denotes the inaccessible pore volume, c_a is the amount of polymer adsorbed on the rock surface, ρ_r is the rock density, and ϕ_{ref} a reference porosity. The details of these parameters, and the physical effects they model, are described in more detail below.

Viscosity influence. Adding polymer to the water results in an increased viscosity of the solution. The effective viscosities of water and polymer are denoted by $\mu_{w,\text{eff}}$ and $\mu_{p,\text{eff}}$, respectively. These effective viscosities are defined using the Todd–Longstaff mixing model [45]. The viscosity of a fully mixed solution of water and polymer is denoted by $\mu_m(c_p)$, and the effective polymer viscosity is given by

$$\mu_{p,\text{eff}} = \mu_m(c_p)^\omega \mu_p^{1-\omega},$$

where $c_{p,\max}$ is the maximum possible polymer concentration, $\mu_p = \mu_m(c_{p,\max})$, and $\omega \in [0, 1]$ is the Todd–Longstaff mixing parameter. For $\omega = 1$, the polymer solution and the water are fully mixed, whereas for $\omega = 0$ if the polymer solution is completely segregated from the pure water. Values of ω in between 0 and 1 model partial mixing. The viscosity of partially mixed water is defined as

$$\mu_{w,e} = \mu_m(c_p)^\omega \mu_w^{1-\omega}.$$

The effective water viscosity $\mu_{w,\text{eff}}$ is then given by

$$\frac{1}{\mu_{w,\text{eff}}} = \frac{1 - c_p/c_{p,\max}}{\mu_{w,e}} + \frac{c_p/c_{p,\max}}{\mu_{p,\text{eff}}}. \tag{3}$$

We also define a viscosity multiplier m_μ, such that

$$\mu_m(c_p) = m_\mu(c_p)\mu_w, \tag{4}$$

where $m_\mu(c_p)$ is given as input, instead of specifying $\mu_m(c_p)$ directly. We also note a useful relation between the water and polymer flux, writing $v_p = m(c_p)v_w$, where $m(c_p)$ can be expressed as

$$m(c_p) = \frac{\mu_{w,\text{eff}}}{\mu_{p,\text{eff}}} = \left[\left(1 - \frac{c_p}{c_{p,\max}}\right)\left(\frac{\mu_p}{\mu_w}\right)^{1-\omega} + \frac{c_p}{c_{p,\max}}\right]^{-1}.$$

Inaccessible pore volume. Polymer molecules are large relative to the water and hydrocarbons in the reservoir and a portion of the pore volume may therefore be inaccessible to the polymer, as they are unable to enter the smallest pores. This may result in an accelerated polymer flow, and this effect is included in (1c) with the value s_{ipv}, which is the fraction of the pore volume not accessible to polymer, commonly referred to as the *inaccessible pore volume* or *dead pore space*.

Adsorption. Adsorption is the effect of polymer molecules attaching to the rock surface. This will cause the polymer concentration in the solution to decrease, and consequently so will the viscosity. The adsorption function $c_a(c_p)$ gives the relationship between the polymer concentration and the amount of adsorbed polymer. Herein, we assume the adsorption effect is instantaneous and reversible, such that polymer detaches from the rock if the concentration decreases.

Permeability reduction. The mobility of a water-polymer solution is reduced because of an increased viscosity, but some types of polymer also experience a reduction in the permeability [24]. This can be explained by the adsorption, as the large polymers attached to the rock reduces the effective pore size for the flowing polymer solution. The permeability reduction effect is modeled by the reduction factor R_k, defined by

$$R_k(c_p) = 1 + (R_{RF} - 1)\,\frac{c_a(c_p)}{c_{a,\max}}, \tag{5}$$

where $R_{RF} \geq 1$ is called the residual resistance factor and $c_{a,\max}$ is the maximum adsorption.

Non-Newtonian behavior. A fluid is called *Newtonian* if there is a linear relationship between the shear stress and the strain rate (the change in shear strain). If this relationship is not linear, the fluid is called *non-Newtonian*. A *pseudodilatant*, or *shear-thickening*, fluid increases resistance with increasing applied stress, whereas a *pseudoplastic*, or *shear-thinning*, fluid decreases resistance with increasing stress. For a polymer solution at low shear rates, there is a linear relationship between the shear stress and the shear rate, and the solution is a Newtonian fluid. However, at higher shear rates, the viscosity decreases. This shear-thinning effect in polymer solutions is caused by the uncoiling and unsnagging of polymer chains when they are elongated in shear flow [24]. Throughout the reservoir, the flow-rates are usually low and so are the shear stresses. But near the injection well, the shear rates can be quite high and the effect of shear thinning can consequently be large. The viscosity of a polymer solution is also highly sensitive to the salinity of the water, but his is not discussed herein.

Mathematical formulation of shear thinning. The shear-thinning effect is included by modifying the effective viscosities by a shear-thinning multiplier M_{sh} such that the resulting viscosities becomes

$$\mu_{w,\text{sh}} = \mu_{w,\text{eff}} M_{\text{sh}}, \qquad \text{and,} \qquad \mu_{p,\text{sh}} = \mu_{p,\text{eff}} M_{\text{sh}}.$$

This multiplier is computed as follows [43]: Given the discrete water flux v_w, computed from the discretized form of equation (2b) without any shear effect, the water velocity is defined on each face of the discrete grid as

$$u_w = \frac{v_w}{\phi A},$$

where the porosity ϕ is taken as the average of the two neighboring cells, and A is the face area. The product ϕA is then the available area for the fluids to flow through each particular face. Using the water velocity, the shear-modified water velocity $u_{w,\text{sh}}$ is calculated using the implicit equation

$$u_{w,\text{sh}} = u_w \frac{\mu_{w,\text{eff}}}{\mu_{w,\text{sh}}} \tag{6}$$

where $\mu_{w,\text{sh}} = \mu_{w,\text{sh}}(u_{w,\text{sh}})$ is the shear-modified water viscosity defined by

$$\mu_{w,\text{sh}} = \mu_{w,\text{eff}} M_{\text{sh}} = \mu_{w,\text{eff}} \left(\frac{1 + (m_\mu - 1) m_{\text{sh}}}{m_\mu} \right).$$

Here, $m_\mu = m_\mu(c_p)$ is the viscosity multiplier defined in (4), and $m_{\text{sh}} = m_{\text{sh}}(u_w)$ is a shear multiplier, which depends on the water velocity, and is given as input. Solving (6) gives the shear-viscosity multiplier M_{sh}, and so both modified viscosities can be computed, and consequently also the modified phase fluxes, which are then given by

$$v_{w,\text{sh}} = \frac{v_w}{M_{\text{sh}}}, \qquad \text{and} \qquad v_{p,\text{sh}} = \frac{v_p}{M_{\text{sh}}}.$$

3 Sequential Formulation

To apply the multiscale method, we need to formulate our equations (1) in a sequential form. In the following, we explain the splitting of the equations (1) without polymer shear thinning, and then afterwords, we address how the shear-thinning calculation is included in the sequential solver. Wells are left out of equations below to ease readability. For details on how wells are included in our implementation, we refer to [38].

3.1 Pressure equation

To find an equation for the pressure only, we start by discretizing the conservation equations (1) in time using the backward (implicit) Euler method to obtain the following semi-discrete equations, written in residual form;

$$\mathcal{R}_o = \frac{1}{\Delta t}\left[(b_o\phi s_o)^{n+1} - (b_o\phi s_o)^n\right] + \nabla\cdot(b_o v_o)^{n+1} = 0, \tag{7a}$$

$$\mathcal{R}_w = \frac{1}{\Delta t}\left[(b_w\phi s_w)^{n+1} - (b_w\phi s_w)^n\right] + \nabla\cdot(b_w v_w)^{n+1} = 0, \tag{7b}$$

$$\begin{aligned}\mathcal{R}_p = {}& \frac{1}{\Delta t}\left[(b_w\phi s_w c_p)^{n+1} - (b_w\phi s_w c_p)^n\right] \\ & + (1-\phi_{\text{ref}})\rho_r\frac{1}{\Delta t}\left[c_a^{n+1} - c_a^n\right] + \nabla\cdot(b_w c_p v_p)^{n+1} = 0.\end{aligned} \tag{7c}$$

Here, superscript denotes the discrete time and $\Delta t = t^{n+1} - t^n$ is the time step. To remove the dependence of the saturations and concentration at the next time step, we sum these equations as

$$\mathcal{R}_t = \beta_o\mathcal{R}_o + \beta_w\mathcal{R}_w + \beta_p\mathcal{R}_p = 0,$$

where we assume there exist β-factors such that $\mathcal{R}_t$ only depends on the pressure at time $n+1$. We construct the pressure equation in the same way as is usual in the two-phase case, and so using factors

$$\beta_o = \frac{1}{b_o^{n+1}}, \qquad \beta_w = \frac{1}{b_w^{n+1}}, \qquad \text{and} \qquad \beta_p = 0,$$

we get

$$\mathcal{R}_t = \frac{\phi^{n+1}}{\Delta t} - \frac{\phi^n}{\Delta t}\left[\frac{(b_o s_o)^n}{b_o^{n+1}} + \frac{(b_w s_w)^n}{b_w^{n+1}}\right] + \frac{\nabla\cdot\left(b_o^{n+1}v_o^{n+1/2}\right)}{b_o^{n+1}} + \frac{\nabla\cdot\left(b_w^{n+1}v_w^{n+1/2}\right)}{b_w^{n+1}} = 0,$$

where we have used the relation $s_o + s_w = 1$ to eliminate the saturations at the next time step. This is the standard IMPES pressure equation where the effect of polymer comes from the water viscosity. The fluxes in $\mathcal{R}_t$ are given by

$$v_o^{n+1/2} = -\frac{Kk_{ro}(s_o^n)}{\mu_o(p^{n+1})}\left[\nabla p_o^{n+1} - g\rho_o\nabla z\right], \tag{8a}$$

$$v_w^{n+1/2} = -\frac{Kk_{rw}(s_w^n)}{\mu_{w,\text{eff}}(p^{n+1}, c_p^n)R_k(c_p^n)}\left[\nabla p_o^{n+1} - \nabla p_{\text{cow}}(s_w^n) - g\rho_w\nabla z\right]. \tag{8b}$$

We denote the phase fluxes with the discrete time $n+1/2$ to indicate that they are computed using pressures at time $n+1$ and saturations and concentration at time n, and thus can be thought of as intermediate fluxes. We have now obtained the equation

$$\mathcal{R}_t = \mathcal{R}_t(p_o^{n+1}; p_o^n, s_w^n, c_p^n) = 0, \tag{9}$$

which can be solved for p_o^{n+1} using the Newton–Raphson method. Here, we have written the equation in terms of the oil pressure, but we could equally well have solved for the water pressure.

The pressure equation (9) is discretized by a standard two-point flux-approximation scheme with upstream mobility weighting of all terms that depend on saturations and polymer concentrations;

see e.g., [38] for more details. The resulting nonlinear system is linearized and solved by a Newton–Raphson method. Shear-thinning effects will generally induce strong nonlinearities in the discrete system since the effective water viscosity now depends on the water velocity u_w and the polymer concentration c_p. In the linearized pressure equation of the sequential formulation, the dependence on c_p is treated explicitly while the dependence on u_w is treated implicitly. Moreover, to reduce the nonlinearity of the pressure system, the shear-thinning effect is accounted for in an inner iteration. That is, we do not account for the fact that the water viscosity depends on water velocity when linearizing the global pressure equation, but rather use another Newton loop to linearize and solve (6) to a prescribed tolerance for each (outer) pressure iteration. Once the overall system is solved, the pressure p_o^{n+1} at the next time step is known, as well as the fluxes (8) and all fluid viscosities, which all are considered to be constant during the subsequent transport step.

3.2 Transport equation

To evolve the saturations and the concentration, we first find expressions for the phase fluxes in terms of the total flux $v_T = v_o + v_w$. From (2), we compute v_T and rearrange to find an expression for ∇p_o in terms of v_T. This is then inserted back into each phase flux (2) to obtain phase fluxes expressed in terms of the total flux. From the pressure solution, we are given the total flux $v_T^{n+1} = v_o^{n+1/2} + v_w^{n+1/2}$. Each phase flux at the discrete time $n+1$ is then given by

$$
\begin{aligned}
v_o^{n+1} &= f_o\Big[v_T^{n+1} + K\lambda_w\big(\rho_o g\nabla z - \rho_w g\nabla z\big)\Big],\\
v_w^{n+1} &= f_w\Big[v_T^{n+1} + K\lambda_o\big(\rho_w g\nabla z - \rho_o g\nabla z\big)\Big],\\
v_p^{n+1} &= f_p\Big[v_T^{n+1} + K\lambda_o\big(\rho_w g\nabla z - \rho_o g\nabla z\big)\Big],
\end{aligned}
$$

where $f_\alpha = \lambda_\alpha/(\lambda_o + \lambda_w)$ is the fractional flow, and λ_α are the mobilities given by

$$
\lambda_o = \frac{k_{ro}}{\mu_o}, \qquad \lambda_w = \frac{k_{rw}}{\mu_{w,\mathrm{eff}} R_k}, \qquad \lambda_p = \frac{k_{rw}}{\mu_{p,\mathrm{eff}} R_k}.
$$

The capillary pressure is left out of the above flux expressions just for readability. The resulting transport equation is discretized using a standard finite-volume method. To evaluate the mobilities λ_α on the faces of each grid cell, we use potential ordering to determine the upstream weighting [7], which in most cases coincides with the upstream weighting used in the pressure solver.

We now choose two of the three conservation equations (7) to solve for, and then insert the above phase fluxes into these equations. Through numerical experiments, we have in some cases experienced convergence problems using conservation of water together with the polymer equation. We therefore choose to solve the oil and polymer equations, and then let the water fill up the remaining pore space. For the temporal discretization, we can either use the backward or forward Euler method, which result in a sequentially-implicit or a IMPES-type simulator, respectively. To allow for larger time-steps, we have chosen an implicit discretization. That is, we solve the system

$$
\mathcal{R}_s = \mathcal{R}_s(s_w^{n+1}, c_p^{n+1}; s_w^n, c_p^n, v_T) = [\mathcal{R}_o, \mathcal{R}_p]^T = 0, \tag{10}
$$

where $\mathcal{R}_o$ is given in (7a), and $\mathcal{R}_p$ in (7c), but now with the phase fluxes expressed in terms of the total flux. Herein, we use a standard Newton–Raphson method to solve (10), but remark that it is generally possible to use topological of grid cells according to total velocity to develop nonlinear solvers that are significantly more efficient for cases with small or moderate contrasts in water and oil densities [28, 29].

3.3 Solving the nonlinear problem

For clarity, let us summarize our sequentially-implicit method. Assume the state (p_o^n, s_w^n, c_p^n) is known at discrete time n. One time-step is then performed using the following steps:

1) Solve the pressure equation (9) by the Newton–Raphson method. Let subscript i denote the iteration count in the Newton-loop. Set initial guess $p_{i=0} = p_o^n$ (i.e., the oil pressure at time n), and then iterate the following steps:

   a) Construct $\mathcal{R}_t(p_i)$ and its Jacobian J_p. To this end, we have to perform a nested Newton-loop to compute the shear-thinning multipliers by solving (6).

   b) Find the pressure increment Δp by solving

$$-J_p \Delta p = \mathcal{R}_t(p_i). \tag{11}$$

   c) Update pressure by $p_{i+1} = p_i + \Delta p$.

   d) Check the following convergence criterion

$$\|p_{i+1} - p_i\|_\infty \leq \varepsilon_p \left(\max p_i - \min p_i\right), \tag{12}$$

   for some prescribed tolerance ε_p. If we have not converged, set $i \leftarrow i + 1$ and go to (a).

   At convergence, set the pressure at the next time-step, $p_o^{n+1} = p_{i+1}$, and compute the total flux v_T by using phase-fluxes (8).

2) Given the total flux v_T, construct and solve the transport equation (10) using Newton–Raphson iterations. If we denote $s = (s_w, c_p)^T$, then set $s_{i=0} = s^n$, and perform iterations

$$-J_s \Delta s = \mathcal{R}_s(s_i), \qquad s_{i+1} = s_i + \Delta s,$$

   where J_s is the Jacobian of $\mathcal{R}_s(s_i)$. For the oil equation, the convergence is defined using both a maximum error and a total error,

$$\left\| \frac{\Delta t \mathcal{R}_o}{\phi} \right\|_\infty \leq \varepsilon_V b_o^{\text{avg}}, \qquad \frac{\|\Delta t \mathcal{R}_o\|_1}{\|\phi\|_1} \leq \varepsilon_M b_o^{\text{avg}},$$

   whereas for the polymer equation, we use an incremental tolerance,

$$\|c_{i+1} - c_i\|_\infty \leq \varepsilon_c c_{p,\max}.$$

   At convergence, the time-step is complete, and we proceed to the next time-step.

If required, the sequential implicit procedure outlined above can be extended with an outer iteration over the pressure and transport steps to ensure that the overall fine-scale residual is reduced to within a prescribed tolerance at the end of the time step. The result is what is sometimes referred to as an iterated fully-implicit solution procedure.

4 Multiscale Pressure Solution

Solving the linearized pressure system (11) is computationally expensive and becomes the largest contributor to the total runtime for large systems. Instead of solving (11) directly, we compute an approximate solution using an iterative multiscale solver. To this end, we will use the MsRSB method [37, 39, 38], which has proved to be a particularly versatile method that can robustly handle both the complexity in flow physics and geological description seen in real-life simulation models. The method incorporates concepts and insight from previous multiscale methods, including algebraic [47, 31, 46] and iterative [14, 32, 15, 48, 46] formulations, as well as flexibility with respect to fine grids and coarse partitions [1, 2, 27].

As explained briefly in the introduction, the basic form of the MsRSB method relies on three key ingredients: a coarse partition, a prolongation operator that maps unknowns from the fine grid to the coarse grid, and a restriction operator that maps the flow equations defined on the fine grid to a reduced system of flow equations defined over the coarse partition. Let the fine-scale grid consist of n cells $\{C_i\}$. The coarse grid is then defined as a partition of the fine-scale grid

into m coarse blocks $\{B_j\}$, where each block B_j is a connected set of fine-scale cells defined so that each cell C_i only belongs to one block B_j. Then, the *restriction operator* is represented as a matrix $R \in \mathbb{R}^{m\times n}$, which is a map from the fine grid to the coarse grid. Here, we let R be the control-volume summation operator,

$$R_{ji} = \begin{cases} 1, & \text{if fine cell } i \text{ is part of coarse block } j, \\ 0, & \text{otherwise.} \end{cases}$$

Similarly, we define the *prolongation operator* as a matrix $P \in \mathbb{R}^{n\times m}$, which maps from the coarse grid to the fine grid. The construction of the prolongation operator P will be described in detail below. First, however, we show how R and P can be used to construct a coarse system.

4.1 Coarse system

In each pressure Newton-iteration, we need to solve the linearized pressure system (11). To simplify the notation, we write this system as

$$J\Delta p = r. \tag{13}$$

Instead of solving this linear system directly, we wish to solve a system on the coarse scale to create some approximate coarse solution Δp_c. If we obtain such a solution, it can be mapped back to the fine grid using the prolongation operator to obtain $\Delta p_f = P\Delta p_c$, and we then hope that Δp_f is a good approximation to the true solution Δp.

Replacing Δp with the approximation Δp_f in (13), and then applying the restriction matrix R on both sides, we obtain the following coarse-scale equation simply as

$$(R\,J\,P)\Delta p_c = Rr \qquad \longleftrightarrow \qquad J_c\,\Delta p_c = r_c. \tag{14}$$

which is inexpensive to solve compared with the original fine-scale system provided the coarse partition induces a reasonable reduction in the number of unknowns.

4.2 Basis functions

We only give a very brief description of the construction of the basis functions and refer to [37, 39, 38] for details. The prolongation matrix P is created from a set of localized basis functions, with one basis function associated with each block in the coarse partition, that together form a partition of unity of the domain. In the MsRSB method, the basis functions are computed numerically in an iterative process which is illustrated in Figure 1. Initially, the value of each basis function is set to unity inside the corresponding coarse block, and zero outside. Through repeated iteration of the form,

$$P_j^{\ell+1} = \big(I - \omega D^{-1}A\big)P_j^{\ell} \tag{15}$$

the basis function associated with block B_j is gradually smoothed inside the interaction region surrounding the coarse block until a convergence criterion is met. Here P_j is the jth column of the prolongation operator, A is the fine-scale discretization matrix for a variable-coefficient Poisson operator $\nabla\cdot(K\lambda\nabla)$ that represents the elliptic part of our flow equation, D is a diagonal matrix containing the diagonal entries of the weakly diagonally dominant matrix A, and ω is a relaxation factor. The purpose of the iteration is to make p algebraically smooth, i.e., reduce $\|AP\|_1$ as much as possible. Because each iteration modifies cell values based on the topological neighbors, the support of the basis functions will gradually increase and eventually cover the entire domain. The purpose of the interaction region is to limit the expansion of the basis function outside of the coarse grid block.

4.3 Iterative multiscale solution

Using the prolongation operator introduced above, or any other prolongation operator defined by piecing together localized flow solutions, to map a coarse scale solution to an approximate fine-scale solution, we will inevitably introduce local errors in the fine-scale approximation. These

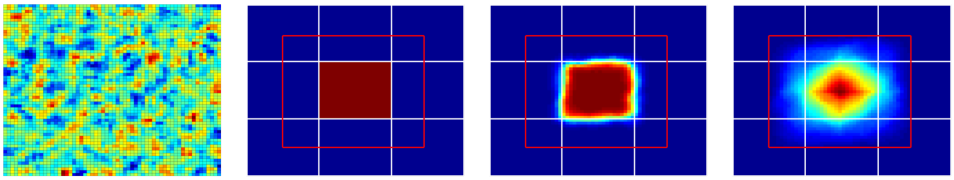

(a) $\log_{10} K$ (b) Initial constant. (c) 10 iterations. (d) Converged.

Figure 1: Iterative construction of a single basis function using restricted smoothing.

high-frequency errors are easy to reduce by using a *smoother*, which can be combined with the multiscale solve to formulate an iterative solver. That is, instead of approximating the solution of (13) by a single coarse solution of (14) prolongated onto the fine grid, we iteratively compute a multiscale increment followed by a few smoothing steps to limit the error of our approximation and hence systematically drive the fine-scale residual toward zero, thus following the ideas of [47, 32, 48, 46]

Let the solution at each multiscale iteration ℓ be denoted x^ℓ, which is an approximation for the solution Δp. At each iteration, define the *defect* as

$$d^\ell = r - Jx^\ell.$$

Let also $y^\ell = S(d^\ell)$ denote a smoother applied to the defect. One iteration then consists of applying the smoothed update, together with a coarse correction,

$$x^{\ell+1} = x^\ell + P\left(J_c^{-1} R(d^\ell - Jy^\ell)\right) + y^\ell. \tag{16}$$

The smoother S in this scheme should be inexpensive, and herein we use a single pass of a preconditioner based on the incomplete LU-factorization with zero fill in (ILU0). One iteration (16) is denoted a *multiscale cycle*.

4.4 Multiscale solution of the nonlinear problem

Let us go back to the nonlinear problem to get an overview of the solution strategy. To aid the explanation, we refer to the flow chart in Figure 2 showing one time step of the nonlinear problem. From the previous time step, we move into the pressure Newton-loop. When assembling the residual equation and the Jacobian matrix, we need to solve for the shear-thinning multiplier, which is done in a nested Newton solver. Once the linearized system (11) is assembled, we do not solve it directly, but instead approximate the pressure update Δp through a number of multiscale cycles (16). When the multiscale cycles have converged to within the prescribed linear tolerance, we have an approximation for the pressure update, and we can continue the nonlinear Newton-loop for the pressure until the nonlinear increment tolerance (12) is met.

The approximate fine-grid pressures computed by the multiscale iteration do not necessarily give a conservative flux field from (8) that can be applied in the transport step. After the convergence of the nonlinear pressure step, we therefore need to solve a set of local Neumann problems to reconstruct a conservative flux field. In this reconstruction step, all pressure-dependent properties used are evaluated using the J matrix from the last multiscale iteration, i.e., the second-last pressure approximation, as discussed in [38], thereby making the problem linear and simpler to solve. Once the flux field is reconstructed, we compute the total flux and move on to solve for saturations and polymer concentration in the transport step. Then the time step is complete, and we can move on to the next time step.

5 Numerical Experiments

The polymer model and sequential solvers outlined above have been implemented using the Matlab Reservoir Simulation Toolbox (MRST) [26, 22, 25, 36], which is an open-source toolbox for rapid

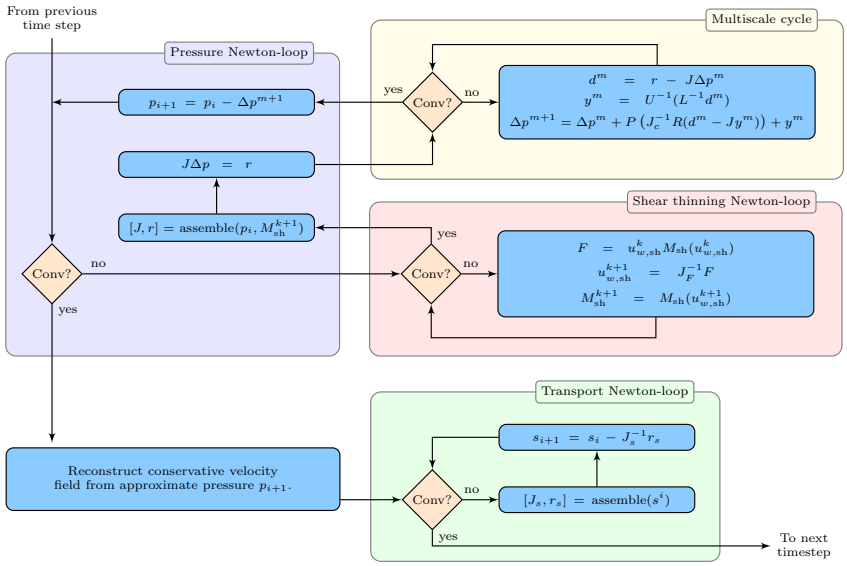

Figure 2: Flow chart of the solution strategy for one time step of the full nonlinear problem. If required, this step can be iterated until the residual of the overall fine-scale flow problem is below a prescribed tolerance.

prototyping of new computational methods and reservoir engineering workflows. In the following, we report a few numerical experiments we have run to verify the sequential solution procedure and our implementation of the polymer model, verify and validate the multiscale method, and assess its computational efficiency.

5.1 Verification: layers of SPE 10

We wish to verify our implementation of the polymer model, our sequential solution procedure, the inclusion of the shear-thinning effect, as well as the use of MsRSB to compute approximate pressures in this setting. To this end, we compare simulations using our sequential solver with a fine-scale or the MsRSB pressure solver with simulations performed with the commercial simulator ECLIPSE 100 [43]. We expect that the correct solutions to be computed by our sequential solvers is relatively close to the solution computed by the fully-implicit commercial simulator if we use sufficiently small time steps.

Model setup

To set up a challenging test case, we will sample petrophysical properties from Model 2 of the 10th SPE Comparative Solution Project [9]. In this model, a single horizontal layer has logical dimensions 60×220 and covers an area of 1200×2200 ft^2. We choose two layers as shown in Figure 3. The bottom layer of the Tarbert formation (Layer 35) has a relatively smooth heterogeneity with a permeability following a lognormal distribution that will be resolved relatively well by most multiscale methods. The bottom layer of the Upper Ness formation (Layer 85) is fluvial and has very long correlation lengths and permeabilities with orders-of-magnitude differences between neighboring cells, which enforces small time steps and makes this layer challenging both for the fully-implicit and the multiscale simulators.

To ensure we are testing all aspects of the polymer model, we choose parameters such that all polymer effects described earlier are included and affect the simulation. In particular, this means

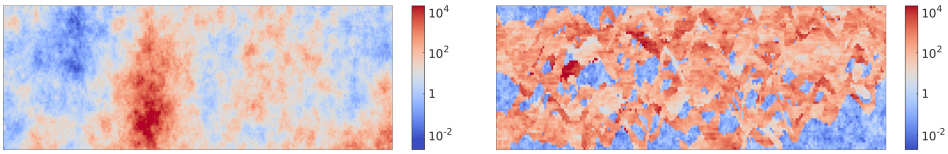

(a) Layer 35 (Tarbert). (b) Layer 85 (Upper Ness).

Figure 3: Permeability field of the SPE 10 layers in logarithmic scale.

choosing a Todd–Longstaff parameter that is neither 0 nor 1, an R_{RF}-factor larger than 1, and dead pore space s_{ipv} larger than zero. The relative permeabilities for oil and water, respectively, are computed from

$$k_{ro}(s_w) = (1-s)^2, \qquad \text{and} \qquad k_{rw}(s_w) = s^2, \qquad \text{where} \qquad s = \frac{s_w - s_{wir}}{1 - s_{or} - s_{wir}}.$$

Here, $s_{or} = 0.2$ is the residual oil saturation and $s_{wir} = 0.2$ is the irreducible water saturation. There is no capillary pressure. The compressibility-factors for oil and water are $c_o = 5 \cdot 10^{-5}$ and $c_w = 1 \cdot 10^{-6}$, respectively, and the rock compressibility is set to $c_r = 1 \cdot 10^{-5}$. The polymer related properties are set as follows: Todd–Longstaff mixing parameter $\omega = 0.5$, residual resistance factor $R_{RF} = 1.1$, dead pore space $s_{\text{ipv}} = 0.05$, rock density $\rho_r = 2000\,\text{kg/m}^3$, and the remaining polymer properties are plotted in Figure 4. These property functions are synthetic, but based on what is found in literature. However, we note that the nonlinearity of the shear-thinning curve has been somewhat exaggerated to ensure we obtain notable effect in the simulations.

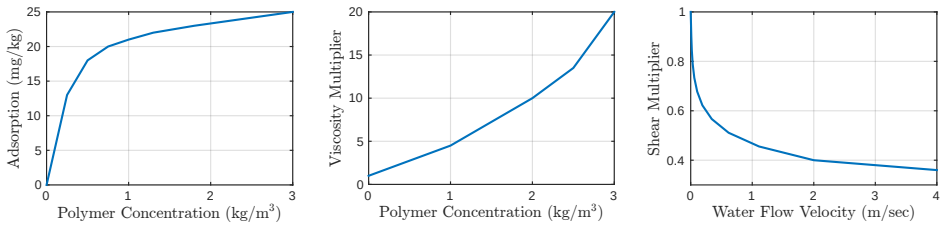

Figure 4: Fluid polymer properties used in the SPE 10 simulations. From the left; adsorption isoterm c_a, viscosity multiplier m_μ from (4), and shear multiplier m_{sh} from (2).

Two wells are placed in opposite corners of the domain, a rate-controlled injector at logical indices $(I, J) = (56, 10)$, and a pressure-controlled producer at $(I, J) = (5, 211)$. The domain is initialized with water saturation $s_w = 0.2$ everywhere. We start injecting water and polymer (at maximum concentration) for 0.1 PV (pore volumes), and continue to inject pure water until a total of 0.5 PV have been injected. For the MsRSB pressure solver, we choose a tolerance of 0.01 and coarsening factor of 10×20, meaning that the coarse grid has dimensions 6×11 which gives square blocks. For both simulators, we used the same time steps, starting with a gradual ramp-up towards a maximum time step of five days.

Results

For each of the two layers, we consider three scenarios: water flooding without polymer, water flooding with polymer having Newtonian rheology, and water flooding with a shear-thinning polymer. Figure 5 shows the water saturation and the polymer concentration at water breakthrough for the latter scenario. It is not possible to distinguish the sequential solution using MsRSB from the fully-implicit reference solution in any of these plots. (The sequential solution with a fine-scale pressure solver is indistinguishable from the MsRSB solution and hence not included for brevity).

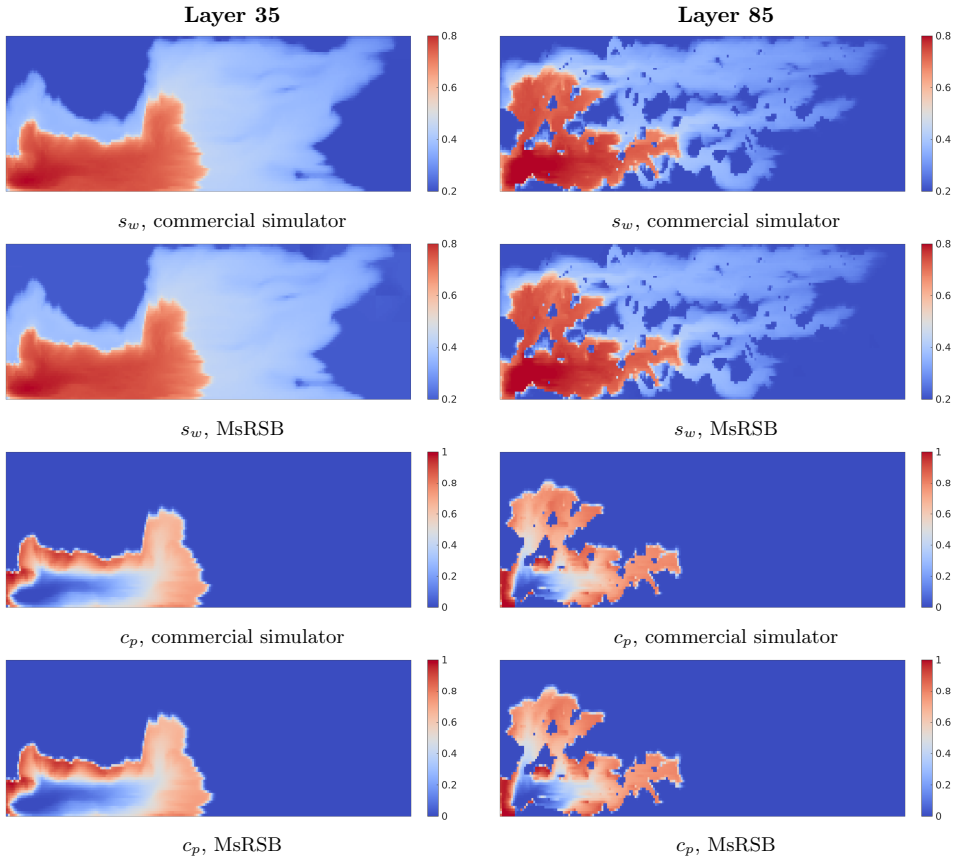

Figure 5: Water saturation and polymer concentration at the point of water break through for the simulations with polymer and shear-thinning effect in the SPE 10 example.

Because of the strong heterogeneity in the SPE 10 subsamples, the discrete system is relatively stiff, and so both the commercial simulator and our sequential simulator need to take small time-steps to converge. As the time-steps are small, we can expect a close agreement between the two simulators even though they use different solution strategies.

Well curves for all these three flow scenarios are shown for both layers in Figure 6. We first note that the bottom-hole pressure (BHP) in the injector is unrealistically high, which is a consequence of injecting a solution of very low mobility in a rate-controlled injector. In reality, the near-well region would fracture or the pressure would be regulated in other ways, but this is not really important for our discussion. The main point we want to make in this example is that we are able to reproduce the reference solution for a case with very strong shear effects.

Comparing the results in Figure 6, both injector BHP and the oil production rate have a near perfect match between the sequential MsRSB solutions and the reference solutions. This is a good indication that the sequential formulation and our implementation are correct. Looking closely at the well-curves, we can observe a slight difference in the oil production when shear-thinning is included. As the other production curves are indistinguishable, this could indicate that there are some small difference in the implementation-details of shear-thinning in the wells, but as we consider the difference in the results negligible, this is not something we pursue.

We also see the clear difference between the polymer flooding with and without shear thinning.

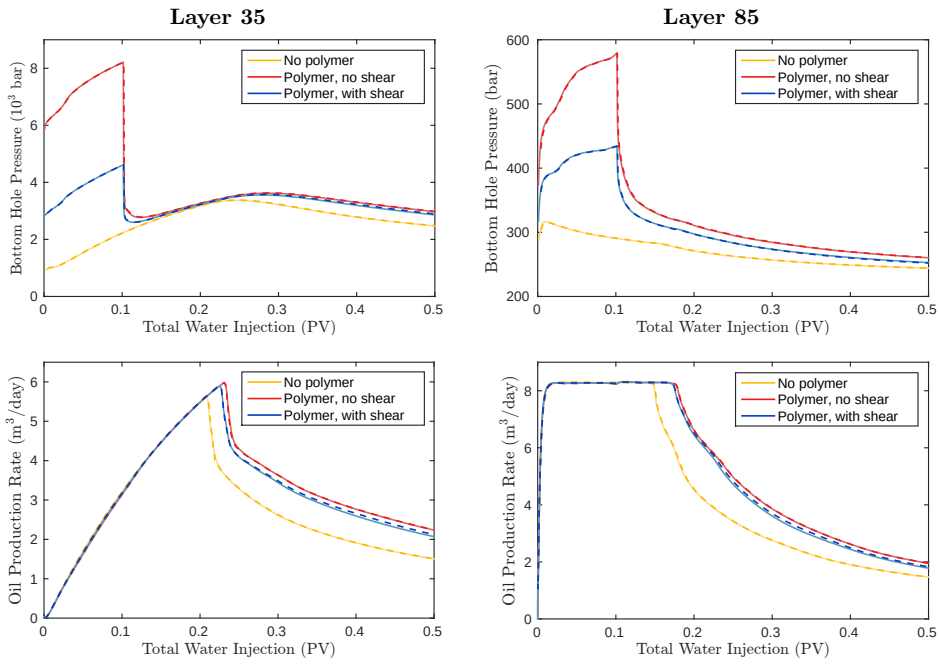

Figure 6: Well solution curves for the SPE 10 example. The fully-implicit reference solutions are plotted in solid lines, while the sequential solutions using MsRSB are plotted in dashed lines on top using slightly stronger colors.

As expected, the injector BHP is lower when shear thinning is included because the shear thinning reduces the viscosity of the injected solution and thus lower pressure is needed to obtain the given injection rate.

5.2 Validation: shallow-marine reservoir

To validate our multiscale method and assess its computational efficiency, we consider a realistic model representing a shallow-marine environments generated by the SAIGUP project [33]; this particular realization can be downloaded using MRST [36]. The permeability field is anisotropic, and the permeability in the x-direction is shown to the left in Figure 7.

Model description

The SAIGUP model consists of 78 720 active cells on an underlying logical grid of size $40 \times 120 \times 20$. Five injection wells and five production wells are placed in the model as shown in Figure 7. The injectors are completed in the lowest 12 layers, while the producers are completed in the top 14 layers. For the fluid properties, we assume densities $\rho_o = 850\,\mathrm{kg/m^3}$ and $\rho_w = 1050\,\mathrm{kg/m^3}$, and viscosities $\mu_o = 5\,\mathrm{cP}$ and $\mu_w = 0.55\,\mathrm{cP}$. The formation volume factors are computed as

$$B_\alpha = B_{\alpha,\mathrm{ref}} e^{-c_\alpha (p - p_{\mathrm{ref}})},$$

where $B_{o,\mathrm{ref}} = 1.06$, $B_{w,\mathrm{ref}} = 1.01$. The compressibility factors are $c_o = 6.7 \times 10^{-5}\,1/\mathrm{bar}$ and $c_w = 4.2 \times 10^{-5}\,1/\mathrm{bar}$ and the reference pressure is $p_{\mathrm{ref}} = 300\,\mathrm{bar}$. The relative permeability and the capillary pressure used are shown in Figure 8. We use the same polymer properties as in the

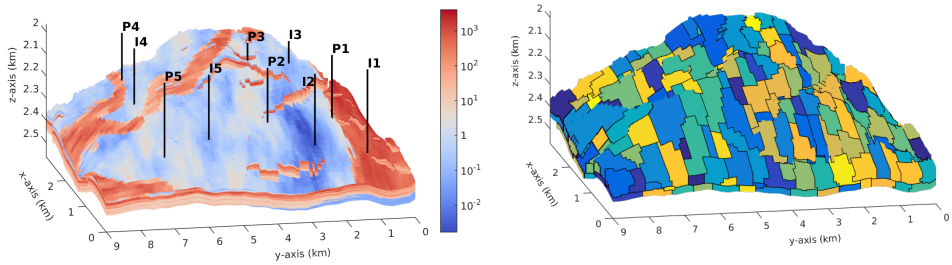

Figure 7: The SAIGUP model. Left: the permeability field in x-direction in units of milli-Darcy on a log-scale, also showing the location of the five injectors and five producers. Right: the METIS partitioning used by the MsRSB method.

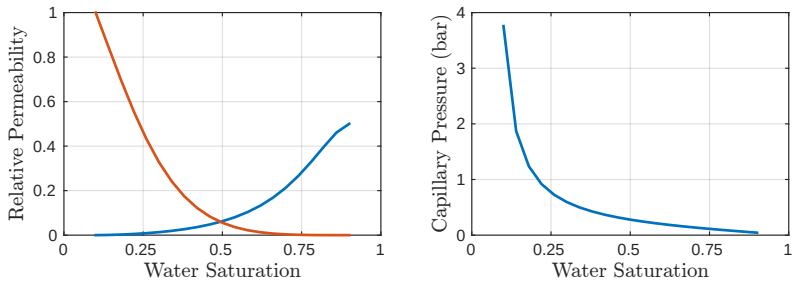

Figure 8: Fluid properties used in the SAIGUP simulations. Left: relative permeability. Right: capillary pressure.

SPE 10 example above, only adjusting the Todd–Longstaff mixing parameter, which is now set to $\omega = 0.8$.

Simulation setup

The domain is initialized with water saturation set to $s_w = 0.1$ everywhere, which is the same as the irreducible water saturation. All the injectors are rate controlled with a constant injection rate of 600 m^3/day, and all the producers operate at a constant pressure of 300 bar. For simplicity, we also let all injectors use the same polymer injection schedule. First, pure water is injected for 1 year, then polymer (at maximum concentration $c_{p,\max}$) is injected for 250 days, followed by continued pure water injection until reaching a total reservoir time of 15 years.

As in the SPE 10 example above, we ran three variations of the simulation: polymer injection with all polymer properties, polymer injection without shear-thinning effect, and finally a pure water injection. Each of these simulations were run using two different sequential simulators. As references we use solutions computed using a direct fine-scale pressure solver, which are compared with the approximate solutions computed using the MsRSB method. Normally, we would set a tolerance for the multiscale iterative solver, but for this example, we choose instead to run a fixed number of multiscale cycles. The coarse grid used by MsRSB is constructed using METIS [19] with transmissibilities for connectivity, where we choose to divide the domain into 250 blocks. The resulting coarse grid is shown in Figure 7.

Results

The final state of the simulation with polymer (including shear-thinning) is shown in Figure 9. Only the layer number 9 (counting from top) is shown in the figure, which is the top-most layer

in which both the injectors and producers are completed. Looking closely at the saturation plot, we see that all producers, except for producer P5, have had water break through. In the polymer concentration plot, we see how the polymer slugs have spread out from the injectors as rings.

Without plotting the well curves for all the wells in the model, we note that when we compare the three different simulation types (polymer, polymer without shear-thinning, and pure water injection), we observe that four of the five producers produce more oil with polymer injection than without, whereas one producer (P5) actually produces less oil when polymer is injected. However, the total production of all wells is notably higher when using polymer. Also, in the four first producers, we observe higher oil production when the shear-thinning effect is neglected in the simulations. This is expected, as shear-thinning lowers the mobility of the polymer solution in high-flow regions, and in this way reduces the desired effect of a more favorable mobility ratio, which in turn reduces the sweep efficiency.

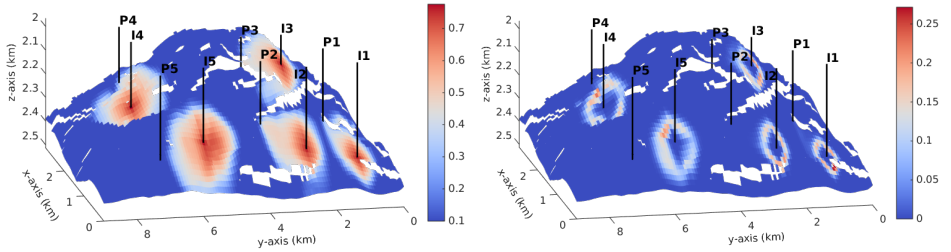

Figure 9: Final state of the SAIGUP example with polymer, showing water saturation (left) and polymer concentration (right) in layer number 9 only.

Accuracy of MsRSB. We have run the simulation using the sequential solver with pressures computed by the MsRSB solver with one, two, and three multiscale cycles. That is, we do not apply a specific tolerance for the convergence of the iterative multiscale solver, but instead choose a fixed number of multiscale-cycles. The well curves computed with the fine-scale pressure solver and the MsRSB solver are virtually identical. Oil production rate and water-cut for one of the five producers (P1) are plotted in Figure 10, where the multiscale solver shown is the one obtained using a single multiscale cycle. The four other producers have equally good match between reference solution and the multiscale solution. Also, performing more multiscale cycles gives even closer match with the reference solution.

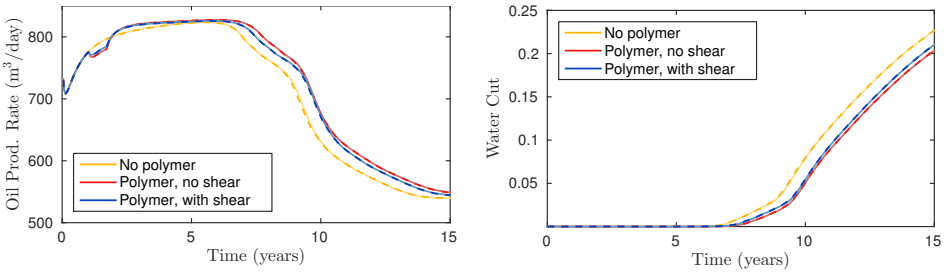

Figure 10: Well solution production well P1 in the SAIGUP example. The reference solutions are plotted are solid lines, while the MsRSB solutions with a single multiscale cycle are plotted as dashed lines on top using slightly stronger colors.

Nonlinear pressure iterations. When using only a few multiscale cycles to solve the *linearized pressure equation*, each linearized solution will not be very accurate and we hence should expect

to use a higher number of iterations to reduce the residual of the *nonlinear pressure equation* below the prescribed tolerance. In all the multiscale simulations above, we used the same value $\varepsilon_p = 10^{-3}$ for the nonlinear pressure convergence criterion (12). In Figure 11, we compare the number of nonlinear pressure iterations throughout the simulations for the different simulations. As expected, the number of nonlinear iterations increases as the number of multiscale cycles goes down. Likewise, the sequential simulation with exact fine-scale solver requires less iterations than when using the approximate MsRSB solver. Especially, we note an increase in the number of iterations after the polymer injection has stopped.

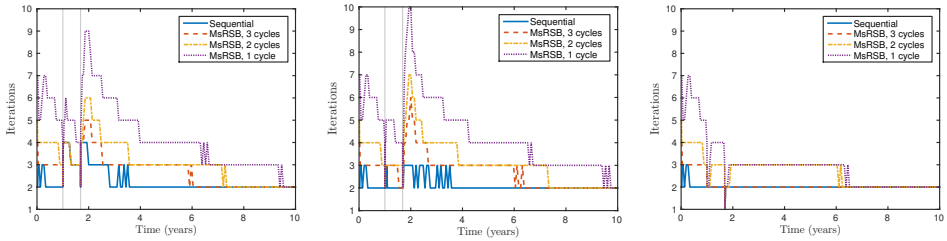

(a) Polymer (b) No shear thinning (c) Pure water injection

Figure 11: Nonlinear pressure iterations for the SAIGUP example; comparison of the sequential reference solver and multiscale solver with different number of multiscale cycles. Vertical gray lines indicate start and stop of polymer injection.

Computational cost. Even though computational efficiency and code optimization is not the focus of this study, it is still of interest to consider the runtime for the different simulations. Of particular interest is the time spent in the linear pressure solver, as this is where we observe the speedup from using the MsRSB method. The CPU-time used for each simulation is split into the different solution parts and shown in Figure 12. We first note that each timing result here is taken from a single simulation, and is not an average of multiple runs. Also, the timing is not performed in a controlled environment, so other processes running on the computer may influence the performance. However, more controlled timing tests are not expected to change the overall picture.

The timing for each simulation is divided into four categories: time spent in linear pressure solver, pressure reconstruction solver, linear transport solver, and computational overhead coming from other parts of the code. As explained in more detail in [38], the MRST implementation has a significant overhead in the evaluation of fluid properties and assembly of linear systems that most likely can be eliminated or significantly reduced if the sequential simulators were implemented in a computer environment optimized for performance rather than prototyping flexibility. Hence, only the first three categories are shown in Figure 12. As expected, the total simulation time is considerably higher for the first two simulations, where polymer is present in the system, compared to the pure oil-water system. Also, we observe that the runtime for polymer simulations *with* shear-thinning is notably higher than simulations without as a result of the extra calculations performed to compute the shear thinning in each pressure nonlinear iteration.

For each of the three types of simulation, we observe similar difference among the solvers; the fine-scale AGMG pressure solver spends a considerably longer time solving fine-scale pressure system than the multiscale solver spends solving the coarse-scale pressure system and reconstructing fine-scale flux fields field. Looking only at the time for the pressure solution, the multiscale solver is between 6 and 8 times faster than the fine-scale solver.

5.3 Validation: model with faults and adaptive gridding

To demonstrate the ability to run simulations on more complex grid, we construct a synthetic model with radial well refinement and faults. In this example, which is inspired by test case used in [39],

we wish to validate that our sequential solver with approximate pressure solution converges to the fully-implicit solution, and observe how the solution changes with different tolerance levels. For the iterative setup of the MsRSB method, we apply the MS-ILU0 as a preconditioner for GMRES as explained in [39].

Model description and simulation setup

We consider a 2D rectangular reservoir model having four sealing faults and petrophysical properties sampled from the tenth layer of the SPE 10 model. To ensure that we have significant non-Newtonian rheology throughout the whole reservoir, we scale the physical dimensions to be $73 \times 134\,\mathrm{ft}^2$. An injector and a producer are placed at opposite sides of the domain. The reservoir is gridded by a PEBI-mesh that adapts to the faults, has radial refinement at the wells, but is elsewhere regular. The resulting grid consists of approximately 3800 cells and is shown in Figure 13. We use METIS [19] to perform a black-box partition into 24 coarse blocks. As seen in the right plot in Figure 13, the result is a fully unstructured partition that gives no special treatment to the near-well refinements, but manages to preserve three of the faults and most of the fourth fault as block boundaries. In [39], we consider a user-adapted partition that preserves more of the structure of the fine-scale grid in the sense that it is radially refined near the wells, respects the faults, and is more or less regular elsewhere. Using an adapted grid will generally result in a more accurate multiscale solution. The METIS partition, on the other hand, has more coarse-block connections and will therefore result in a faster decay as the fine-scale residual is driven towards zero in an iterative multiscale solver.

We assume incompressible fluids with viscosities $\mu_o = 10\,\mathrm{cP}$ and $\mu_w = 1\,\mathrm{cP}$. The relative permeabilities and the capillary pressure are shown in Figure 14, while the polymer property curves are shown in Figure 15. In addition, we assume a Todd–Longstaff mixing parameter $\omega = 0.9$, residual resistance factor $R_{RF} = 1.05$, dead pore space $s_{\mathrm{ipv}} = 0.02$, and rock density $\rho_r = 2000\,\mathrm{kg/m}^3$. The producer is set to be pressure-controlled at 200 bar, while the injector is rate-controlled with constant rate. A total of one pore volume of water is injected over a simulation time of 5 years. During the first 0.05 pore volumes, polymers are added to the injection water, and then the remaining simulation has pure water injection.

Results

We run the simulation using three different solvers in MRST; the fully implicit solver, the sequential solver with exact pressures, and the sequential solver with approximate pressures computed by MsRSB. The fully implicit solution at water breakthrough is shown in Figure 16, where we clearly observe how the faults largely dictate the flow pattern. As in previous examples, we do not observe any difference in the saturation or concentration plots comparing the fully-implicit solution with the different sequential solutions. Because of this, we only plot the fully-implicit solution here.

Accuracy of pressure solution

There are two parameters that control the accuracy of the pressure approximation computed by the multiscale method: the multiscale tolerance that controls how accurately the iterative MsRSB method approximates each linearized equation, and the nonlinear pressure tolerance that controls how accurately we approximate the *nonlinear* pressure equation.

Figure 17 shows the difference in water cut between the sequential solver with exact pressure updates and a very low nonlinear pressure tolerance, and the MsRSB solution with different multiscale tolerances and different nonlinear pressure tolerances. As the nonlinear pressure tolerance is lowered, we observe the well solution approaches the solution using exact pressure updates. However, the different multiscale tolerances give approximately the same accuracy, meaning that even at a low multiscale tolerance, the flux field is well approximated.

An important question is to what extent the accuracy of the multiscale approximation affects the convergence of the nonlinear iterations. Figure 18 reports the average number of nonlinear iterations for a test matrix of four different multiscale tolerances (10^{-n}, $n = 1, \ldots, 4$) and five

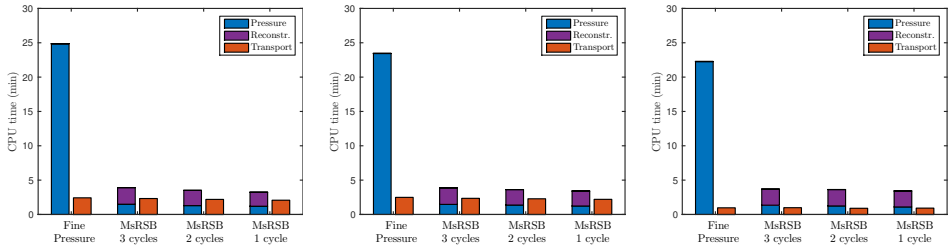

(a) Polymer (b) No shear thinning (c) Pure water injection

Figure 12: Timing results for the SAIGUP example.

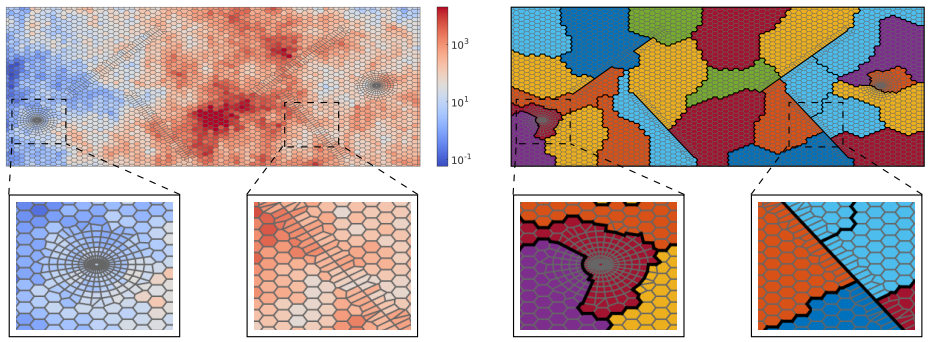

Figure 13: Grid, permeability field and coarse partitioning used by MsRSB.

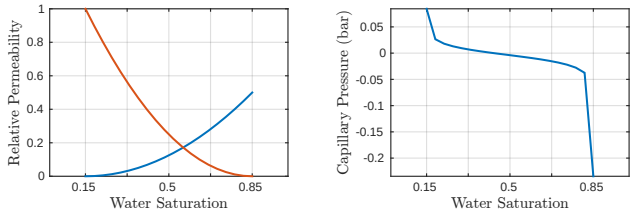

Figure 14: Fluid properties used with the PEBI model: relative permeability (left) and capillary pressure (right).

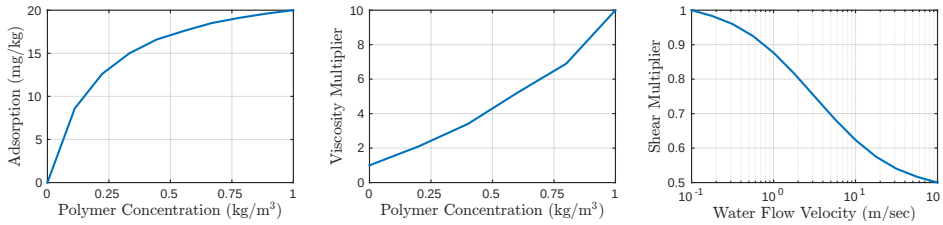

Figure 15: Fluid polymer properties used with the PEBI model: adsorption isoterm c_a (left), viscosity multiplier m_μ from (4) (middle), and shear multiplier m_{sh} from (2) (right).

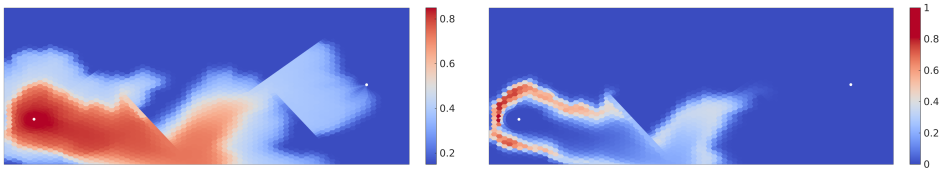

Figure 16: Fully-implicit solution at time of water breakthrough for the PEBI model; water saturation shown to the left and polymer concentration to the right.

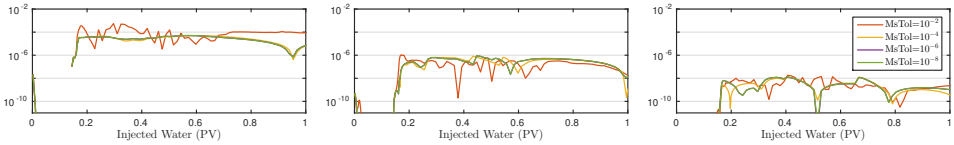

(a) $\varepsilon_p = 10^{-2}$ (b) $\varepsilon_p = 10^{-4}$ (c) $\varepsilon_p = 10^{-6}$

Figure 17: Water cut for MsRSB solver relative to the sequential solver with exact pressure. Results shown for different nonlinear incremental pressure tolerance ε_p as defined in (12), and different multiscale tolerances.

different nonlinear tolerances (10^{-n}, $m = 0, \ldots, 4$). Note that the nonlinear tolerance is an *incremental* pressure tolerance, as defined in (12), which means that the pressure has converged when the approximate multiscale increments are sufficiently small. Two trends can be observed: At least for this particular example, the pressure converges very quickly, and more than two pressure iteration on average is only required for a incremental pressure tolerances of 10^{-3} or smaller, even when using a relatively coarse multiscale tolerance of 0.1. Secondly, for small nonlinear tolerances, it seems like a multiscale tolerance of 10^{-3} to 10^{-2} is sufficient to ensure convergence in less 2.5 iterations on average. This is a quite promising result: If only a few iterations are needed in the multiscale method, there is a significant potential for reducing computational speed compared to a fine-scale solver.

Outer iterations on each time step

As explained above, we may extend the sequential solver by using outer iterations on each time step to make it converge to the solution of a fully-implicit formulation. That is: after the transport equation has converged, we compute the residual of the pressure equation using the updated saturation and concentration. If the pressure residual is larger than the prescribed tolerance, the pressure and transport equations are solved again at that same time step. This is repeated until convergence.

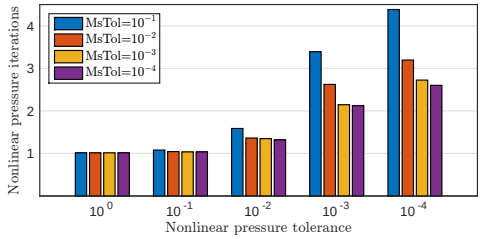

Figure 18: Average number of nonlinear pressure iterations through a simulation as a function of the nonlinear incremental pressure tolerance ε_p as defined in (12). The different colors represent different multiscale tolerances.

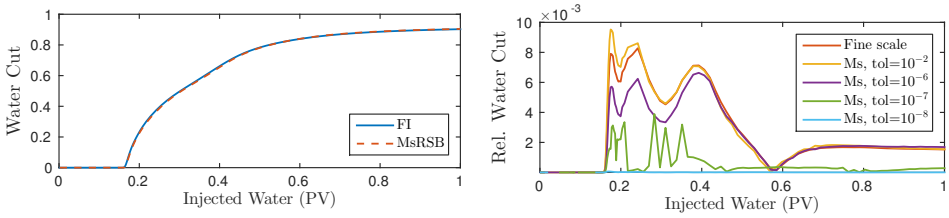

Figure 19: The left plot shows the water-cut curves computed by the fully-implicit solver and the sequential MRST solver with no outer iterations and multiscale tolerance 0.01. The right plot shows discrepancy between the fully-implicit solution and the sequential simulator with no iterations and a direct fine-scale solver for the linearized pressure systems, and with different tolerances on the outer iterations and MsRSB as an approximate solver for the linearized pressure systems.

Applying outer iterations to our sequential solver, we expect the solution to converge to the fully-implicit solution as the tolerance level is decreased. To verify this, we compare the well solutions obtained by the different solvers. To the left in Figure 19, we show the water cut computed by the fully-implicit solver together with the water cut computed by the sequential MsRSB solver without outer iterations and with multiscale tolerance set to 0.01. We see that even without any outer iterations, the two solutions are closely matched.

The right plot in in Figure 19 shows how we can make the approximate multiscale solution converge to the solution computed by a conventional fully-implicit simulator by adjusting the tolerance on the outer iterations. In the figure, "fine scale" refers to the sequential simulator with a direct solver for the linearized pressure equations and no outer iterations, whereas the other solutions are multiscale solutions with different tolerances for the outer iterations. All these simulations are run using the same time steps to be able to compare the results directly. With a high tolerance on the outer iterations, the MsRSB solver is in close agreement with the solution computed using an exact solver for the linearized pressure equations. Likewise, as the tolerance for the outer iterations is decreased, the multiscale solver converges to the fully-implicit solution as expected.

6 Conclusion

We have developed a sequential solution procedure for simulating polymer flooding with shear effects and extended the formulation with a multiscale solver to accelerate the computation of the pressure part of the flow problem. The multiscale solver has the appealing feature that it can provide mass-conservative flux fields without having to converge the linearized pressure residuals to machine precision. In the resulting simulator, we can therefore trade accuracy for computational efficiency by prescribing coarse tolerances on the linear and/or nonlinear pressure updates. On the other hand, the simulator can be made to reproduce the results of a fully-implicit simulator by prescribing low tolerances for the linear and nonlinear pressure updates and/or possibly adding outer iterations on each time step to run the simulator iterated fully-implicit mode.

Our prototype implementation of the multiscale polymer simulator has been verified against the commercial ECLIPSE100 simulator to demonstrate the correctness of the sequential formulation, as well as the robustness of the MsRSB method. Likewise, we have illustrated that the multiscale method can efficiently resolve the highly nonlinear flow physics of a shear-thinning polymer flooding in a reservoir model with industry-standard geological complexity. Seen from the point of view of a multiscale method, this demonstrates the versatility of the MsRSB method.

Acknowledgments

The research is partly funded by VISTA, which is a basic research programme funded by Statoil and conducted in close collaboration with The Norwegian Academy of Science and Letters. The authors would also like to acknowledge funding by Schlumberger Information Solutions and by the Research Council of Norway under grant no. 226035.

References

[1] J. E. Aarnes, S. Krogstad, and K.-A. Lie. Multiscale mixed/mimetic methods on corner-point grids. *Comput. Geosci.*, 12(3):297–315, 2008.

[2] F. O. Alpak, M. Pal, and K.-A. Lie. A multiscale method for modeling flow in stratigraphically complex reservoirs. *SPE J.*, 17(4):1056–1070, 2012.

[3] A. M. AlSofi and M. J. Blunt. Streamline-based simulation of non-Newtonian polymer flooding. *SPE J.*, 15(4):895–905, 2010.

[4] T. Arbogast. Implementation of a locally conservative numerical subgrid upscaling scheme for two-phase Darcy flow. *Comput. Geosci.*, 6(3-4):453–481, 2002.

[5] M. Babaei and P. R. King. A modified nested-gridding for upscaling–downscaling in reservoir simulation. *Transp. Porous Media*, 93(3):753–775, July 2012.

[6] M. Babaei and P. R. King. An upscaling–static-downscaling scheme for simulation of enhanced oil recovery processes. *Transp. Porous Media*, 98(2):465–484, March 2013.

[7] Y. Brenier and J. Jaffré. Upstream differencing for multiphase flow in reservoir simulation. *SIAM J. Numer. Anal.*, 28(3):685–696, 1991.

[8] Z. Chen and T. Y. Hou. A mixed multiscale finite element method for elliptic problems with oscillating coefficients. *Math. Comp.*, 72:541–576, 2003.

[9] M. A. Christie and M. J. Blunt. Tenth SPE comparative solution project: A comparison of upscaling techniques. *SPE Reserv. Eval. Eng.*, 4(4):308–317, August 2001.

[10] T. Clemens, J. Abdev, and M. R. Thiele. Improved polymer-flood management using streamlines. *SPE J.*, 14(2):171–181, 2011.

[11] M. Cusini, A. A. Lukyanov, J. Natvig, and H. Hajibeygi. Constrained pressure residual multiscale (CPR-MS) method for fully implicit simulation of multiphase flow in porous media. *J. Comput. Phys.*, 299:472–486, 2015.

[12] Y. Efendiev, J. Galvis, and T. Y. Hou. Generalized multiscale finite element methods (GMsFEM). *J. Comput. Phys.*, 251:116–135, 2013.

[13] Y. Gautier, M. J. Blunt, and M. A. Christie. Nested gridding and streamline-based simulation for fast reservoir performance prediction. *Comput. Geosci.*, 3(3):295–320, 1999.

[14] H. Hajibeygi, G. Bonfigli, M. A. Hesse, and P. Jenny. Iterative multiscale finite-volume method. *J. Comput. Phys*, 227(19):8604–8621, 2008.

[15] H. Hajibeygi and P. Jenny. Adaptive iterative multiscale finite volume method. *J. Comput. Phys*, 230(3):628–643, 2011.

[16] H. Hoteit and A. Chawathé. Making field-scale chemical EOR simulations a practical reality using dynamic gridding. In *SPE EOR Conference at Oil and Gas West Asia, 31 March–2 April, Muscat, Oman*, 2014. SPE 169688-MS.

[17] T. Hou and X.-H. Wu. A multiscale finite element method for elliptic problems in composite materials and porous media. *J. Comput. Phys.*, 134:169–189, 1997.

[18] P. Jenny, S. H. Lee, and H. A. Tchelepi. Multi-scale finite-volume method for elliptic problems in subsurface flow simulation. *J. Comput. Phys.*, 187:47–67, 2003.

[19] G. Karypis and V. Kumar. A fast and high quality multilevel scheme for partitioning irregular graphs. *SIAM J. Sci. Comput.*, 20(1):359–392, 1999.

[20] F. Koyassan Veedu and M. D. G. A. Pope. Scaleup methodology for chemical flooding. In *SPE Annual Technical Conference and Exhibition, 19-22 September, Florence, Italy*, 2010. SPE 135543-MS.

[21] A. Kozlova, Z. Li, J. R. Natvig, S. Watanabe, Y. Zhou, K. Bratvedt, and S. H. Lee. A real-field multiscale black-oil reservoir simulator. In *SPE Reservoir Simulation Symposium, 23-25 February, Houston, Texas, USA*, 2015. SPE 173226-MS.

[22] S. Krogstad, K.-A. Lie, O. Møyner, H. M. Nilsen, X. Raynaud, and B. Skaflestad. MRST-AD – an open-source framework for rapid prototyping and evaluation of reservoir simulation problems. In *SPE Reservoir Simulation Symposium, 23–25 February, Houston, Texas*, 2015.

[23] S. Krogstad, K.-A. Lie, H. M. Nilsen, J. R. Natvig, B. Skaflestad, and J. E. Aarnes. A multiscale mixed finite-element solver for three-phase black-oil flow. In *SPE Reservoir Simulation Symposium, The Woodlands, TX, USA, 2–4 February 2009*, 2009.

[24] L. W. Lake. *Enhanced Oil Recovery*. Society of Petroleum Engineers, reprint 2010 edition, 1989.

[25] K.-A. Lie. *An Introduction to Reservoir Simulation Using MATLAB: User guide for the Matlab Reservoir Simulation Toolbox (MRST)*. SINTEF ICT, `http://www.sintef.no/Projectweb/MRST/publications`, 2nd edition, Dec 2015.

[26] K.-A. Lie, S. Krogstad, I. S. Ligaarden, J. R. Natvig, H. Nilsen, and B. Skaflestad. Open-source MATLAB implementation of consistent discretisations on complex grids. *Comput. Geosci.*, 16:297–322, 2012.

[27] K.-A. Lie, J. R. Natvig, S. Krogstad, Y. Yang, and X.-H. Wu. Grid adaptation for the Dirichlet–Neumann representation method and the multiscale mixed finite-element method. *Comput. Geosci.*, 18(3):357–372, 2014.

[28] K.-A. Lie, H. M. Nilsen, A. F. Rasmussen, and X. Raynaud. An unconditionally stable splitting method using reordering for simulating polymer injection. In *ECMOR XIII – 13th European Conference on the Mathematics of Oil Recovery, Biarritz, France, 10-13 September 2012*, 2012. B25.

[29] K.-A. Lie, H. M. Nilsen, A. F. Rasmussen, and X. Raynaud. Fast simulation of polymer injection in heavy-oil reservoirs based on topological sorting and sequential splitting. *SPE J.*, 19(6):991–1004, 2014.

[30] K. Lipnikov, J. D. Moulton, and D. Svyatskiy. A multilevel multiscale mimetic (m^3) method for two-phase flows in porous media. *J. Comput. Phys.*, 227(14):6727–6753, 2008.

[31] I. Lunati and S. H. Lee. An operator formulation of the multiscale finite-volume method with correction function. *Multiscale Model. Simul.*, 8(1):96–109, 2009.

[32] I. Lunati, M. Tyagi, and S. H. Lee. An iterative multiscale finite volume algorithm converging to the exact solution. *J. Comput. Phys.*, 230(5):1849–1864, 2011.

[33] T. Manzocchi et al. Sensitivity of the impact of geological uncertainty on production from faulted and unfaulted shallow-marine oil reservoirs: objectives and methods. *Petrol. Geosci.*, 14(1):3–15, 2008.

[34] O. Møyner and K.-A. Lie. The multiscale finite-volume method on stratigraphic grids. *SPE J.*, 19(5):816–831, 2014.

[35] O. Møyner and K.-A. Lie. A multiscale two-point flux-approximation method. *J. Comput. Phys.*, 275:273–293, 2014.

[36] The MATLAB Reservoir Simulation Toolbox, MRST 2015a, May 2015. `www.sintef.no/MRST`.

[37] O. Møyner and K.-A. Lie. A multiscale method based on restriction-smoothed basis functions suitable for general grids in high contrast media. In *SPE Reservoir Simulation Symposium held in Houston, Texas, USA, 23-25 February 2015*, 2015.

[38] O. Møyner and K.-A. Lie. A multiscale restriction-smoothed basis method for compressible black-oil models. 2015.

[39] O. Møyner and K.-A. Lie. A multiscale restriction-smoothed basis method for high contrast porous media represented on unstructured grids. *J. Comput. Phys.*, 304:46–71, 2016.

[40] J. R. Natvig and K.-A. Lie. Fast computation of multiphase flow in porous media by implicit discontinuous Galerkin schemes with optimal ordering of elements. *J. Comput. Phys.*, 227(24):10108–10124, 2008.

[41] J. R. Natvig, B. Skaflestad, F. Bratvedt, K. Bratvedt, K.-A. Lie, V. Laptev, and S. K. Khataniar. Multiscale mimetic solvers for efficient streamline simulation of fractured reservoirs. *SPE J.*, 16(4):880–888, 2011.

[42] M. Pal, S. Lamine, K.-A. Lie, and S. Krogstad. Validation of the multiscale mixed finite-element method. *Int. J. Numer. Meth. Fluids*, 77(4):206–223, 2015.

[43] Schlumberger. *ECLIPSE 2013.2 Technical Description*, 2013.

[44] F. I. Stalkup, L. L. Lo, and R. H. Dean. Sensitivity to gridding of miscible flood predictions made with upstream differenced simulators. In *SPE/DOE Enhanced Oil Recovery Symposium, 22-25 April, Tulsa, Oklahoma*, 1990. SPE 20178-MS.

[45] M. Todd and W. Longstaff. The development, testing, and application of a numerical simulator for predicting miscible flood performance. *J. Pet. Technol.*, 24(7):874–882, July 1972.

[46] Y. Wang, H. Hajibeygi, and H. A. Tchelepi. Algebraic multiscale solver for flow in heterogeneous porous media. *J. Comput. Phys.*, 259:284–303, 2014.

[47] H. Zhou and H. A. Tchelepi. Operator-based multiscale method for compressible flow. *SPE J.*, 13(2):267–273, 2008.

[48] H. Zhou and H. A. Tchelepi. Two-stage algebraic multiscale linear solver for highly heterogeneous reservoir models. *SPE J.*, 17(2):523–539, 2012.

Paper V

A Well-Posed Model of Inaccessible Pore Volume for Polymer

Sindre Tonning Hilden, Halvor Møll Nilsen, and Xavier Raynaud

Submitted

A Well-Posed Model of Inaccessible Pore Volume for Polymer

Sindre T. Hilden Halvor Møll Nilsen Xavier Raynaud

Preprint, March 29, 2016

Abstract

Inaccessible pore volume, also known as dead pore space, is used when simulating enhanced oil recovery by polymer injection. We show that a widely used model for inaccessible pore volume can lead to an ill-posed problem, resulting in unphysical results. By considering shock-solutions, we derive a necessary condition for an inaccessible pore volume model, and based on a heuristic understanding of relative permeability, we find a modified model which satisfies this condition. Also, for the numerical examples we run, the polymer concentration is between zero and the maximum allowed polymer concentration for the modified model, which is not the case for the standard model. This enables a more stable implementation of the highly nonlinear system. The modification can easily be implemented in existing reservoir simulators and can be used for a wide range of polymer models.

1 Introduction

One of the primary methods of enhanced oil recovery is polymer injection, in which polymer molecules are added to the injected water. This is done to reduce the mobility of the injected solution and create a more favorable mobility ratio between the water and the oil in place. In physical experiments, the polymer is observed to travel faster through the water than a passive tracer. The common explanation for the increased velocity is that the smallest pores are not accessible to the polymer because of the large size of the polymer molecules [8]. As the flow rate is greater in the large pores, the effective speed of the polymer becomes higher than the average speed of water. The region of the pore space which is not accessible to polymer is known as the *inaccessible pore volume* (IPV), or the *dead pore space* (DPS).

In reservoir-scale simulations of polymer flooding, IPV is often used as a parameter in the model equations. We show that the most common IPV model can lead to unphysical solutions where polymer travels through a water front, and invades regions without water. This was noticed in [1], and an alternative model based on percolation principles was proposed for the case where the inaccessible pore volume is smaller than the irreducible water saturation. The shortcoming in the conventional model and the limitation in the percolation based model motivate us to create an IPV model which is robust and does not impose any limitations on the value of the inaccessible pore volume.

By first considering shock solutions of the one-dimensional equations, we find a necessary condition that the IPV model must fulfill for the equations to be well-posed. This condition guides us when constructing an alternative model. Based on a heuristic physical understanding of relative permeability, we present a modification of the conventional IPV model which leads to well-posed equations. Our modification reduces to the percolation based model of [1] in the case where the inaccessible pore volume is smaller than the irreducible water saturation, but our model also extends to the general case. To observe how the different IPV models behave in practice, we run both one- and two-dimensional numerical simulations with varying input parameters. The examples help to illustrate potential problems with the different models.

2 Mathematical Formulation

We consider a two-phase oil and water model, in which polymer in addition can be part of the water phase. First, the equations are presented without the effect of inaccessible pore volume (IPV), and then different IPV models are discussed below. The governing equations without IPV are

$$\frac{\partial}{\partial t}(\rho_\alpha \phi s_\alpha) + \nabla \cdot (\rho_\alpha \mathbf{v}_\alpha) = 0, \qquad \alpha \in \{w, o\}, \tag{1a}$$

$$\frac{\partial}{\partial t}(\rho_w \phi s_w c) + \nabla \cdot (c\rho_w \mathbf{v}_{wp}) = 0, \tag{1b}$$

with porosity ϕ, phase densities ρ_α, phase saturations s_α, and polymer concentration c, which is given in units of mass per volume of water. The Darcy velocities are given by

$$\mathbf{v}_o = -\frac{k_{ro}}{\mu_o}\mathbf{K}(\nabla p - \rho_o g \nabla z), \tag{2a}$$

$$\mathbf{v}_w = -\frac{k_{rw}}{\mu_{w,\text{eff}}}\mathbf{K}(\nabla p - \rho_w g \nabla z), \tag{2b}$$

$$\mathbf{v}_{wp} = -\frac{k_{rwp}}{\mu_{p,\text{eff}}}\mathbf{K}(\nabla p - \rho_w g \nabla z). \tag{2c}$$

Here it is assumed that the presence of polymer does not affect the oil phase, nor any pressure or densities. Also, the relative permeabilities are independent of the polymer concentration. The viscosity of a fully mixed solution of water and polymer is denoted $\mu_m(c)$, and the effective polymer viscosity is given by

$$\mu_{p,\text{eff}} = \mu_m(c)^\omega \mu_p^{1-\omega} \quad \text{with} \quad \mu_p = \mu_m(c_{\max}).$$

The viscosity of the partially mixed water is given in a similar way by

$$\mu_{w,e} = \mu_m(c)^\omega \mu_w^{1-\omega}.$$

and the effective water viscosity $\mu_{w,\text{eff}}$ is defined by interpolating linearly between the inverse of the effective polymer viscosity and the partially mixed water viscosity

$$\frac{1}{\mu_{w,\text{eff}}} = \frac{1 - c/c_{\max}}{\mu_{w,e}} + \frac{c/c_{\max}}{\mu_{p,\text{eff}}}.$$

Other polymer effects such as adsorption and shear-thinning are ignored herein for simplicity.

3 Existing Inaccessible Pore Volume Models

3.1 Conventional Model

Polymer cannot reach the smallest pores and, as a result, the effective pore volume for the polymer solution is smaller than the pore volume of the rock. This effect has been modeled in [7] by replacing the polymer equation (1b) with

$$\frac{\partial}{\partial t}\Big(\rho_w(1 - s_{\text{ipv}})\phi s_w c\Big) + \nabla \cdot (c\rho_w \mathbf{v}_{wp}) = 0,$$

where $s_{\text{ipv}} \in [0, 1]$ denotes the fraction of the pore volume that is not accessible to polymer. The introduction of inaccessible pore volume has the effect to increase the mobility of the polymer solution. To more strongly emphasize this, and also for the purpose of comparison with methods presented below, the equation above can be re-written as

$$\frac{\partial}{\partial t}\Big(\rho_w \phi s_w c\Big) + \nabla \cdot (c\rho_w \gamma \mathbf{v}_{wp}) = 0, \tag{3}$$

where the constant velocity enhancement factor γ is given by

$$\gamma = \frac{1}{1 - s_{\text{ipv}}}. \tag{4}$$

This simple model is used in several reservoir simulators [4, 5, 10, 12]. However, this conventional model yields instabilities because it allows polymer to travel independent of the concentration and the water content, which can result in the polymer traveling beyond the existence of water. We give an example to illustrate this.

Example: Instability of the Conventional IPV Model. The instability of the conventional model can be illustrated by the following example. Consider a one-dimensional horizontal model, with incompressible fluids and incompressible rock of constant permeability (say $K = 1$) and constant porosity (say $\phi = 1$). Let the relative permeabilities be equal and linear for oil, water, and water with polymer, such that $k_{ro}(s_o) = s_o$, and $k_{rw}(s_w) = k_{rwp}(s_w) = s_w$. Also, let $\mu_m(c)$ be a constant, and set $\mu_m(c) = \mu_w = \mu_o = \mu$, which implies $\mu_{w,\text{eff}} = \mu$. For incompressible 1D flow with constant pressure-drop, the velocity is constant, and we can assume $v_w = 1$ without any loss of generality. The governing equations with the conventional IPV model then simplifies to

$$\frac{\partial}{\partial t}\begin{bmatrix} s_w \\ s_o \\ (1 - s_{\text{ipv}})z \end{bmatrix} + \frac{\partial}{\partial x}\begin{bmatrix} s_w \\ s_o \\ z \end{bmatrix} = 0, \tag{5}$$

where z denotes the product $s_w c$. Consider the domain $x \in [-\frac{1}{2}, \frac{1}{2}]$ and boundary conditions given by $s_w(t, -0.5) = 1$ and $z(t, -0.5) = c_L$. The initial state is given by

$$s_w(0, x) = H(x), \quad c(0, x) = c_L H(x)$$

where

$$H(x) = \begin{cases} 1 & \text{for } x \leq 0, \\ 0 & \text{for } x > 0. \end{cases}$$

We can solve for s_w and z in (5) by using the method of characteristics to obtain

$$s_w(t, x) = H(x - t), \quad z(t, x) = c_L H(x - v_p t),$$

where $v_p = 1/(1 - s_{\text{ipv}})$. The solution at time $t_1 > 0$ is depicted in Figure 1 in the case where $s_{\text{ipv}} > 0$. At the point $x_1 = v_p t_1$, we have $z(t_1, x_1) = c_L$ and, as $s_{\text{ipv}} > 0$, the water saturation is $s_w(t_1, x_1) = 0$. It follows that the polymer concentration at this point, $c(t_1, x_1) = z(t_1, x_1)/s_w(t_1, x_1)$, is infinite.

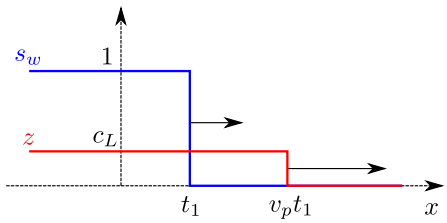

Figure 1: Solutions of the one-dimensional problem (5).

3.2 Percolation Based Velocity Enhancement Model

The conventional IPV model has a constant velocity enhancement factor γ, as given by (4). It was above that the constant conventional velocity enhancement factor leads to an ill-posed problem.

This was also shown in [1], and it was suggested instead, based on a percolation model, to use a saturation-dependent function $\gamma(s_w) = s_w/(s_w - s_w^*)$, where s_w^* is a threshold saturation. Based on the argument that for a water-wet media, the water will enter the smallest pores first, the threshold saturation s_w^* is the saturation that is needed to fill the pores before polymer is allowed to enter. This definition is similar to the definition of s_{ipv}, and for the purpose of comparison, we assume herein that $s^* = s_{\text{ipv}}$. The percolation-based velocity enhancement factor from [1] is thus written

$$\gamma(s_w) = \frac{s_w}{s_w - s_{\text{ipv}}}. \tag{6}$$

In the numerical simulations in [11], the authors use a fractional flow formulation and the equation for polymer is given by

$$\frac{\partial}{\partial t}\Big(c(s_w - s_{\text{ipv}})\Big) + u\frac{\partial}{\partial x}\Big(cf(s_w)\Big) = 0, \tag{7}$$

where u denotes the ratio between the total velocity and the porosity, that is $u = (v_o + v_w)/\phi$. In (7), we can see that c denotes the concentration of polymer with respect to the amount of water in the accessible region while, in the conventional model, it denotes the concentration with respect to the total amount of water. This formulation corresponds to the model used by the commercial simulator Eclipse before 2008 [12], and is also equivalent to the percolation-based model *after renormalization* of the concentration. Indeed, if we set

$$c = \bar{c}\frac{s_w}{s_w - s_{\text{ipv}}},$$

then (7) becomes

$$\frac{\partial}{\partial t}(\bar{c}s_w) + u\frac{\partial}{\partial x}\Big(\bar{c}\gamma(s_w)f(s_w)\Big) = 0,$$

where γ is given by (6). This is the percolation-based model written using a fractional flow formulation. We will show in the following that this model may also lead to an ill-posed problem, depending on the parameters of the particular problem.

4 A Necessary Condition for Well-Posedness

By considering shock solutions of our equations, we will now derive a necessary condition for well-posedness. Consider a one-dimensional case where the water flow is not affected by the presence of polymer, and the polymer behaves as an inert component, whose flux depends on a velocity enhancement factor γ, which is a function of saturation. In this section, a Buckley-Leverett formulation is used. Assuming incompressibility, the governing equations are

$$\frac{\partial s_w}{\partial t} + u\frac{\partial f(s_w)}{\partial x} = 0, \tag{8a}$$

$$\frac{\partial (s_w c)}{\partial t} + u\frac{\partial}{\partial x}\Big(c\gamma(s_w)f(s_w)\Big) = 0, \tag{8b}$$

where the fractional flow function is

$$f(s_w) = \frac{k_{rw}/\mu_w}{k_{rw}/\mu_w + k_{ro}/\mu_o},$$

and $u = (v_o + v_w)/\phi$. For simplicity, but without loosing generality, assume the velocity is $u = 1$. Let $z = s_w c$ and consider the Riemann problem with values (s_l, z_l) and (s_r, z_r), on respectively the left and right hand-side. Assume the values s_l and s_r are such that $s_l > s_r$ and the solution to (8a) is a pure shock. Such a pair of saturations will be called a *single shock pair*. The shock speed for the water wave is given by the Rankine-Hugoniot condition

$$v = \frac{f(s_l) - f(s_r)}{s_l - s_r}.$$

The polymer conservation equation is now rewritten in a moving frame following the water front with velocity v. Let $\hat{x} = x - vt$ and denote $\hat{s}(\hat{x}) = s_w(t, x)$ and $\hat{z}(t, \hat{x}) = z(t, x)$. After a change of variables, equation (8b) becomes

$$\frac{\partial \hat{z}}{\partial t} + \frac{\partial}{\partial \hat{x}}\Big(\hat{z}(\frac{\gamma(\hat{s})}{\hat{s}}f(\hat{s}) - v)\Big) = 0.$$

To simplify the notation, the hat notation on the variables is removed in the following, and it is understood that we are in a moving frame. Because of the discontinuity in the water saturation, the polymer problem has discontinuous flux,

$$\frac{\partial z}{\partial t} + \frac{\partial}{\partial x}(g_l z) = 0 \quad \text{if } x < 0, \qquad \frac{\partial z}{\partial t} + \frac{\partial}{\partial x}(g_r z) = 0 \quad \text{if } x > 0, \tag{9}$$

where the constants g_l and g_r are given by

$$g_l = \frac{\gamma(s_l)f(s_l)}{s_l} - v, \quad \text{and,} \quad g_r = \frac{\gamma(s_r)f(s_r)}{s_r} - v. \tag{10}$$

We want to show that for any single shock pair and for any non-negative z_l and z_r, we can find values z_- and z_+ at the discontinuities for which the following conditions are fulfilled.

1. For $x < 0$, there exists a Riemann solution to $\frac{\partial z}{\partial t} + \frac{\partial}{\partial x}(g_l z) = 0$ for (z_l, z_-) with only waves traveling from right to left.
2. The Rankine-Hugoniot condition $g_l z_- = g_r z_+$ holds.
3. For $x > 0$, there exists a Riemann solution to $\frac{\partial z}{\partial t} + \frac{\partial}{\partial x}(g_r z) = 0$ for (z_+, z_r) with only waves traveling from left to the right.

We say that a Riemann solution is *acceptable* if it satisfies the three requirements above, and that a pair z_l and z_r is *solvable* if there is an acceptable Riemann solution joining z_l to z_r. To obtain a well-posed problem, we need to find a function γ such that any pair (z_l, z_r) will be solvable. All the different cases are divided into four groups depending on the sign of g_l and g_r. For the three cases presented in Figure 2, any pair (z_l, z_r) is solvable. The remaining cases are

$$g_l \geq 0 \quad \text{and} \quad g_r \leq 0 \quad \text{with} \quad g_l \neq g_r, \tag{11}$$

and $g_l = g_r = 0$. If $g_l = g_r = 0$, the solution remains unchanged in the moving frame. If the condition (11) holds, then $g_l z_- = g_r z_+$ implies that only the pairs with either $z_l = 0$ or $z_r = 0$ are solvable. Therefore, to obtain a well-posed problem, γ must be chosen such that (11) never occurs. Consider the case where $s_r = s_{\text{wir}}$, the irreducible water saturation, such that $f(s_r) = 0$. Then, we have $g_r(z_r) = -v \leq 0$. Hence, for (11) not to happen, we must have $g_l \leq 0$, that is,

$$\frac{\gamma(s_l)f(s_l)}{s_l} - v \leq 0.$$

Using the fact that $v = \frac{f(s_l)}{s_l - s_{\text{wir}}}$, we can rewrite this as

$$\gamma(s) \leq \frac{s}{s - s_{\text{wir}}}, \tag{12}$$

for $s = s_l$. The condition (12) is a *necessary* condition for an IPV model. In Proposition 8.1 in the Appendix, we present mild assumptions on the fractional flow for which this condition becomes sufficient in the sense that if (12) is satisfied for any single shock pair, then any pair (z_l, z_r) is solvable. Moreover, the proposition shows that $g_l > 0$ is not a possibility, meaning that the first configuration in Figure 2 does not occur either. To derive the necessary condition (12), we rely on the Rankine-Hugoniot condition. Alternative solution concepts can be considered and, in particular, δ-shock solutions. In [6], the authors present a construction of δ-shock solutions for a system of equations which coincides with (8) when additional properties on the fluxes are

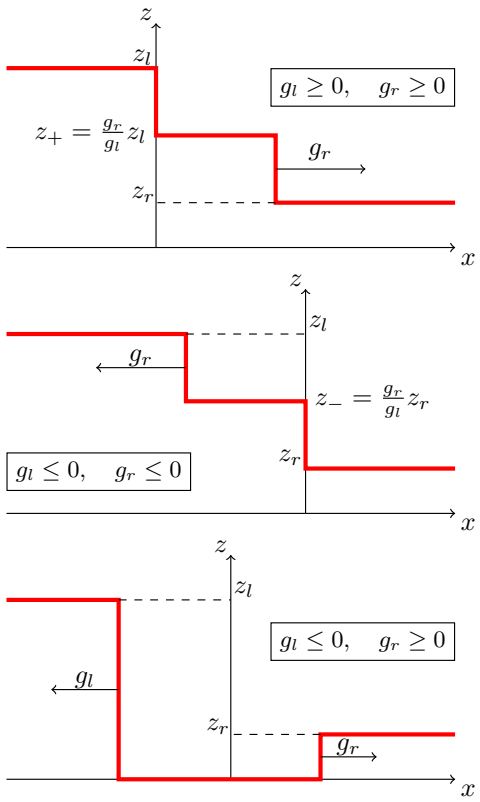

Figure 2: Acceptable shock solutions of (9) for different signs of g_l and g_r.

assumed. The δ-shock solutions opens for the possibility of strongly localized accumulation of polymer at a single point, which is the support of a δ-function. Needless to say, such solutions are very irregular and will be a challenge to simulate numerically. When using the Rankine-Hugoniot condition, we *de facto* exclude such solutions. However one could argue that, if we introduce back the coupling between the polymer concentration and the water flux, then, in regions of high polymer concentration, the accelerating effect of IPV may be canceled out by the viscous effect of polymer which slows down the flow, and δ-shock solutions may never form. Yet, in this paper, we will not consider δ-shock solutions. This type of solution remains very challenging from a theoretical and practical point of view.

5 IPV Based on Relative Permeability Model

By first presenting a heuristic understanding of relative permeability, we will derive different models for the inaccessible pore volume. Our relative permeability model is based on the following principle: Due to capillary forces, for a water-wet system, the water invades the smallest pores first. At the same time, in the region of the smallest pores, the permeability is lower and water travels slower.

5.1 A Simple Interpretation of Relative Permeability

Consider a model with one-dimensional incompressible flow. Define a pore size distribution function $\chi(\hat{r})$ where $\hat{r}$ denotes the characteristic length of a pore. For each pore size $\hat{r}$, there corresponds a permeability $\hat{k}(\hat{r})$, and the total permeability is then given by

$$K = \frac{n}{A} \int_0^\infty \pi r^2 \hat{k}(\hat{r}) \chi(\hat{r}) \, d\hat{r},$$

for tubular sections, where n denotes the number of pore in a cross-section of area A. We can rewrite this expression as

$$K = n \int_0^\infty \hat{\phi}(\hat{r}) \hat{k}(\hat{r}) \chi(\hat{r}) \, d\hat{r}, \tag{13}$$

which can accommodate for more general structures by choosing different function $\hat{\phi}$. Equation (13) corresponds to an upscaling of the permeability using an arithmetic average. More advanced models include tortuosity, see [3]. The water saturation is denoted $\hat{s}(\hat{r})$, which is assumed to be the same in all the pores of the same size $\hat{r}$. In the case of a parallel tubular structure, the global water saturation would be defined as a function of χ and $\hat{s}$ through the relation

$$\phi s = n \int_0^\infty \hat{\phi}(\hat{r}) \hat{s}(\hat{r}) \chi(\hat{r}) \, d\hat{r}.$$

Here, our aim is simply to obtain a definition of the global saturation s given as a weighted integral of the pore saturation. Now, we use our main simplifying assumption, which will contain all the effects of the capillary forces that relative permeabilities are meant to contain as an upscaled quantity. We assume that, due to capillary forces, for a water-wet medium, the pores are filled successively, in increasing order of their size. Hence, for a given global saturation s, there exists a threshold for the pore size, which we denote $r(s)$ or simply r, such that

$$\hat{s}(\hat{r}) = \begin{cases} 1 & \text{if } \hat{r} \leq r(s), \\ 0 & \text{if } \hat{r} > r(s). \end{cases} \tag{14}$$

This definition enables us to rewrite (5.1) as

$$s = \frac{n}{\phi} \int_0^{r(s)} \hat{\phi}(\hat{r}) \chi(\hat{r}) \, d\hat{r}$$

or

$$s(r) = \frac{\int_0^r \hat{\phi}(\hat{r}) \chi(\hat{r}) \, d\hat{r}}{\int_0^\infty \hat{\phi}(\hat{r}) \chi(\hat{r}) \, d\hat{r}}, \tag{15}$$

which also provides us with a well-defined definition of $r(s)$, as long as the mapping $r \mapsto s(r)$ in (15) can be inverted, that is, if $\frac{dr}{ds} > 0$ is when $s \in (0, 1)$. Another relation, also relating the saturation and the hydraulic radius, can be found in [2]. This relation is defined by using the capillary pressure function $p_c(s)$ such that the definition of the relative permeability contains upscaled effects originating from capillary effects. Herein, we will base our analysis on (15) where, as we said earlier, all upscaled effects and in particular those coming from capillary pressure are modeled through the simplifying assumption presented above which states that the smallest pores are invaded first. The water phase permeability in a pore of size $\hat{r}$ is equal to $\hat{s}(\hat{r})\hat{k}(\hat{r})$, and the total phase permeability is

$$K_w = n \int_0^\infty \hat{\phi}(\hat{r}) \hat{s}(\hat{r}) \hat{k}(\hat{r}) \chi(\hat{r}) \, d\hat{r}. \tag{16}$$

The mass conservation equation for water can then be written as

$$\frac{\partial}{\partial t}(\phi s) - \frac{\partial}{\partial x} \left(\frac{n}{\mu_w} \int_0^\infty \hat{\phi}(\hat{r}) \hat{s}(\hat{r}) \hat{k}(\hat{r}) \chi(\hat{r}) \, d\hat{r} \frac{\partial p}{\partial x} \right) = 0.$$

An expression for the water relative permeability $k(s)$ can be found by dividing the phase permeability (16) by the absolute permeability (13), such that

$$k(s) = \frac{K_w}{K} = \frac{\int_0^\infty \hat{\phi}(\hat{r})\hat{s}(\hat{r})\hat{k}(\hat{r})\chi(\hat{r})\,d\hat{r}}{\int_0^\infty \hat{\phi}(\hat{r})\hat{k}(\hat{r})\chi(\hat{r})\,d\hat{r}} = \frac{\int_0^r \hat{\phi}(\hat{r})\hat{k}(\hat{r})\chi(\hat{r})\,d\hat{r}}{\int_0^\infty \hat{\phi}(\hat{r})\hat{k}(\hat{r})\chi(\hat{r})\,d\hat{r}}, \tag{17}$$

where in the last equality we have used (14) to simplify the expression. After differentiating (15), we get

$$\frac{ds}{dr} = \frac{\hat{\phi}(r)\chi(r)}{\int_0^\infty \hat{\phi}(\hat{r})\chi(\hat{r})\,d\hat{r}}, \tag{18}$$

so that

$$\frac{dk}{ds} = \hat{k}(r(s))\frac{\int_0^\infty \hat{\phi}(\hat{r})\chi(\hat{r})\,d\hat{r}}{\int_0^\infty \hat{\phi}(\hat{r})\hat{k}(\hat{r})\chi(\hat{r})\,d\hat{r}}. \tag{19}$$

It is reasonable to assume that $\hat{k}(\hat{r})$ is an increasing function of $\hat{r}$, as the flow increases with the size of the pores. As $r(s)$ is an increasing function in s, see (18), the expression (19) tells us that $\frac{dk}{ds}$ is increasing in s, that is, k is a convex function. The convexity of the relative permeability, which is a common feature, at least for models which are not upscaled, is therefore naturally embedded in the model.

5.2 Uniform Polymer Diffusion

Polymer is now included in the heuristic model. Denote by $\hat{c}(\hat{r})$ the concentration of polymer in pores of size $\hat{r}$. The global polymer concentration c satisfies the relation

$$\phi sc = n\int_0^\infty \hat{c}(\hat{r})\hat{\phi}(\hat{r})\hat{s}(\hat{r})\chi(\hat{r})\,d\hat{r},$$

which by (14) simplifies to

$$\phi sc = n\int_0^r \hat{c}(\hat{r})\hat{\phi}(\hat{r})\chi(\hat{r})\,d\hat{r}. \tag{20}$$

The inaccessible pore volume can be modeled by defining a pore size r_{ipv} such that polymer cannot enter pores of smaller size than r_{ipv}. That is,

$$\hat{c}(\hat{r}) = \begin{cases} 0 & \text{if } r \le r_{\text{ipv}}, \\ \bar{c} & \text{if } r > r_{\text{ipv}}. \end{cases} \tag{21}$$

In the region $r > r_{\text{ipv}}$, it is assumed that the polymer diffuses uniformly and reaches a constant concentration which is denoted $\bar{c}$. Let $s_{\text{ipv}} = s(r_{\text{ipv}})$ by using definition (15), and insert $\hat{c}$ from (21) into (20) to obtain

$$\phi sc = n\bar{c}\int_{r_{\text{ipv}}}^r \hat{\phi}(\hat{r})\chi(\hat{r})\,d\hat{r} = \phi\bar{c}\Big(s - s_{\text{ipv}}\Big),$$

or

$$c = \bar{c}\frac{s - s_{\text{ipv}}}{s}. \tag{22}$$

Similar to how the water phase permeability was defined, the permeability of water and polymer in a pore of size $\hat{r}$ is defined to be $c(\hat{r})\hat{s}(\hat{r})\hat{k}(\hat{r})$. The mass conservation equation for polymer can then be written as

$$\frac{\partial}{\partial t}(\phi sc) - \frac{\partial}{\partial x}\left(\frac{n}{\mu_w}\int_0^\infty \hat{c}(\hat{r})\hat{\phi}(\hat{r})\hat{s}(\hat{r})\hat{k}(\hat{r})\chi(\hat{r})\,d\hat{r}\frac{\partial p}{\partial x}\right) = 0. \tag{23}$$

After applying the assumptions (14) and (21), this yields

$$\frac{\partial}{\partial t}(\phi sc) - \frac{\partial}{\partial x}\left(\frac{n}{\mu_w}\bar{c}\int_{r_{\text{ipv}}}^r \hat{\phi}(\hat{r})\hat{k}(\hat{r})\chi(\hat{r})\,d\hat{r}\frac{\partial p}{\partial x}\right) = 0.$$

Then, using (17) and (22), this becomes

$$\frac{\partial}{\partial t}(\phi sc) - \frac{\partial}{\partial x}\left(c\frac{s}{s - s(r_{\text{ipv}})}\Big(k(s) - k(s_{\text{ipv}})\Big)\frac{K}{\mu_w}\frac{\partial p}{\partial x}\right) = 0.$$

If now this equation is rewritten as

$$\frac{\partial}{\partial t}(\phi sc) - \frac{\partial}{\partial x}\left(c\gamma(s)\frac{k(s)}{\mu_w}K\frac{\partial p}{\partial x}\right) = 0,$$

then the velocity enhancement factor is

$$\gamma(s) = \frac{s}{k(s)}\frac{k(s) - k(s_{\text{ipv}})}{s - s_{\text{ipv}}}, \tag{24}$$

To make a well-defined function for all values, we define $\gamma(s) = 0$ for $s \leq s_{\text{ipv}}$.

If it is assumed as in [1] that $s_{\text{ipv}} \leq s_{\text{wir}}$, i.e., that the inaccessible pore volume ratio is less than the irreducible water saturation[1], then $k(s_{\text{ipv}}) = 0$ and $\gamma(s)$ reduces to

$$\gamma(s) = \frac{s}{s - s_{\text{ipv}}}, \tag{25}$$

which means we obtain the percolation based model as presented in [1] and discussed in Section 3.2. The expression (24) apparently opens for the possibility of inaccessible pore space values s_{ipv} that are larger than s_{wir}. As the well-posedness condition (12) for γ should still hold, we must have

$$\frac{k(s) - k(s_{\text{ipv}})}{s - s_{\text{ipv}}} \leq \frac{k(s) - k(s_{\text{wir}})}{s - s_{\text{wir}}}. \tag{26}$$

Note that $k(s_{\text{wir}}) = 0$, but we have included this term in the inequality for the sake of symmetry. If we assume that the function k is convex, which is consistent with our interpretation, then the condition (26) is fulfilled only if $s_{\text{ipv}} \leq s_{\text{wir}}$. That is, the enhancement factor $\gamma(s)$ as defined by (24) is not applicable in general when $s_{\text{ipv}} > s_{\text{wir}}$. To arrive at an enhancement factor without this restriction, we move away from the assumption of uniform polymer diffusion in the following.

5.3 Non-Uniform Polymer Diffusion

Depending on the time-scale of the problem, the instantaneous polymer diffusion assumption (21) may not be appropriate, and it is now replaced by a weighted expression

$$\hat{c}(\hat{r}) = \hat{w}(\hat{r})\bar{c}. \tag{27}$$

The weighting function $\hat{w}$ reflects the fact that, for a given upscaled concentration c, higher concentrations are expected in the regions where diffusion is smaller. The inaccessible pore space assumption can be incorporated by requiring that $\hat{w}(\hat{r}) = 0$ for $\hat{r} \leq r_{\text{ipv}}$. Inserting the weighted expression (27) into (20) yields

$$\phi sc = n\bar{c}\int_0^r \hat{w}(\hat{r})\hat{\phi}(\hat{r})\chi(\hat{r})\,d\hat{r},$$

which may be written

$$\bar{c} = \frac{sc}{W(s)}, \tag{28}$$

by introducing $W(s)$ as defined by

$$W(s) = \frac{n}{\phi}\int_0^r \hat{w}(\hat{r})\hat{\phi}(\hat{r})\chi(\hat{r})\,d\hat{r}.$$

[1]The assumption in [1] is actually that $s_{\text{ipv}} < s_{\text{wc}}$, the connate water saturation. However, it is also assumed that water is immobile at s_{wc}, meaning $s_{\text{wir}} = s_{\text{wc}}$. Herein, on the other hand, we allow for mobile connate water, and may have $s_{\text{wir}} < s_{\text{wc}}$.

Note that

$$\frac{dW}{ds} = \frac{dW}{dr}\frac{dr}{ds} = \hat{w}(r). \tag{29}$$

The water and polymer permeability from (23) may be rewritten as

$$\begin{aligned} n\int_0^\infty \hat{c}(\hat{r})\hat{\phi}(\hat{r})\hat{s}(\hat{r})\hat{k}(\hat{r})\chi(\hat{r})\,d\hat{r} &= n\bar{c}\int_0^r \hat{w}(\hat{r})\hat{\phi}(\hat{r})\hat{k}(\hat{r})\chi(\hat{r})\,d\hat{r}, \\ &= \bar{c}K\int_0^s \frac{dW}{ds}\frac{dk}{ds}ds, \end{aligned}$$

after using (17) and (29). Hence, after inserting the expression (28) for $\bar{c}$, then the following new expression is obtained for γ,

$$\gamma(s) = \frac{s\displaystyle\int_0^s W'(\hat{s})k'(\hat{s})\,d\hat{s}}{W(s)k(s)}. \tag{30}$$

The function W will be convex if the polymer tends to occupy preferentially the region with large pore space, concave if it occupies preferentially the region with small pore space and linear if the distribution is uniform. In the later case, we would have

$$W(s) = \begin{cases} 0 & \text{if } s < s_{\text{ipv}}, \\ A(s - s_{\text{ipv}}) & \text{if } s_{\text{ipv}} \le s \le 1 - s_{\text{or}}, \end{cases} \tag{31}$$

for some constant A and we recover (24). Note that we have not chosen any normalization for $W(s)$ and, from the definition (30) of γ, we see that the normalization constant can be chosen arbitrarily. It means that we can simplify (31) by choosing $A = 1$. In (30), as $k(s) = 0$ for $s \le s_{\text{wir}}$, the integration domain can be restricted to $[s_{\text{wir}}, s]$ and the well-posedness condition (12) imposes

$$\frac{\displaystyle\int_{s_{\text{wir}}}^s W'(\hat{s})k'(\hat{s})\,d\hat{s}}{W(s)k(s)} \le \frac{1}{s - s_{\text{wir}}}. \tag{32}$$

If we consider, as before, a strictly inaccessible pore volume s_{ipv}, then we have $W(s) = W'(s) = 0$ for $s \le s_{\text{ipv}}$. In this case, if $s_{\text{ipv}} \ge s_{\text{wir}}$, letting s tending to s_{ipv} in (32) yields

$$k'(s_{\text{ipv}}) \le \frac{k(s_{\text{ipv}}) - k(s_{\text{wir}})}{s_{\text{ipv}} - s_{\text{wir}}}. \tag{33}$$

The condition (33) cannot be fulfilled for $s_{\text{ipv}} > s_{\text{wir}}$ if the function k is convex. In other words, the inaccessible pore volume s_{ipv} can be larger than the irreducible water saturation s_{wir} only if $k(s)$ is non-convex. There is no such requirement for $s_{\text{ipv}} < s_{\text{wir}}$. As relative permeability functions usually are convex, this in practice means the weighted velocity enhancement factor (30) does not fulfill the well-posed condition if we assume a strictly inaccessible pore volume. However, by slightly relaxing this assumption, we can overcome the limitation of requiring $s_{\text{ipv}} < s_{\text{wir}}$.

5.4 Relaxing the IPV Definition

The models considered so far all require $s_{\text{ipv}} < s_{\text{wir}}$ for the well-posedness condition (32) to be satisfied. Our goal is to obtain a model where the value of the inaccessible pore volume is not constrained by the value of the irreducible water saturation. To do so, we relax the definition of inaccessible pore volume and consider functions W of the form

$$W(s) = \begin{cases} \frac{\varepsilon}{s_{\text{ipv}}}s & \text{if } s < s_{\text{ipv}}, \\ \varepsilon + (s - s_{\text{ipv}}) & \text{if } s_{\text{ipv}} \le s \le 1 - s_{\text{or}}, \end{cases} \tag{34}$$

as shown in red in Figure 3. When ε tends to zero, we recover (31). For $\varepsilon > 0$ on the other hand, we have $W(s) > 0$ for $s < s_{\text{ipv}}$, meaning that there will be polymer in the inaccessible pore regions, but to much less extent than in the other regions.

First note that in the case where $s_{\text{ipv}} \leq s_{\text{wir}}$, then (34) reduces to $W(s) = \varepsilon + s - s_{\text{ipv}}$ for all s, and in the degenerated case where $s_{\text{ipv}} = 0$, we have $W(s) = \varepsilon + s$ for all s. In both cases, it is easy to show that the well-posedness condition (32) is satisfied for all $\varepsilon \geq 0$, and in particular for $\varepsilon = 0$. If we set $\varepsilon = 0$ for the case where $s_{\text{ipv}} \leq s_{\text{wir}}$, then (34) reduces to (31), and we recover (25). That is,

$$\gamma(s) = \frac{s}{s - s_{\text{ipv}}}.$$

In the following, we concentrate on the remaining cases, and assume both $s_{\text{ipv}} > s_{\text{wir}}$ and $s_{\text{ipv}} > 0$.

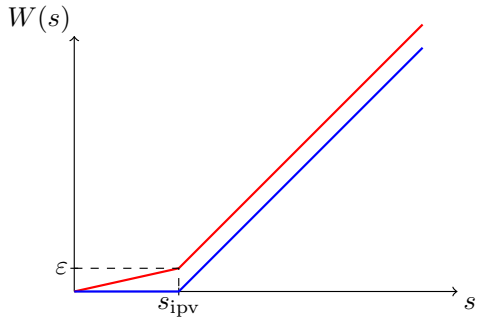

Figure 3: Relaxation of the inaccessible pore volume. In blue, we plot the function $W(s)$ as given in (31), which correspond to the percolation-based model. In red, we plot the relaxation given by (34).

Inserting the function $W(s)$ given by (34) into the definition of the γ from (30), we obtain

$$\gamma(s) = \begin{cases} 0 & \text{if } s \leq s_{\text{ipv}}, \\ s\dfrac{k(s) + \frac{\varepsilon - s_{\text{ipv}}}{s_{\text{ipv}}} k(s_{\text{ipv}})}{(s + \varepsilon - s_{\text{ipv}})k(s)} & \text{if } s > s_{\text{ipv}}. \end{cases} \tag{35}$$

Since we always have $1 \leq \frac{s}{s - s_{\text{wir}}}$, the well-posedness condition (32) is clearly fulfilled if $s \leq s_{\text{ipv}}$. If on the other hand $s > s_{\text{ipv}}$, the condition becomes

$$\frac{k(s) + \frac{\varepsilon - s_{\text{ipv}}}{s_{\text{ipv}}} k(s_{\text{ipv}})}{(s + \varepsilon - s_{\text{ipv}})k(s)} \leq \frac{1}{s - s_{\text{wir}}}. \tag{36}$$

This expression provides us with a necessary condition on ε for the model to be well-posed. To continue this analytical study, we assume that the relative permeability follows a Corey model, that is,

$$k(s) = \left(\frac{s - s_{\text{wir}}}{1 - s_{\text{wir}} - s_{\text{or}}} \right)^{N_w},$$

where we assume $N_w \geq 1$. In this case, the condition (36) is fulfilled for $s > s_{\text{ipv}}$ if the function $F(s, \varepsilon)$ defined as

$$F(s, \varepsilon) = (s + \varepsilon - s_{\text{ipv}})(s - s_{\text{wir}})^{N_w - 1} - (s - s_{\text{wir}})^{N_w} - \frac{\varepsilon - s_{\text{ipv}}}{s_{\text{ipv}}}(s_{\text{ipv}} - s_{\text{wir}})^{N_w},$$

remains non-negative for all $s > s_{\text{ipv}}$. The function F can be rewritten as

$$F(s, \varepsilon) = (\varepsilon - s_{\text{ipv}} + s_{\text{wir}})(s - s_{\text{wir}})^{N_w - 1} - \frac{\varepsilon - s_{\text{ipv}}}{s_{\text{ipv}}}(s_{\text{ipv}} - s_{\text{wir}})^{N_w}.$$

From this, we see that F is monotonic in s. Also, as we have assumed $s_{\text{ipv}} > s_{\text{wir}}$, we see that

$$F(s_{\text{ipv}}, \varepsilon) = \varepsilon \frac{s_{\text{wir}}}{s_{\text{ipv}}} (s_{\text{ipv}} - s_{\text{wir}})^{N_w - 1} > 0.$$

If $\varepsilon \geq s_{\text{ipv}} - s_{\text{wir}}$, then the function F is non-decreasing in s and thus $F > 0$ for $s > s_{\text{ipv}}$, and the well-posedness condition (36) holds.

If we instead consider $\varepsilon \leq s_{\text{ipv}} - s_{\text{wir}}$, the function F is non-increasing in s, and the sign of F will depend on s. Considering the maximum saturation $s = 1 - s_{\text{or}}$, which will give the minimum of F for any given ε, we get that

$$F(1 - s_{\text{or}}, 0) \leq 0 < F(1 - s_{\text{or}}, s_{\text{ipv}} - s_{\text{wir}}),$$

This implies that, as F is continuous in ε, there exists for each N_w, a corresponding ε_{N_w}, such that $F(1 - s_{\text{or}}, \varepsilon_{N_w}) = 0$, which again implies $F(s, \varepsilon_{N_w}) \geq 0$ for all s. Also, we observe that

$$\varepsilon_1 = 0, \quad \text{and} \quad \lim_{N_w \to \infty} \varepsilon_{N_w} = s_{\text{ipv}} - s_{\text{wir}}.$$

Thus, for any $\varepsilon < s_{\text{ipv}} - s_{\text{wir}}$, there will exist a Corey coefficient N_w such that the corresponding γ leads to an ill-posed model. Hence $\varepsilon = s_{\text{ipv}} - s_{\text{wir}}$ is the smallest value of ε that fulfills the well-posed condition for all Corey relative permeability curves.

If we now try to insert the value $\varepsilon = s_{\text{ipv}} - s_{\text{wir}}$ into (35), we obtain

$$\gamma(s) = \begin{cases} 0 & \text{if } s \leq s_{\text{ipv}}, \\ \left(1 - \frac{s_{\text{wir}}}{s_{\text{ipv}}} \frac{k(s_{\text{ipv}})}{k(s)}\right) \dfrac{s}{s - s_{\text{wir}}} & \text{if } s > s_{\text{ipv}}. \end{cases} \tag{37}$$

Recall that we have assumed $s_{\text{ipv}} > s_{\text{wir}}$, such that this expression for $\gamma(s)$ is well-defined. That this choice of $\gamma(s)$ fulfills the well-posedness condition (36) not only for all Corey-type curves, but the condition is actually fulfilled for *any choice* of relative permeability k. Hence, we have found an ε which is optimal in the sense that it yields a well-posed velocity enhancement function γ for any relative permeability function, and, for any smaller value of ε, there exists a relative permeability function such that the corresponding γ leads to an ill-posed model.

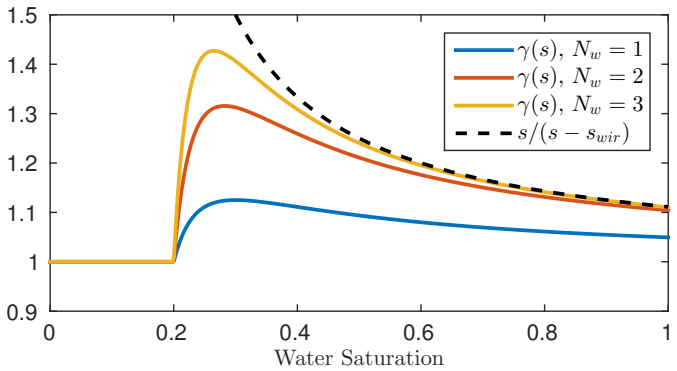

Figure 4: Examples of velocity enhancement functions $\gamma(s)$, given by (37), for different Corey coefficients N_w. Here, we have chosen $s_{\text{wir}} = 0.1$, $s_{\text{or}} = 0$ and $s_{\text{ipv}} = 0.2$. The upper limit for γ, given by the well-posedness condition (12), is also shown.

6 Numerical Examples

6.1 Overview of IPV Models

In the following, we will apply the different IPV models in numerical examples to observe how their results differ for different model parameters. To summarize the different methods discussed

above and to create a clear overview, the velocity enhancement factor γ appearing in the polymer equation (3) for each method is listed below.

The percolation based model assumes $s_{\text{ipv}} \leq s_{\text{wir}}$. To still be able to include this model in all simulation for comparison, we create a simple extension to the model by defining $\gamma(s) = 0$ for $s \leq s_{\text{ipv}}$.

I) Conventional model, with constant velocity enhancement.

$$\gamma = \frac{1}{1 - s_{\text{ipv}}}.$$

II) Percolation based model.

$$\gamma(s) = \begin{cases} \dfrac{s}{s - s_{\text{ipv}}} & \text{if } s > s_{\text{ipv}}, \\ 0 & \text{if } s \leq s_{\text{ipv}}. \end{cases}$$

III) Model based on uniform polymer diffusion.

$$\gamma(s) = \begin{cases} \dfrac{s}{k(s)} \dfrac{k(s) - k(s_{\text{ipv}})}{s - s_{\text{ipv}}} & \text{if } s_{\text{ipv}} > s_{\text{wir}} \text{ and } s > s_{\text{ipv}}, \\ \dfrac{s}{s - s_{\text{ipv}}} & \text{if } s_{\text{ipv}} \leq s_{\text{wir}} \text{ and } s > s_{\text{ipv}}, \\ 0 & \text{if } s \leq s_{\text{ipv}}. \end{cases}$$

IV) Model based on non-uniform polymer diffusion with a relaxation of the IPV definition.

$$\gamma(s) = \begin{cases} \left(1 - \dfrac{s_{\text{wir}}}{s_{\text{ipv}}} \dfrac{k(s_{\text{ipv}})}{k(s)}\right) \dfrac{s}{s - s_{\text{wir}}} & \text{if } s_{\text{ipv}} > s_{\text{wir}} \text{ and } s > s_{\text{ipv}}, \\ \dfrac{s}{s - s_{\text{ipv}}} & \text{if } s_{\text{ipv}} \leq s_{\text{wir}} \text{ and } s > s_{\text{ipv}}, \\ 0 & \text{if } s \leq s_{\text{ipv}}. \end{cases}$$

6.2 1D Examples

Consider a one-dimensional Cartesian grid of length 1 m discretized into 200 cells, with homogeneous permeability and porosity $\phi = 0.3$. Water with polymer is injected over the West boundary from the beginning of the simulation until 0.25 pore volumes of water is injected. All examples below are run using each of the four IPV-models using a sequential solver.

Example 1: Linear Relative Permeability, $s_{\text{ipv}} > s_{\text{wir}}$

This first example is similar to the example we used to illustrate the instability of the conventional model in Section 3.1. The relative permeabilities are linear, and the inaccessible pore volume is larger than the irreducible water saturation. The example setup is summarized in Table 1, where we use the scaled water saturation

$$s = \frac{s_w - s_{\text{wir}}}{1 - s_{\text{wir}} - s_{\text{or}}}. \tag{38}$$

In this example, the polymer do not influence the viscosity, and thus acts as a tracer.

The results are shown in Figure 5. The water saturation is identical for all four models as the polymer has no influence on the water phase. For the polymer concentration however, both the conventional and the percolation model show a sharp spike at the polymer front. The spikes are an indication of how polymer attempts to travel faster than the water front, and gets accumulated at the front. The uniform and non-uniform models do not produce any such peak in the solution.

s_{wir}	s_{ipv}	k_{rw}	k_{ro}	μ_w	μ_o
0.1	0.105	s^1	$(1-s)^1$	1 cP	1 cP

Table 1: Parameters for example 1. Scaled saturation s is given by (38).

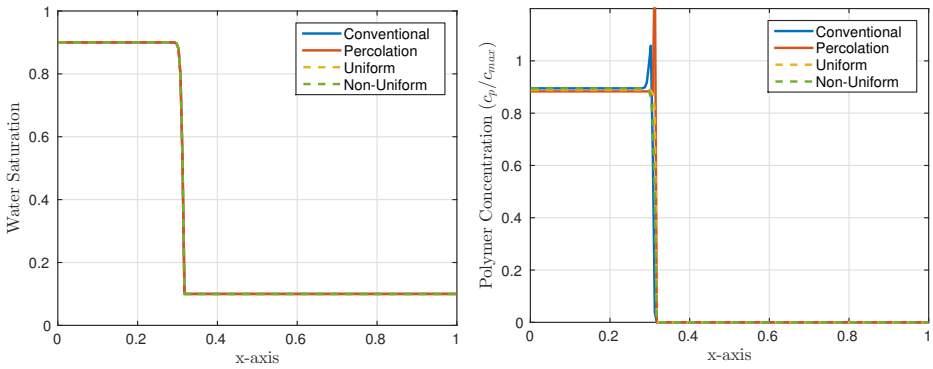

Figure 5: Solution of example 1.

Example 2: Quadratic Relative Permeability, $s_{\text{ipv}} > s_{\text{wir}}$

The setup of the simulation is the same as for Example 1, except that the fluids now have quadratic relative permeabilities. Considering the solutions in Figure 6, the conventional model shows a pile up in the polymer concentration, but not a sharp spike as in Example 1. The percolation model and the uniform model are almost identical, with a steeper peak in the concentration at the polymer front. The peaks will grow differently depending on grid resolution and time-stepping, but this could indicate potential problems with the solutions. The non-uniform model on the other hand, do not possess any peak.

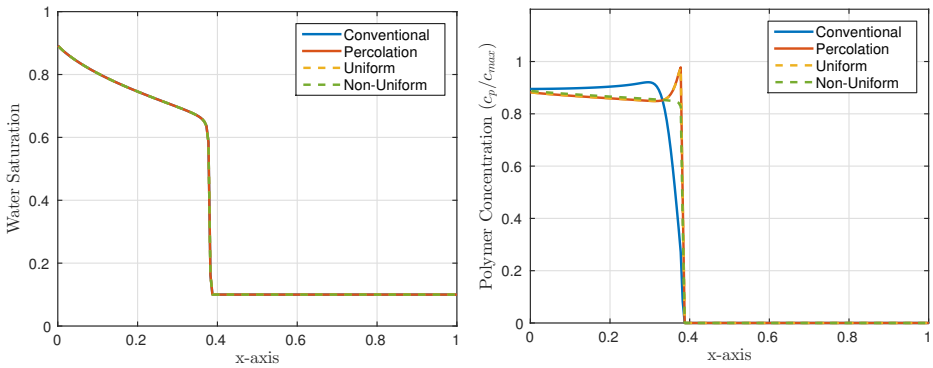

Figure 6: Solution of example 2.

Example 3: Polymer not a Tracer, $s_{\text{ipv}} < s_{\text{wir}}$

This example is similar to the problem discussed in [1], though not identical. In contrast to the previous two examples, the polymer is no longer just a tracer, but has a simple viscosity model $\mu_{p,\text{eff}} = \mu_{w,\text{eff}} = 1 + c^2$. The other fluid properties are summarized in Table 2.

The results are shown in Figure 7. The conventional model shows also now a pile up in the polymer concentration, with values above the the maximum concentration. As $s_{\text{ipv}} < s_{\text{wir}}$ in this case, we can see from Section 6.1 that the other three methods reduce to the same model, and are identical for this example.

s_{wir}	s_{ipv}	k_{rw}	k_{ro}	μ_w	μ_o
0.1	0.09	s^2	$(1-s)^2$	1 cP	10 cP

Table 2: Parameters for example 3. Scaled saturation s is given by (38).

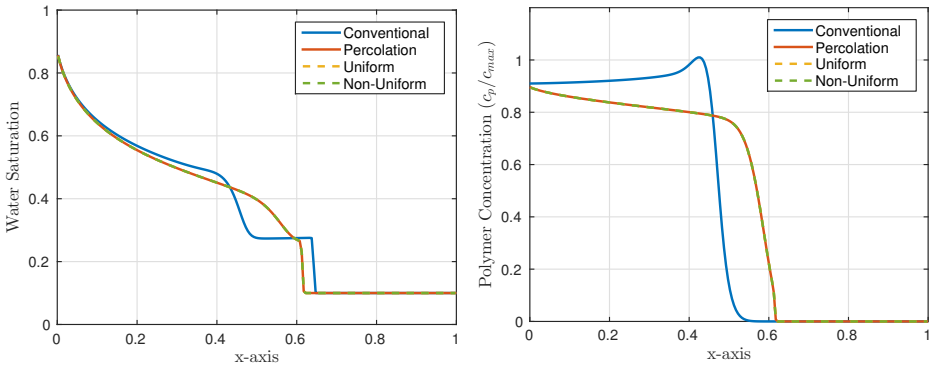

Figure 7: Solution of example 3.

Example 4: Polymer not a Tracer, $s_{\text{ipv}} > s_{\text{wir}}$

This example uses the same setup as Example 3, except that we now set $s_{\text{ipv}} = 0.11 > s_{\text{wir}}$. The results are shown in Figure 8, where we observe that the conventional model has a similar polymer profile as in the previous example. The percolation model and the non-uniform model both have a sharp spike in the polymer concentration, which seem to grow uncontrolled, while the non-uniform model do not show any pile-up effect.

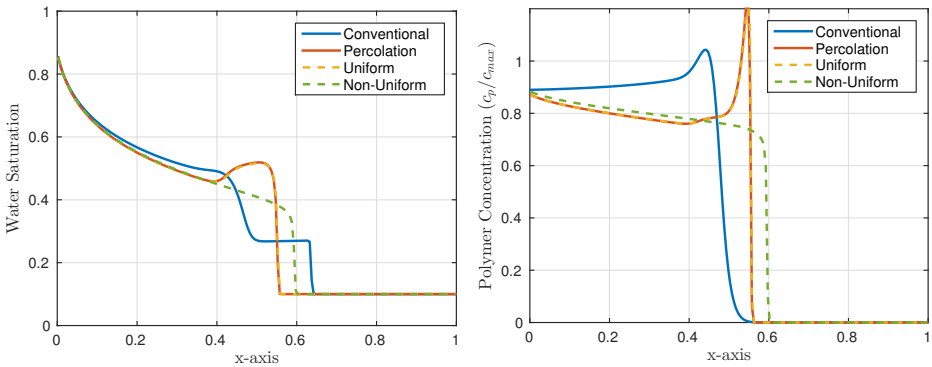

Figure 8: Solution of example 4.

6.3 Numerical 2D Example

Consider a two-dimensional domain with heterogeneous porosity and permeability created by a log-normal distribution. The viscosity model is chosen as $\mu_{p,\text{eff}} = \mu_{w,\text{eff}} = 1 + (3c)^2$, and other fluid properties are summarized in Table 3. There is no gravity or compressibility. The initial water saturation is set to the irreducible saturation, and then water and polymer are injected over the west boundary. The simulations are run using a fully-implicit solver with very strict convergence tolerance.

The saturations and concentrations are plotted in Figure 9 for the different IPV models at the end of the simulation. The percolation model was not able to converge to a solution in this example. The conventional and the uniform model have similar solutions, both with polymer concentration $c > c_{\max}$ at the front. For the state plotted in Figure 9, the maximum concentration is about $c = 5.9c_{\max}$ for the both the conventional model and for the uniform model, and thus show a similar sharp pile-up at the front as in the 1D examples. The non-uniform IPV model do not have values above the maximum.

In our usual implementation, the polymer concentration is limited between zero and the maximum concentration $c_{\max}$. That is, within each nonlinear iteration, the concentration values are forces to obey $c \leq c_{\max}$. If we try to run the same simulation using such a concentration limit, then the solver is not able to converge at all for the conventional and the uniform model.

s_{wir}	s_{ipv}	k_{rw}	k_{ro}	μ_w	μ_o
0.1	0.4	s^2	$(1-s)^2$	1 cP	10 cP

Table 3: Parameters for example 3. Scaled saturation s is given by (38).

7 Conclusion

The conventional method for modeling inaccessible pore space in reservoir simulation creates equations that are ill-posed. This was already shown in [1], and we demonstrated the ill-posedness here analytically by a simple one-dimensional example. This shortcoming of the conventional formulation motivated us to look for an alternative IPV model. The essential feature of an alternative model is to prevent any polymer to go faster than the water shock-front.

By considering shock-solutions of the one-dimensional equations, we first presented a necessary condition for well-posedness which put restrictions on the velocity enhancement factor of the IPV model. It is shown in the appendix that this necessary condition also is a sufficient condition for shock-solutions, given certain mild assumptions on the fractional flow function.

Based on a heuristic interpretation of the relative permeability, we then derived different possible models for IPV. An alternative model based on percolation theory was presented in [1], but this model has the restriction that the inaccessible pore volume has to be smaller than the irreducible water saturation. Herein, assuming a uniform polymer diffusion, we arrived at a model which allows for an inaccessible pore volume larger than the irreducible water saturation, and which reduces to the percolation based model if this is not the case. But, this model did still not fulfill the well-posedness condition for all relative permeability curves.

Another model was then developed by assuming a non-uniform polymer diffusion and by slightly relaxing the assumption of inaccessible pore volume. This model allows for a small fraction of the polymer to also enter the smallest pores, which then is not strictly inaccessible, but intrusion is restricted. This non-uniform model was seen to fulfill the well-posedness condition for any choice of relative permeability curves. Also this model reduces to the percolation based model in the case where the inaccessible pore volume is smaller than the irreducible water saturation.

Through numerical simulation of one- and two-dimensional models, the suggested non-uniform model was seen in practice to give well-behaving results. In all examples we have considered, the polymer concentration stayed below the maximum concentration, though we do not have a guarantee that this will always be the case. All the three other models considered showed spikes in the

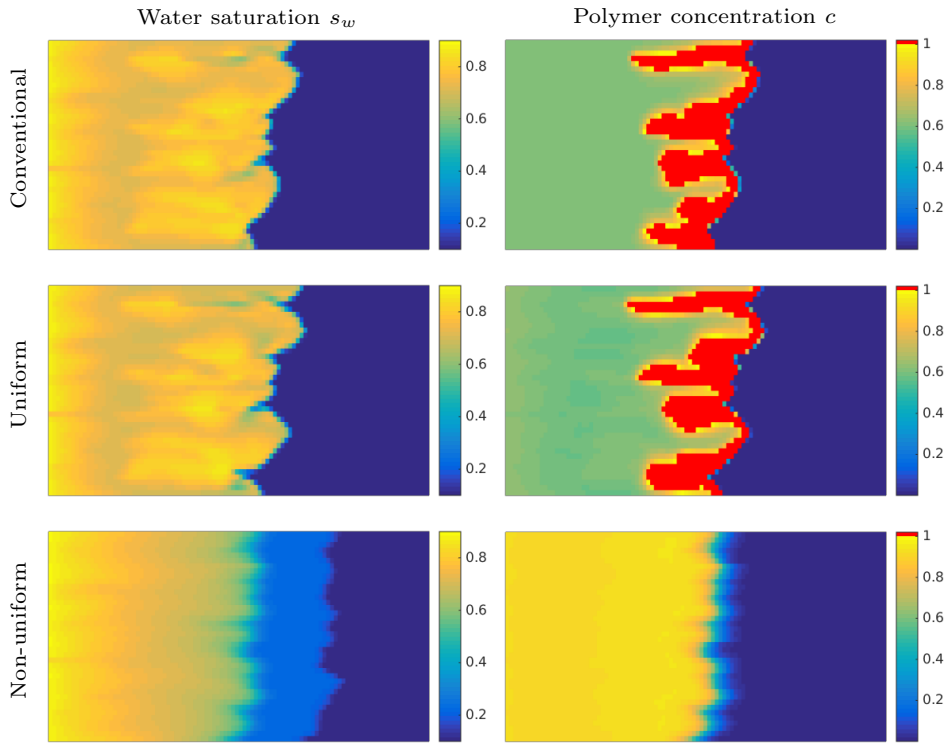

Figure 9: Solution of 2d model. Concentration values $c > c_{\max}$ are colored in red.

polymer concentration at the water front in one or more of the examples. Though polymer pile-up near the water front is not necessarily unphysical, the sharp spikes seem to grow uncontrolled in some cases, and could indicate problems in the equation formulation. In the two-dimensional example, it was also observed that when trying to enforce a maximum concentration on the nonlinear solver, the solver was only able to converge using the non-uniform IPV model.

The IPV models we present are simple to implement into an existing reservoir simulator, and gives thus a useful and practical alternative to the conventional model. A large mobility ratio increases the non-linearity of the equations, in addition to the non-linearities introduced by the polymer model itself. Therefore, polymer simulations often suffers from convergence problems. We believe our modification of the IPV model will be a step to improve convergence. As the polymer concentration in practice seem to be limited between zero and the maximum concentration, a priori known bounds can be used in a polymer solver to limit the solution space. Also, with the proposed model modifications, the highly efficient and unconditionally stable numerical scheme presented in [9] can be extended to also account for the effect of inaccessible pore space.

Acknowledgements

The research is partly funded by VISTA, which is a basic research program funded by Statoil and conducted in close collaboration with The Norwegian Academy of Science and Letters, and partly by the Norwegian Research Council through the PETROMAKS2 program, project number 244361.

8 Appendix

We have shown that the condition (12) is a necessary condition for well-posedness. With certain assumptions on the fractional flow function, we now show that this condition also is a sufficient condition when considering shock solutions where $s_l > s_r$. In the following proposition, s_{wir} denotes is the irreducible water saturation and s_{or} the residual oil saturation.

Proposition 8.1. *Assume that the fractional flow function $f \in C^1(s_{wir}, 1 - s_{or})$, has only one inflection point $\hat{s} \in (s_{wir}, 1 - s_{or})$, is strictly convex on $[s_{wir}, \hat{s}]$ and strictly concave on $[\hat{s}, 1 - s_{or}]$, see Figure 10. Assume further that (s_l, s_r) form a single shock where $s_l > s_r$. If the velocity enhancement factor satisfies*

$$\gamma(s) \leq \frac{s}{s - s_{wir}}, \tag{39}$$

for all $s \in [s_{wir}, s_l]$, then all pairs (z_l, z_r) are solvable and the model equations (8) are well-posed.

Proof. Consider a single shock pair (s_l, s_r) where $s_l > s_r$. We want to show that the apparent flux g_l, as defined by (10), is non-positive. Then the the well-posedness follows from the discussion in Section 4. Assuming (39) holds, we have

$$g_l = \frac{\gamma(s_l) f(s_l)}{s_l} - \frac{f(s_l) - f(s_r)}{s_l - s_r} \leq \frac{f(s_l) - f(s_{\text{wir}})}{s_l - s_{\text{wir}}} - \frac{f(s_l) - f(s_r)}{s_l - s_r}.$$

If $s_r = s_{\text{wir}}$, this immediately implies $g_l = 0$. Assume in the following that $s_r > s_{\text{wir}}$. We will prove that $g_l < 0$ in this case by a geometric argumentation. Define first the three line segments shown in blue in Figure 10: ℓ_{ml} go from s_{wir} to s_l, ℓ_{mr} go from s_{wir} to s_r, and ℓ_{rl} go from s_r to s_l. It is assumed that the solution of the Riemann problem is a shock, which implies that ℓ_{rl} must lie

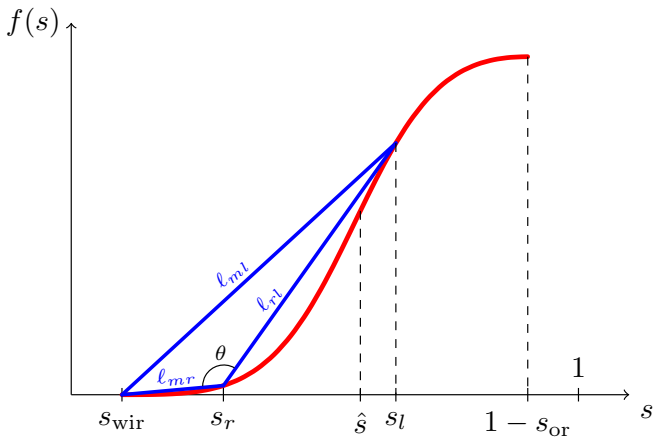

Figure 10: Plot of the fractional flow function with the definition of $\hat{s}$ and θ.

above $f(s)$ for all $s \in (s_r, s_l)$, that is,

$$\rho f(s_l) + (1 - \rho) f(s_r) > f(\rho s_l + (1 - \rho) s_r) \tag{40}$$

for $\rho \in (0, 1)$. Letting ρ tend to zero, this gives

$$f'(s_r) < \frac{f(s_l) - f(s_r)}{s_l - s_r}. \tag{41}$$

If $s_r \geq \hat{s}$, then $f(s)$ would lie above ℓ_{rl} for all $s \in (s_r, s_l)$ as f is strictly concave on $[\hat{s}, 1 - s_{\text{or}}]$, which would contradict the shock assumption. Thus, $s_r < \hat{s}$, and $f(s)$ is strictly convex on (s_{wir}, s_r). We

then have

$$\begin{aligned} f(s_l) - f(s_{\text{wir}}) &= f(s_l) - f(s_r) + f(s_r) - f(s_{\text{wir}}) \\ &< f(s_l) - f(s_r) + f'(s_r)(s_r - s_{\text{wir}}) \end{aligned}$$

by the strict convexity of f in (s_{wir}, s_r). Using (41), we get

$$\begin{aligned} f(s_l) - f(s_{\text{wir}}) &< f(s_l) - f(s_r) + \frac{f(s_l) - f(s_r)}{s_l - s_r}(s_r - s_{\text{wir}}) \\ &= \big(f(s_l) - f(s_r)\big)\frac{s_l - s_{\text{wir}}}{s_l - s_r} \end{aligned}$$

and it follows that $g_l < 0$ for all shock pairs when $s_r > s_{\text{wir}}$. This concludes the proof. □

We note, without proof, that for a given fractional flow function f, which fulfills the assumptions in Proposition 8.1, there exists a point $s^* > \hat{s}$, which is such that for any $s_l \in (s_{\text{wir}}, s^*]$, there exists an $s_r < s_l$ such that (s_l, s_r) is a single shock and, reciprocally, if (s_l, s_r) is a single shock, then $s_l \leq s^*$. This point is s^* is defined by

$$f'(s^*) = \frac{f(s^*) - f(s_{\text{wir}})}{s^* - s_{\text{wir}}},$$

if this point exists, or otherwise by the end point $s^* = 1 - s_{\text{or}}$. This means that if (39) is fulfilled for all $s \in [s_{\text{wir}}, s^*]$, then the problem is well-posed.

We also note that in the case where $s_l < s_r$, and otherwise with the same assumptions as in Proposition 8.1, the condition (39) simply has to be replaced by $\gamma(s) \leq \frac{s}{s - s_{\text{or}}}$.

References

[1] G. A. Bartelds, J. Bruining, and J. Molenaar. The modeling of velocity enhancement in polymer flooding. *Transport in Porous Media*, 26(1):75–88, 1997.

[2] R. Brooks and A. Corey. Hydraulic properties of porous media, hydrology papers, no. 3, colorado state university, ft. *Collins, Colo*, 1964.

[3] N. T. Burdine et al. Relative permeability calculations from pore size distribution data. *Journal of Petroleum Technology*, 5(03):71–78, 1953.

[4] Center for Petroleum and Geosystems Engineering of The University of Texas at Austin. *Technical Documentation for UTCHEM-9.0 A Three-Dimensional Chemical Flood Simulator*, 2000.

[5] Computer Modelling Group Ltd. *User's guide STARS*, 2009 edition, 2009.

[6] V. Danilov and D. Mitrovic. Delta shock wave formation in the case of triangular hyperbolic system of conservation laws. *Journal of Differential Equations*, 245(12):3704–3734, 2008.

[7] R. Dawson, R. B. Lantz, and M. Aime. Inaccessible pore volume in polymer flooding. *SPE J.*, 253(3522):448–452, 1972.

[8] L. W. Lake. *Enhanced Oil Recovery*. Society of Petroleum Engineers, reprint 2010 edition, 1989.

[9] K.-A. Lie, H. M. Nilsen, A. F. Rasmussen, X. Raynaud, et al. Fast simulation of polymer injection in heavy-oil reservoirs on the basis of topological sorting and sequential splitting. *SPE Journal*, 19(06):991–1, 2014.

[10] U. L. Norris. Core-scale simulation of polymer flow through porous media. Master thesis, University of Stavanger, Norway, 2011.

[11] M. Pancharoen, M. R. Thiele, A. R. Kovscek, et al. Inaccessible pore volume of associative polymer floods. In *SPE Improved Oil Recovery Symposium*. Society of Petroleum Engineers, 2010.

[12] Schlumberger. *Eclipse Technical Description Manual*, 2009.2 edition, 2009.